THE SUPERSONIC JET SPECTROSCOPY OF [2.2]PARACYCLOPHANE

By

Tun-Li Shen

A DISSERTATION

Submitted to

Michigan State University

in partial fulfillment of the requirements

for the degree of

DOCTOR OF PHILOSOPHY

Department of Chemistry

1992

ABSTRACT

THE SUPERSONIC JET SPECTROSCOPY OF [2.2]PARACYCLOPHANE

By

Tun-Li Shen

Supersonic jet expansion is an extremely useful technique for molecular spectroscopic studies of large molecules. The main advantange offered by this technique is the significant cooling of the molecular rotation and vibration temperatures. In this dissertation, the principles and construction of a supersonic jet apparatus is discussed; further, the analysis of an electronic transition of a large molecule, [2.2]paracyclophane, by laser-induced fluorescence spectroscopy is reported.

The fluorescence excitation spectrum of [2.2]paracyclophane has been recorded from 30675 cm^{-1} to 32570 cm^{-1}. Two inter-ring vibrations, the breathing mode and the twisting mode, are responsible for the extensive vibronic structure observed in this lowest-lying electronic transition. The breathing mode gives rise to a long dominant progression with origin at 30772 cm^{-1} and fairly even separations of 235 cm^{-1}. The remaining progressions are built on this breathing mode with several binary combinations of the twist.

To my parents

ACKNOWLEDGMENTS

I wish to thank my adviser Professor Leroi for allowing me to join his research group and for all the encouragement, inspiration and guidance he has given me during my graduate work. As his student, I benefitted from working in open atmosphere that he fostered. I will always be grateful that he motivated me by sharing his own enthusiasm. I especially thank him for the help and support he has provided when things were not working well.

I thank my second reader Professor Nocera for offering suggestions and advice. I also thank Professor Jackson for carrying out the calculations described in this dissertation.

Many people have helped me over the years. I would like thank Deak Watters, Sam Jackson and Russ Geyer of the Chemistry Department Machine Shop as well as Scott Sanderson of the Electronics Shop for their friendship and efforts. I thank Marty Rabb for being always willing to listen and provide suggestions; I also thank him for helping me assemble the pulsed valve driver. I acknowledge my colleague Jia-Hwa Yeh for his participation in the paracyclophane experiment.

I am deeply grateful to my wife Dai-Hua for her patience, understanding and encourgement.

TABLE OF CONTENTS

LIST OF TABLES

LIST OF FIGURES

CHAPTER I

INTRODUCTION

The first molecular beam experiment was carried out by the frenchman Dunoyer in 1911 [1,2]. In this 20 cm glass apparatus (shown in Figure 1-1), sodium was placed in chamber A and heated to vaporize and then deposit on the closed end of chamber C. Based on the pattern of the deposit, this experiment confirmed that the Na beam travelled in a straight line under vacuum. In fact, the object of the earliest molecular beam experiments was to measure molecular velocities. In 1920, Stern designed another apparatus to measure the molecular velocity distribution of silver atom beams, and the results were found to be in agreement with the theoretical prediction [1,2].

Two experimental methods were dominant in the early years of molecular beam research [3]: the deflection method, and the resonance method. With the deflection method, atomic or molecular beams passed through an inhomogeneous magnetic field H. If the sample posses a magnetic dipole μ, the magnetic field will exert a force $\nabla(\mu \cdot H)$, and this force would split the beam into several components dependent on the magnetic quantum number. The most important achievement of this method

Figure 1-1 The first molecular beam apparatus

is the Stern and Gerlach experiment. In that experiment, a silver atom beam passed through an inhomogeneous magnetic field produced by an iron magnet and split into two components. According to quantum mechanics, the magnetic dipole of the atom is $\mu=mg\mu_0$ (m: magnetic quantum number, g: Lande g factor, and μ_0: Bohr magneton); m can have 2J+1 values, where J is the total angular momentum of the atom. Since the ground state of the silver atom is $^2S_{1/2}$, the splitting into two components indicated that J=1/2. This was the first verification of a half-integral angular-momentum quantum number. For molecules like those with $^1\Sigma$ symmetry which have no electronic magnetic moment, any deflection in an inhomogeneous field is due to the nuclear magnetic moment and/or the rotational magnetic moment. Magnetic moments of the proton and the deuteron, as well as the rotational magnetic moments of H_2, D_2, and HD, were determined by this method.

The resonance method was introduced by Rabi in 1938 [3]. The basic idea of this method is that the transitions between nuclear spin states could be induced in a homogeneous magnetic field by adding a radio-frequency field. The frequency of the radio-frequency field will satisfy the Bohr condition for the two spin states being connected. Three magnetic fields were used in this method (A-B-C fields); the A and B-fields acted as the polarizer and analyzer, while the C-field produced the Zeeman effect and provided the magnetic scanning of the

resonance spectrum. In the deflection method one can measure only dE/dH for the magnetic states. On the other hand, the energy differences between different magnetic states are measured in the resonance method. Most molecular beam work in the 1940-50s employed the resonance method. An important variant of the resonance method is the inhomogeneous electric field method first introduced by Hughes for the study of rotational transitions of molecules such as cesium iodide [4,5].

The application of molecular beams in chemistry can be broadly divided into three categories [6]: (1) Measurement of static and dynamic properties of isolated molecular systems; (2) Molecule-molecule collisions; (3) Molecule-surface interactions. The first category includes a large amount of work starting from the early days of molecular beam research; this is the area in which most spectroscopic work in the past two decades belongs. The research on chemical reactions by using molecular beams began with the work of Bull and Moon on the reaction of Cs + CCl_4 and of Taylor and Datz on the reaction of K + HBr in 1955. The development and contributions of this area have been well documented in the Discussions of the Faraday Society meetings [7] and in standard texts describing molecular reaction dynamics [8]. The third category represents a broad area related to the understanding of surface phenomena. The application of molecular beams to the study of interactions of molecules with

surfaces started with Stern's work in the early years [2,3]; this area has expanded rapidly in recent years.

Molecular beam techniques were rarely used by molecular spectroscopists in the 1960s, although a handful of examples can be found. By using a Rabi-type molecular beam electric resonance spectrometer as the basic experimental tool, Klemperer and coworkers [9] have studied the electric dipole moments of small molecules in the electronic ground state, the electric dipole moments of molecules in electronic excited states, the geometry of molecules containing cesium, and loosely bound molecular complexes [10]. The principle of this method is that an inhomogenous electric field is employed to deflect the molecular beam by the Stark effect; since the Stark effect depends on the rotational state of the molecule, different rotational transitions will have different trajectories.

While the theoretical and experimental investigations of supersonic jets were fairly complete before the 1970s, the application of supersonic jets to optical spectroscopy was pioneered by the reseach group of Levy around 1974 [11-14]. The maturation of laser technology provided the impetus for the development of laser supersonic jet spectroscopy. In a series experiments, the Levy group has shown the advantages of optical spectroscopy with supersonic jets. The first example was NO_2. The spectrum of NO_2 extends from 4000 Å in the near uv to 8000 Å in the near ir; since it has a very high

density of lines, the spectroscopic analysis was extremely difficult. When NO_2 was seeded in argon (as the carrier gas), the lowering of the internal temperature led to a significant simplification of the spectrum. In the thousand Angstrom region from 6700 Å to 5700 Å, 140 vibronic bands have been identified and analyzed. In the NO_2 studies, the supersonic expansion was used to simplify a spectrum that is difficult to analyze in static gas experiments. For large molecules like the phthalocyanines, the spectral features are several hundred wavenumbers wide in the static-gas experiment. In the supersonic jet-cooled spectrum of this large molecule, the vibrational features were resolved and sharp lines with widths of less than 1 cm^{-1} were observed. This proved that the supersonic expansion can be very useful in the study of large molecules. Another important application of supersonic jet spectroscopy demonstrated by Levy's group is the study of van der Waals molecules [14]. Two types of problems can be studied: (1) Structural studies - by analysis of rotational and vibrational structure in the fluorescence excitation spectrum, small to medium size molecules like I_2, benzene, and tetrazine bound to helium, argon or the hydrogen molecule have been studied; (2) Photochemistry - in these experiments, van der Waals molecules can be used as model systems to study the intramolecular energy redistribution. From the study of the He-I_2 molecule, the rates for transfer of energy from the I_2 vibration to the He-I_2 bond (which results in predissociation

of the van der Waals molecule) have been measured; these transfer rates as a function of vibrational states can be fit to the Golden Rule type model, which essentially predicts that the energy gap between the I_2 vibrational quantum and the van der Waals bond mode will determine the energy transfer, and the larger the gap the less likely these two modes will couple. The significance of these experiments is that they have exemplified not only the advantages of applying the supersonic jet technique in spectroscopic experiments, but they also opened up new areas of research.

Many observations of van der Waals molecules by various experimental techniques such as infrared, Raman, ultraviolet, mass spectrometry as well as electron diffraction have been employed [15-18]. Except for the mass spectrometry and electron diffraction experiments, most of the optical spectroscopic experiments were of molecules in an equilibrium cell. The production of van der Waals molecules in a cell depends on reduced temperature, increased sample pressure, and increased path length. The ease of using supersonic jets to generate van der Waals molecules has provoked interest in their study in almost every area of molecular spectroscopy. The first systematic study of van der Waals molecules in the supersonic jet was by W. Klemperer [19], who employed the molecular beam electric resonance method, actually a spectroscopic analysis in the microwave region. Many diatomic and polyatomic noble gas complexes have been investigated.

The specific information obtained about these complexes includes molecular geometry, and parameters of potential energy functions such as dissociation energy, equilibrium internuclear distance and force constants.

The development of supersonic jet spectroscopy in the 1970s has established the foundation for a number of important areas of research.

The most impressive progress has been in the following areas:

(1) The study of molecular complexes
- the geometry of van der Waals molecules [20-24]
- the dynamics of van der Waals molecules [25-28]
- the study of condensed phase reactions and in the gas phase [29-33]

(2) The study of large molecule spectroscopy
- Intramolecular vibrational energy redistribution (IVR) [35-39]
- Intramolecular large amplitude motions [40,41]

The central theme of this dissertation is the application of the supersonic jet technique to study the molecular spectroscopy of large molecules. The two areas where supersonic jets have made an impact are described in category (2). The cooling which results from supersonic expansion reduces spectral congestion, and thus facilitates the spectroscopic assignment for large molecules. For larger molecules, the density of vibrational states can be very high,

and the study of intrinsic properties of the molecules (especially when vibrational analysis is important) is possible only in the cold and isolated environment provided by a supersonic jet. An interesting aspect of large molecules is that they are likely to have large amplitude, low frequency vibrational motions, e.g. the inter-ring modes of [2.2]paracyclophane; the supersonic jet technique is best suited for the study of these vibrational mode(s).

At room temperature, a large number of quantum states of a large molecule will be populated. Each populated state may contribute to the overall spectrum, and therefore the entire spectrum is a composite of many lines. Under normal laboratory conditions, the electronic spectrum of a large molecule consists of broad and unresolved features. Detailed spectroscopic analysis is prohibited by this complexity. This situation arises from the fact that large molecules have a large number of vibrational degrees of freedom and that the excited vibrational levels are populated, which gives rise to many hot bands in the spectrum. Although many low temperature spectroscopic methods have been used to reduce the internal temperatures of large molecules, these methods generally create a perturbed environment for the molecule under study.

The development of the supersonic jet technique helped solve this problem. The thermal energy of a molecule is converted to directed translational energy during the expansion process.

The temperatures of the translational, rotational, and vibrational degrees of freedom are greatly reduced. In many cases, the translational and rotational temperatures can be as low as 10 K or lower. The vibrational temperature is somewhat higher due to the ineffective vibrational<->translational energy transfer process [1-34], ($\tau_{V->T}$~10^{-5}, $\tau_{R->T}$~10^{-8}, $\tau_{T->T}$~10^{-9} sec); however, a vibrational temperature of 50 K or lower is obtainable for large molecules. In the resulting cold spectrum, individual vibrational features of large molecules can be resolved, and thus detailed spectroscopic analyses are possible. Now let us discuss the study of large amplitude motion in large molecules.

The large amplitude motions of flexible molecules have captured the attention of molecular spectroscopists for many years [40,41]. Many experimental techniques have been used to study large amplitude vibrational motions, such as internal rotation, including the spectroscopic method, diffraction method, relaxation method and classic method [41]. Some of the interesting topics involving molecular internal motion are: the number of different rotational isomers, the preferred conformation of stable rotameric forms, the shapes of potential energy functions for large amplitude motions and the heights of barriers impeding motions such as inversion, ring puckering internal rotation and torsion.

Among the experimental methods, microwave [42], and infrared and Raman [43] spectroscopy are perhaps the most popular

spectroscopic methods, and they have provided the most extensive experimental data on large amplitude motions in the past. The main characteristics of a microwave spectrum are determined by the molecular geometry and nuclear masses, hence internal motions can be studied by microwave spectroscopy in several ways. One way is through the phenomenon called quantum mechanical tunneling. Tunneling can occur when there are two or more equivalent molecular configurations which are interconvertible by the internal motion. Tunneling gives rise to a splitting of some of the spectral lines. Since these splittings are sensitive to the potential function involved, they provide a very accurate way of determining the potential function associated with the internal motion. Another way in which internal motions can affect the microwave spectrum is by shifting the spectral lines. This occurs through a modification of the moments of inertia. In microwave spectroscopy, the basic data obtained from the analysis of measured rotational transition frequencies of a molecule are the molecular rotational constants. In general, different rotational isomers have different moments of inertia and therefore different rotational spectra. Analysis of these spectra can provide information on the potential energy functions that govern large amplitude vibration. Infrared and Raman spectroscopy involve measurement of frequencies of the vibrational transitions of a molecule. The vibrational frequencies themselves are characteristic of the spatial

arrangements of the nuclei, the atomic masses and the forces acting between the nuclei. The fundamental absorption of many large-amplitude vibrations occurs in the far-infrared region, i.e. < 200 cm^{-1}, and the measurement of absorption bands associated with these vibrations gives information about the barriers to internal motions. However, large amplitude vibrations often give rise to weak absorptions; thus, correct assignments of these bands needed to determine the barrier height are not always straightforward. Sometimes "hot" bands of a large amplitude vibration, e.g. a torsional vibration, can be observed involving vibrational transitions between excited states such as v = 2 <-- 1, and 3 <-- 2 transitions. This information about higher vibrational states can be very helpful in constructing the relevant potential function. Futhermore, in the case of torsional vibrations, an alternative way to study these states is to observe them in combination with other absorptions in the near-infrared [43].

It has been recognized that electronic spectroscopy of molecules cooled in supersonic jets can be appllied to the study of large amplitude vibrations, both in the ground and excited electronic states [44]. The information obtained in the ground electronic state is comparable to that obtained from the rotational and vibrational methods; however, the information in electronic excited states can be obtained only by electronic spectroscopy. A typical example is the study of the internal rotation of the CH_3 group in large molecules.

For fluorotoluene [45], the fluorescence excitation and dispersed fluorescence spectra have been studied in a supersonic jet. The analysis of the vibronic bands associated with the internal rotation of the CH_3 group yields accurate potential functions for this motion for both the ground and first excited states. It was shown that the barrier to internal rotation changes dramatically going from ground to excited states.

The torsional motion of trans-stilbene is another example of a large amplitude motion in the ground state that could not be observed by vibrational spectroscopy, but has been successfully characterized by jet spectroscopy [44,46]. Other large amplitude motions studied by jet spectroscopy include the torsion around the C-C bond in the molecules 9-phenylanthracene [47], biphenyl [48], bianthracene [49], xylene [50], dimethyl-aminobenzonitrile [51], methylbenzyl radical [52], and methylnaphthalene [53]. The major portion of this dissertation will focus on the investigation of the electronic spectroscopy of the large aromatic molecule [2.2]paracyclophane, which is comprised of cofacial benzene rings bound by dimethylene bridges. Unlike the molecules mentioned above, the low-frequency internal modes of [2.2]paracyclophane involve the motion of the two benzene rings and the two methylene bridges (two-carbon alkyl chains). In fact, an interesting aspect of this molecule is the large amplitude motion involving the twisting and the breathing of

the two benzene rings around the long molecule axis. The study of the fluorescence excitation indicates that the twisting vibration has a measurable barrier in the ground electronic state and a much lower barrier in the excited state.

Chapter II

Experimental Methods

In this chapter, the principles of supersonic jets will be introduced, and practical considerations of designing nozzles, vacuum systems, and dectection methods will be discussed. The experimental results on characterization of a pulsed beam by a fast ionization gauge (FIG) dectector, as well as fluorescence excitation experiments on perylene and aniline, will also be presented.

2-1. Effusive beam vs. supersonic nozzle beam

The evolution of nozzle designs played a key role in the development of molecular beam techniques. Essentially all the beam experiments before 1950 used the effusive beam source [3]. In 1951 Kantrowitz and Grey [54] first suggested that the coventional effusive beam source can be replaced by a supersonic jet provided that the pumping capacity can handle all the gas load admitted into the vacuum system.

In the effusive beam source, the molecular vapor flows from an oven into a vacuum chamber, and the molecules move through

the orifice (or slit) without undergoing any collisions. Under these conditions, the "Knudsen number" K_n is greater than 1.

$$K_n = \frac{\text{mean free path in the source}}{\text{dimension of the orifice}}$$

The beam properties such as the spatial distribution of the beam flux and the velocity distribution can be accurately predicted by the simple kinetic theory of gases. In the case of $K_n > 1$, few collisions occur in the effusive beam source, and all the internal states of the molecules are at the thermal equilibrium; i.e. the internal temperature of the molecules is characterized by the source temperature.

In the supersonic nozzle beam, the source pressure is of the order of 10^2 torr or higher; $K_n < 1$. The molecular flow is hydrodynamic through the nozzle (see Figure 2-1 for the main features of supersonic jet expansion). The theory for supersonic expansion has been treated in many previous reviews [55-57], thus only the most important results are discussed here.

The basic relationship in the supersonic expansion is the energy equation (first law of thermodynamics),

$$h + mv^2/2 = h_0 \qquad \text{(II-1)}$$

h_0: enthalpy per unit mass prior expansion

h: enthalpy per unit mass after expansion

v: velocity of the molecules of mass m

Figure 2-1 The structure of free jet expansion

FREE-JET EXPANSION

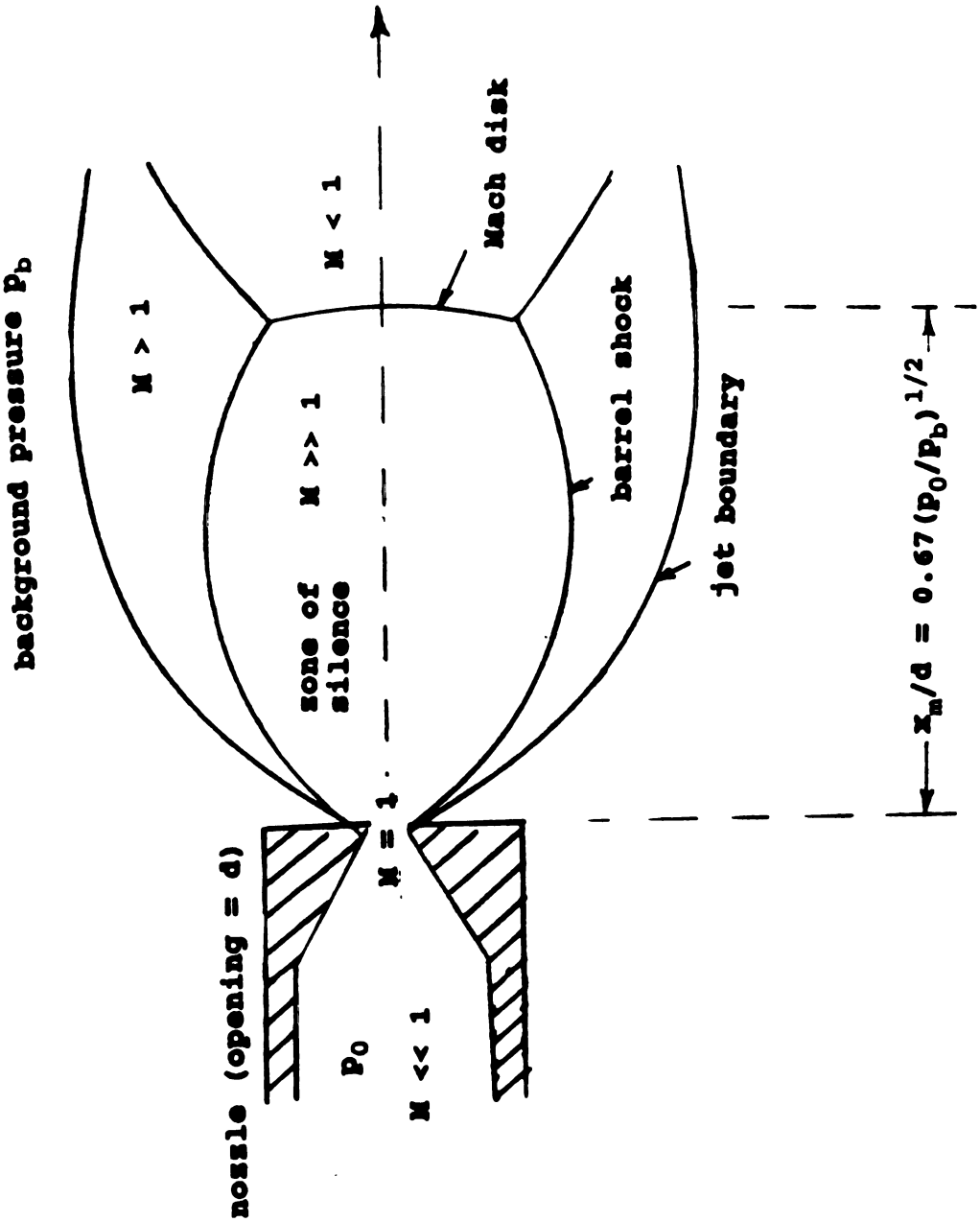

If we assume the expansion is isentropic, ideal gas behavior, and constant C_p or γ, we can write

$$dh = C_p\, dt$$

and from the first law,

$$mv^2/2 = h_0 - h = \int_T^{T0} C_p\, dT$$

$$= C_pT_0 - C_p\, T \qquad \text{(II-2)}$$

This equation can be rearranged into to a more convenient form by introducing two parameters: γ $(=C_p/C_v)$, a property of the molecules in the expansion, and M the Mach number (M=v/a, where a is the local speed of sound; $a = (\gamma RT/M)^{1/2}$). If we divide equation (II-2) by a^2,

$$C_pT_0 \,/\, (\gamma RT/m) \;-\; C_pT \,/\, (\gamma RT/m) = 1/2\; mv^2/\, a^2$$

For an ideal gas, $C_p/R = \gamma/\gamma-1$, thus

$$T/T_0 = [\; 1 + M^2(\gamma-1)/2 \;]^{-1} \qquad \text{(II-3a)}$$

and

$$p/p_0 = (T/T_0)^{\gamma/(\gamma-1)} = [\; 1 + M^2(\gamma-1)/2 \;]^{-\gamma/(\gamma-1)} \qquad \text{(II-3b)}$$

$$n/n_0 = (T/T_0)^{1/(\gamma-1)} = [\; 1 + M^2(\gamma-1)/2 \;]^{-1/(\gamma-1)} \qquad \text{(II-3c)}$$

We can see immediately that for M = 10 and with γ =5/3 (for a monoatomic gas), T/T_0 may be close to 3×10^{-2}, a large amount of temperature drop!

In the free jet, the reservoir pressure and the nozzle size are kept at a ratio such that $K_n < 1$; thus, there will be many

collisions when gas flows through the the nozzle and downstream from the nozzle. This hydrodynamic processes converts the random thermal motion of the molecules behind the nozzle into directed motion after expansion and results in an increase of mass flow velocity. Therefore, the enthalpy of the random motion is reduced in the expansion and supplied to the directed flow. The conversion of random motion into the directed mass flow causes the temperature to decrease and the Mach number to increase, since the classical speed of sound decreases with temperature. In the ideal expansion, M = 1 at the throat of the nozzle, and M > 1 beyond this point and it is thus called supersonic. The free jet can be characterized by the diameter of the jet boundary and the location of the Mach disk (see Figure 2-1). The actual location of the Mach disk is given by [59] $x_m/d = 0.67(p_0/p_b)^{1/2}$ where p_0 is the initial pressure and p_b is the background pressure. The width of the jet boundary is on the order of 0.75 x_m. These parameters define the region where experiments are carried out.

Ashkenhas and Sherman [58,59] have treated the expanding gas as a continuous medium and used the method of characteristics to obtain an expression for the Mach number as a function of the distance downstream from the nozzle

$$M = A\ (x/d)^{\gamma-1} \qquad \text{(II-4)}$$

where X is the distance from the nozzle, d is the nozzle diameter, and A is a constant which depends on γ and is equal to 3.26 for a monoatomic gas (let x/d = X; M = 3.26 $X^{2/3}$). It is clear that downstream from the nozzle (X usually much larger than 1) the Mach number increases and the temperature, pressure, and density decrease. From (II-3) and (II-4) we obtain

$$n/n_0 = \{[(\gamma - 1)/2]M^2\}^{-1/\gamma - 1}, \quad M >> 1 \qquad \text{(II-5)}$$

$$= (1/3M^2)^{-3/2}$$

thus,

$$n/n_0 \propto X^{-2}$$

Anderson and Fenn [57] have shown that the Mach number will reach a terminal value due to the decrease of density and hence the number of collisions downstream from the nozzle, and derived

$$M_T = 133(p_0 d)^{0.4} \qquad \text{(for Ar)}$$

Since the probability for a molecule making a binary collision is proportional to the pressure, $p_0 d$ is proportional to the total number of binary collisions. The formation of a bound dimer requires at least a three-body collision, and the number of these collisions is proportional to $p_0 d^2$. With the nozzle diameter fixed, the formation of such complexes will increase

with pressure.

The generation of molecular beams by using the supersonic jet technique has enhanced the experimental capability of molecular spectroscopy. The supersonic method of best choice for most spectroscopic experiments is the so called "seeded" beam technique [60-62].

The initial motivation to develop this technique was to obtain a molecular beam with higher energy. For example, a source temperature of 3000^0 K will correspond to a kinetic energy of the effective beam of about 12 kcal/mole or 0.5 eV/molecule. By using the seeded beam technique, molecules with kinetic energy above 1 eV can be obtained.

In the seeded beam method, the sample molecule under study is mixed with a large excess of light diluent gas, and accelerated to a velocity essentially equal to that of the diluent gas because of collisions during expansion. Hence, for very dilute solutions of a heavy molecule in a light carrier gas, the energy of the heavy species approaches the value of the product of the molecular mass ratio (heavy to light) and the kinetic energy of the heavy component expanded alone. The behavior of the gas mixture in the jet is the same as that for a pure gas with molecular weight and heat capacity equal the average for the mixture.

When a polyatomic molecule is seeded into a monoatomic carrier gas, it is accelerated aerodynamically to the velocity of the carrier gas, producing a translational temperature

nearly as low as that of the monoatomic gas. Following the supersonic expansion, the rotational temperature of a polyatomic molecule seeded into a monoatomic gas is almost the same as its translational temperature. The vibrational temperature will not be quite so low due to the fact that vibrational relaxation is much slower.

It should be recognized that a typical behavior of seeded beams is the velocity slip effect: the velocity of the heavy molecule slips behind the diluent gas velocity. In general, the speed ratio of heavy molecule to carrier gas molecule becomes less than 1 when the mass difference between the seed and diluent species is large. As a consequence, the efficiency of rotational cooling of I_2 varies markedly in the order He<<Ar when both diluents are at the same pressure. Thus, for large molecules, effective internal cooling (vibrational and rotational) at a moderate pd value can be accomplished in the heavier carrier gases such as Ar, Kr and Xe, but not He.

II-2. The design of a supersonic jet

A free jet source-nozzle can be constructed from almost any machinable material with different nozzle geometries [63], according to the need of a particular experiment and temperature range over which the nozzle will be operated. Small sources (d < 500 μm) commonly use electron microscope aperture pinholes, which are mechanically sealed or electron-

beam welded onto the end of a metal tube. Our cw nozzles were made in this manner [70]. Alternatively, glass (or quartz) tubing can be drawn down, or the end closed by heating and then reopened by grinding to make a short converging source of fairly small diameter. In Figure 2-2 the most commonly used nozzles of various geometry are shown. Although it is not yet clear how the internal temperature in the supersonic expansion depends on the nozzle geometry, the conical nozzle has proven to be the most effective one in producing clusters. Capillaries or capillary bundles (mutichannel nozzle) can also be used [64,65]; theoretical analysis and applications of these nozzles have been discussed in the literature [65]. Recently, the popularity of two-dimensional slit nozzles is growing for many experiments using supersonic jets [66,67], and it may become the exclusive choice for absorption spectroscopy. The planar supersonic expansion from a slit nozzle has the advantage that the intensity of the jet will decrease as a function of distance from the nozzle according to x^{-1} instead of x^{-2} (equation II-5) for the circular nozzle. The consequences are that the higher number density and slower cooling will increase total two- and three- body collisions, and thus enhance the formation of clusters. Moreover, the collimation of velocities in the plane of the slit reduces the Doppler broadening for optical probes parallel to the slit, which reduces the linewidths for high resolution spectroscopy.

Figure 2-2 Cross sections of commonly used nozzle geometries. The conical nozzle has proven to be the most efficient in terms of generating pulsed or continuous beams of large clusters; slit nozzles have been used widely in absorption spectroscopic experiments since they provide the longest path length.

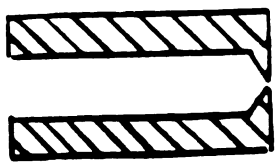

SONIC

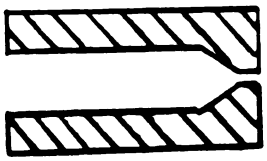

CYLINDRICAL

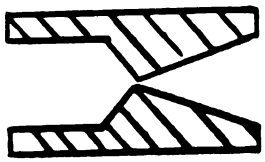

CONICAL

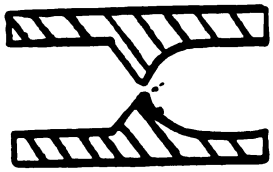

LAVAL

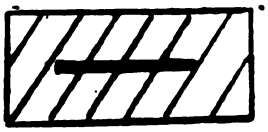

SLIT

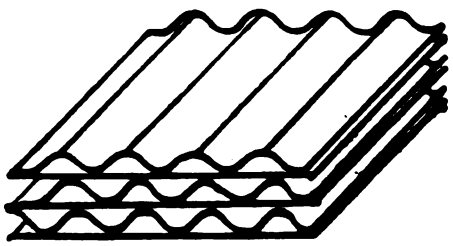

MULTICHANNEL

The controlling factor in the production of a free jet is the throughput, T (torr l/s) of the vacuum system, which is equal to the product of pumping speed (l/s) and chamber pressure (torr). Throughput can be related to the source conditions by [59]

$$\text{Throughput} = (\text{pumping speed})\ (\text{chamber pressure})$$

$$= C\ (T_c/T_0)\ [(300/T_0)]^{1/2}\ (p_0 d)\, d$$

Here T_c is the vacuum chamber temperature, usually room temperature. T_0 is the source temperature, $T_c/T_0 \approx 1$; $p_0 d$ is in torr cm (d in cm). C (l/cm^2 s) is a constant, C having a value like 45 (for He), or 14 (for Ar). The free jet properties and the beam intensity are related to $p_0 d$; in principle, free jets can be obtained for $p_0 d \geq 1$ torr cm, and clustering effects can take place when $p_0 d \geq 10$ torr cm.

Our pumping system consists a 6" diffusion pump which has a nominal pumping speed of 2400 l/s (without baffle). If we use Ar as our carrier gas, and a continuous nozzle with 200 μm diameter, the throughput corresponding to a source pressure of 760 torr at room temperature can be calculated as

$$\text{Throughput} = 14\ p_0\ d^2 \quad \text{torr l/s}$$

$$= 14\ (760)\ (0.0200)^2$$

$$= 4.256 \quad \text{torr l/s}$$

The pressure in the vacuum chamber can be calculated approximately

$$P_{\text{chamber 1}} = (4.256 \text{ torr ls}^{-1})/2400\text{ls}^{-1}$$
$$= 1.77 \times 10^{-3} \text{ torr}$$

For an isentropic expansion, the general formula for the number density is given by $n = 0.161 \times n_0 \times p_0 \times (x/d)^{-2} \times \cos^2\theta$ [65], where θ is the angular displacement from the centerline of the expansion. On the beam axis $\theta = 0$, so that

$$n = 0.161 \times n_0 \times p_0 \times (x/d)^{-2}$$

where n_0 is the number density of one torr at STP,

$$n_0 = 3.24 \times 10^{16} \text{ atom/cm}^{-3}, \text{ and}$$

x is the distance from the nozzle. For x = 0.5 cm

$$n = 0.161 \times 3.24 \times 10^{16} \times 760 \times (0.0200/0.5)^2$$
$$= 6.3 \times 10^{15} \text{ atom/cm}^{-3}$$

The calculation above is for the situation where only one chamber is used to produce the jet. However, many experiments will require a second chamber, the two chambers being separated by a skimmer (a differential pumping system.)

Continuing the calculation, we can estimate the pressure in the second chamber. If the skimmer (with a diameter of 0.06 cm) is located at 0.5 cm from the nozzle, the beam flux at the skimmer entrance is (assuming the velocity v of Ar is 5×10^4 cm/s)

$$n \times v = 5 \times 10^4 \times 6.3 \times 10^{15}$$
$$= 3.15 \times 10^{20} \text{ atom cm}^{-2} \text{ s}^{-1}$$

The number of atoms entering the second second chamber is

$$3.15 \times 10^{20} \times \pi/4 \times (0.06)^2 \text{ atoms s}^{-1}$$
$$= 8.9 \times 10^{17} \text{ atoms s}^{-1}$$

This corresponds to a throughput of

$$(8.9 \times 10^{17} \text{ atom s}^{-1})/(3.24 \times 10^{19} \text{ atom torr}^{-1} \text{ l}^{-1})$$
$$= 2.74 \times 10^{-2} \text{ torr l s}^{-1}$$

The pressure in the second chamber (also pumped by a 6" diffusion pump with 2400 ls^{-1} pumping speed) will be

$$(2.74 \times 10^{-2} \text{ torr l s}^{-1})/(2400 \text{ l s}^{-1})$$
$$= 1.14 \times 10^{-5} \text{ torr}$$

A schematic diagram of the chamber constructed in our

laboratory is shown in Figure 2-3. The vacuum system consists of a stainless steel chamber with four ports (two 6" ports, and two 9" ports). The supersonic source assembly is mounted on one of the 6" ports (top); opposite to this port is the 6" oil diffusion pump (Dresser DPD-6, 2400 l s^{-1}). The diffusion pump is backed by a two-stage mechanical pump (Sargent-Welch 1397, 17 CFM). The diffusion pump can be closed off from the chamber by an aluminum manual sliding gate valve.

The beam source is attached to an xyz-translator which controls the position of the nozzle (either the cw or the pulsed nozzle) from outside the vacuum; the translator is fixed onto a separate chamber which mounts onto the main vacuum system. This design allows us to detach the source assembly in case the sample needs to be refilled or to change the nozzle. The details of the continuous nozzle source have been described elsewhere [70]. The pulsed nozzle will be discussed in later sections of this chapter.

The intensity of scattered light is often the factor that limits the sensitivity for the collection of laser-induced fluorescence. Optimization of the signal-to-noise ratio requires the reduction of the unwanted scattered laser light [69]. This is especially important when the fluorescence itself is weak. The scattered light can be reduced in several ways: by using light baffles [71], by coating of all the surfaces inside the detection chamber black, or by using color cutoff filters or spatial filters. The most efficient way to

Figure 2-3 **Schematic diagram of the pulsed molecular beam apparatus constructed in our laboratory.**

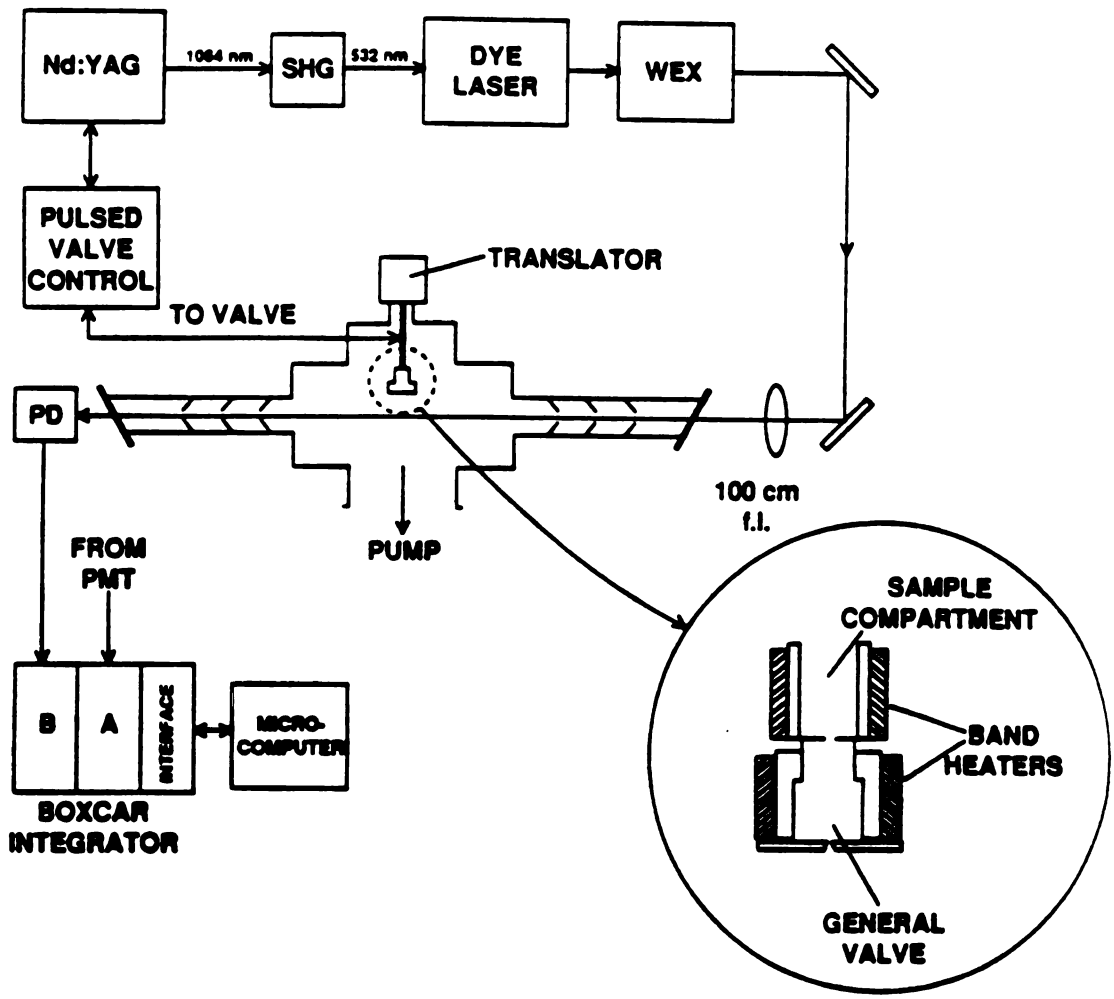
Nd:YAG
1064 nm
SHG
532 nm
DYE LASER
WEX
PULSED VALVE CONTROL
TRANSLATOR
TO VALVE
PD
100 cm f.l.
FROM PMT
PUMP
SAMPLE COMPARTMENT
BAND HEATERS
GENERAL VALVE
B
A
INTERFACE
MICRO-COMPUTER
BOXCAR INTEGRATOR

minimize scattered light arising from the entrance and exit windows of the laser beam is by a series of sharp-edged baffles. The laser baffle arms used in our experiment are similar to the design by Mazur [72]. They are constructed from aluminum tubing, 20" long, 2" o.d. Inside each tube are three conical baffles (3 mm, 4 mm, 5 mm opening); as shown in Figure 2-4, these conical baffles trap any light scattered from the path of the beam. The baffles are separated by aluminum spacers, and the entire assembly is black anodized. The baffle arms are sealed by quartz windows (ESCO Optics, S1-uv, 1.5" dia, 0.125" thick) glued onto Pyrex tubes cut at the Brewster angle and connected to the arms by Cajon fittings. The windows also have a Wood's horn light trap blown below the Pyrex tubes.

The detection optics of the supersonic jet apparatus is shown in Figure 2-5. The vacuum chamber is fitted with two windows made of 2.5" diameter × 1/16" thick quartz plates (ESCO Optics grade s1-uv) pressed against O-rings. The first lens, L1, is a 5 cm, f/1 synthetic fused silica symmetric bi-convex lens (Melles Griot, 01LQD005) which is used to collect the laser-induced fluorescence for the total fluorescence experiment. (Although this single collection lens arrangement can be replaced by two plano-convex lenses or two achromats to correct the aberation of a single lens, the high cost of such quartz lenses offsets the minimal gain in the correction.) The photomultiplier (RCA 8850) is housed in a

Figure 2-4 Entrance or exit arm with light baffles and Brewster angle window. The light baffles are mounted inside the arm by four rods so they can be interchanged and aligned easily.

Figure 2-5 Schematic diagram of the optical detection system for laser-induced fluorescence from jet-cooled molecules.

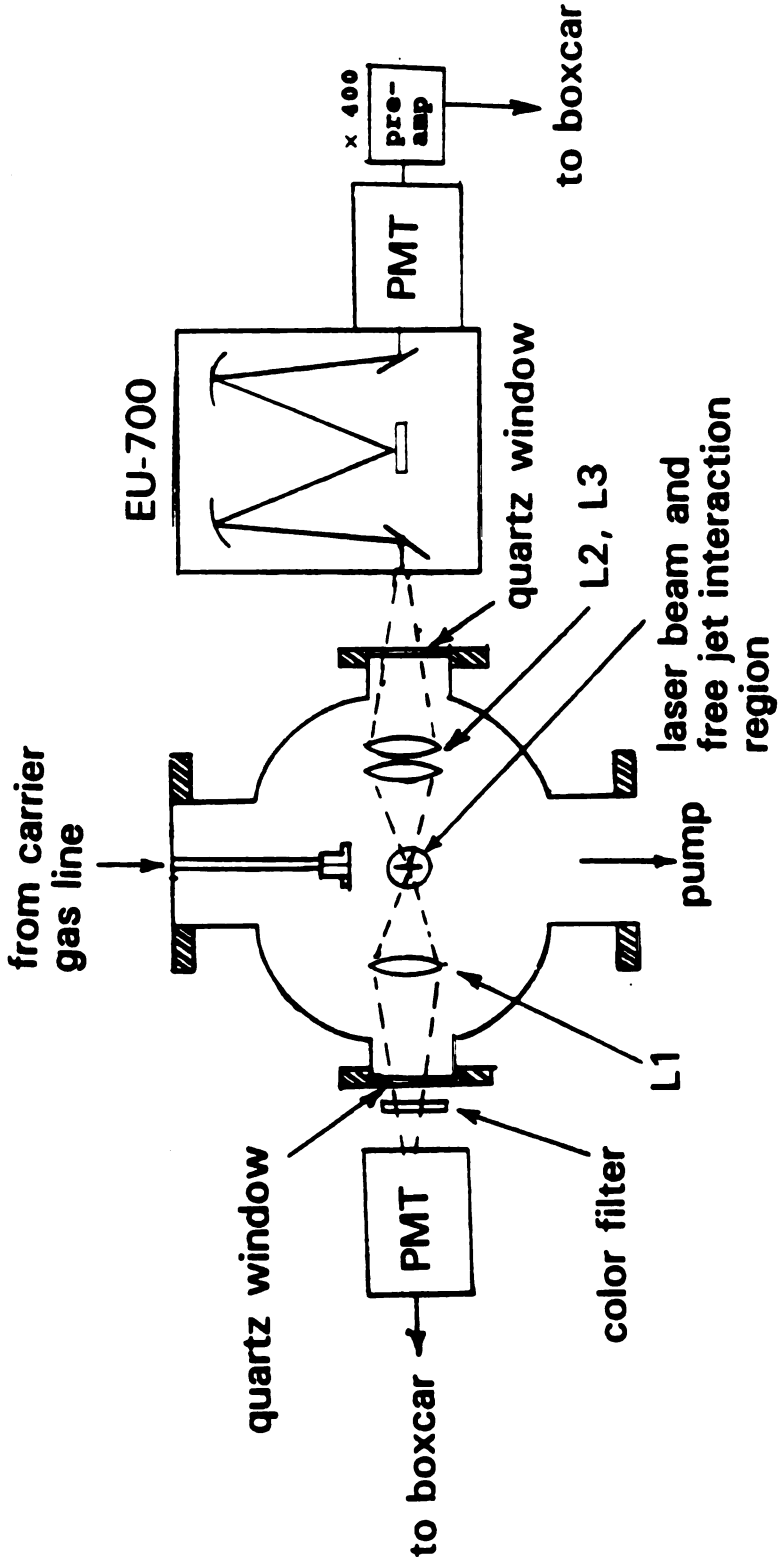
from carrier gas line
quartz window
to boxcar
PMT
color filter
L1
pump
laser beam and free jet interaction region
L2, L3
quartz window
EU-700
PMT
x 400
pre-amp
to boxcar

thermoelectrically cooled housing (Pacific Photometric Instruments, 57W), and the output of the photomultiplier is sent to a boxcar integrator (SRS, 250). On the opposite side from L1 is a two-lens system used for the dispersed fluorescence experiments. L2 is a uv grade biconvex 5 cm f/2 lens (Melles Griot, 01LQD013) which serves to collect the fluorescence and focus the light onto L3, and L3 is a fused silica biconvex 5 cm f/7 lens (ESCO Optics, A1200140) chosen to match the monochromator f number. The photomultiplier (Hamamatsu R562) at the exit of the monochromator is also in a thermoelectrically cooled housing (Products For Research, TE-104TS). The output of this photomultiplier is amplified by a 400 × pre-amplifier (Analog Modules Inc., 322A-5-B-200) before being sent to the boxcar.

The laser systems employed in the experiments described in this dissertation are Nd:YAG pumped dye laser systems. The primary wavelength, 1064 nm, of the Nd:YAG laser (Spectra-Physics, DCR-2) is used for non-linear conversion to shorter wavelengths through harmonic generation, and mixing for sum or difference frequency generation. The output from the YAG laser passes through a second-harmonic generator (Spectra-Physics, HG-2) which converts the primary wavelength to 532 nm. Second harmonic generation is achieved by using KD^*P crystals cut for the proper phase-matching angle. The frequency doubled radiation is used to pump the tunable dye laser (Spectra-Physics PDL-2). Other alternatives are to use

fundamental or other harmonics to pump appropriate dyes. The dye laser can generate wavelengths from 420 nm to 800 nm. Wavelengths shorter than 420 nm can be generated by an automatic tracking wavelength extension system (Spectra-Physics, WEX-1) The existing crystal modules in this system consists of a set of four $LiNbO_3$ crystals used to generate wavelengths from 260 nm to 350 nm for second harmonic generation and 335 nm to 420 nm for the sum generation with the 1064 nm fundamental beam. (C2: 288 nm to 353 nm, C3: 267 nm to 290 nm, C4: 259 nm to 270 nm, C1: 335 nm to 432 nm; C2-C4 are used for doubling dye output, and C1 is used in mixing doubled dye + 1064 nm)

II-3. Pulsed molecular beam sources

Supersonic beams offer many important advantages for molecular spectroscopy. As discussed in Sec. 2-1, the cooling in a supersonic beam is proportional to both the diameter of the nozzle opening and the carrier gas pressure. It is advantageous to use large values of both, but unfortunately this will create a large gas load for the pumping system. One of the requirements of a conventional continuous nozzle beam apparatus is that it utilies either a fairly large vacuum pumping system or incorporates one or more stages of differential pumping to handle the tremendous throughout from

the continuous beam source. However, the pumping requirements can be reduced by using of a fast pulsed molecular beam valve to control the gas flow through the nozzle. This is especially practical in many spectroscopic experiments which use low repetition rate pulsed lasers (e.g. the 10 Hz nanosecond Nd:YAG laser described above), since the low duty cycle of the pulsed laser does not require the unbroken duty cycle of a continuous source.

Molecular beam pulses can be formed by either pulsing the beam source itself or by using a shutter (chopper) that interrupts the beam. We will discuss the former in this section. In the past ten years, various sorts of pulsed valves have been developed [73]. The three commonly used pulsed valve designs are based on: current-loop mechanism, piezoelectric mechanism, and solenoid mechanism. The pulsed valve based on the current loop mechanism was first developed by Gentry and Gieze [74]. The basic principle of operation of this mechanism is very simple; the device (see Figure 2-6(a)) consists of a faceplate and a flexible metal bar formed into a slight loop which is clamped on both ends with an insulator separating the top (metal bar) and bottom pieces (faceplate). A hole is drilled in the bottom plate and sealed by an O-ring. When current pulses through the loop, the opposing magnetic fields set up by the current will push the bar away from the faceplate and cause a displacement which breaks the O-ring seal and allows gas to flow through the

Figure 2-6 Pulsed molucular beam valves. (a) Current loop valve; (b) Solenoid valve (General valve, series 9).

(a)

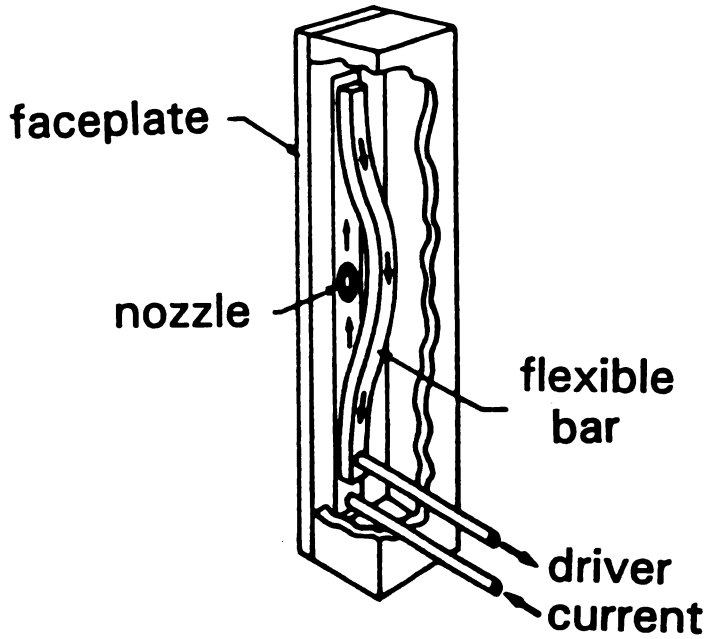
faceplate
nozzle
flexible bar
driver current

(b)

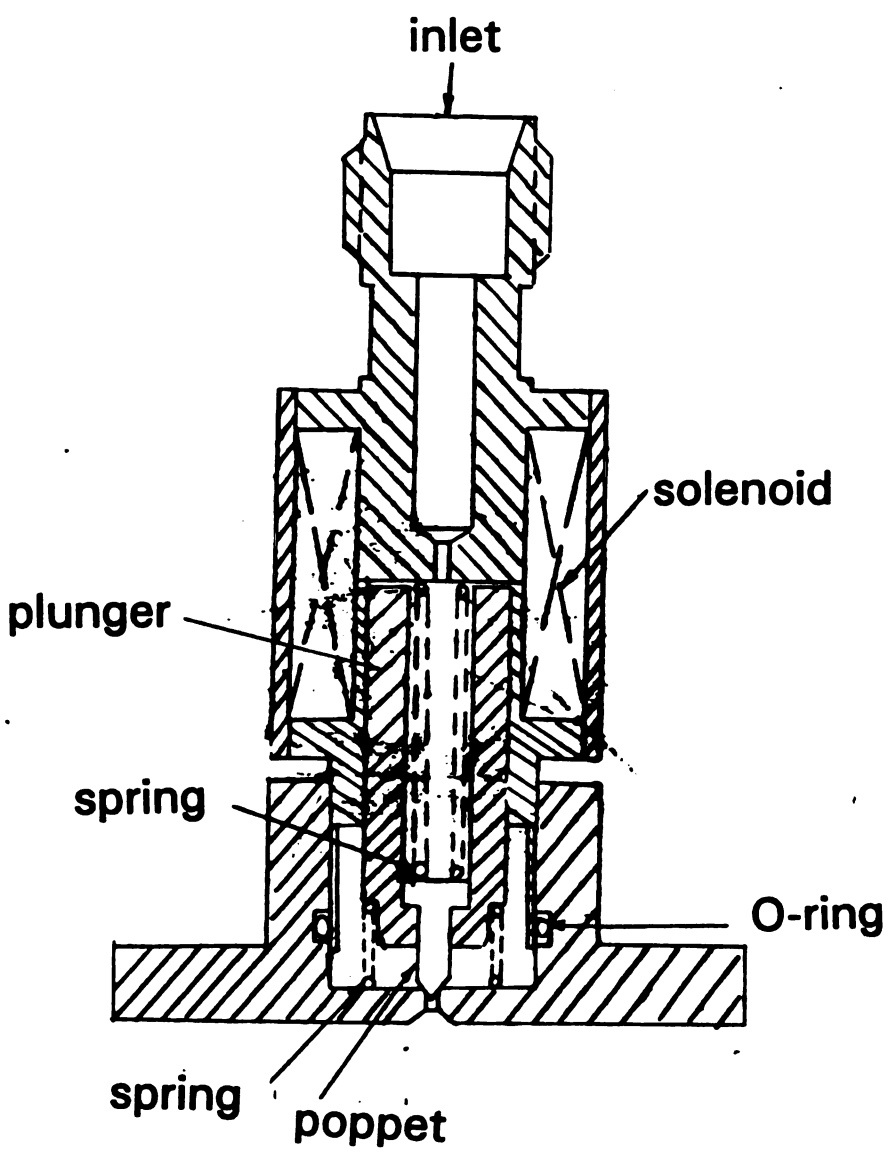
inlet
solenoid
plunger
spring
O-ring
spring
poppet

nozzle. A major advantage of this type mechanism is that it generates very fast pulses; this is especially important in experiments which require good time-of-flight resolution. The shortest pulse generated by this mechanism is 7μs. However, the driving force needed to create short pulses is great. The power source for the fast pulsed valve should be able to charge 2μF capacitors up to 4000 V at a current of 80 mA.

The valve actuating mechanism based on the pizoelectric effect was first intruduced by Auerbach and McDiarmid [75], and by Cross and Valentini [76]. Both of these valves are modified versions of the Veeco leak valve. The piezoelectric crystal is a thin circular disk glued onto an aluminum plunger; a viton tip on the plunger seals directly on the inside of the nozzle. The main advantages of the pizoelectric valve are that they are suited to function at very high repetition rates (up to 750 Hz) and that they require very small amounts of power to operate.

Probably the most popular pulsed valve sources for spectroscopic experiments are the solenoid valves [77]. The solenoid valves are operated by passing a current pulse through a solenoid (coil), which exerts a magnetic force on a ferromagnetic core (plunger) material, e.g. iron. There are many commercial solenoid valves available. One of the most commonly used solenoid valves is a simple automobile fuel injector; Bosch and Honda are two popular brands. Adams et al. [78] have designed a more sophisticated solenoid valve in

which two solenoids are used in one valve, one to open and one to close the valve. The main advantages of solenoid valves are that they are simple to build and inexpensive; furthermore, they generate pulses with widths of a few hundred microseconds and can be operated at modest rates (1-100 Hz).

An important limitation of all the pulsed valves is that the maximum operating temperature is roughly 200^0 C. This limit is due to the material used to construct the valve and the material used to seal the valve when it operates in vacuum. O-ring seals and electrical insulation are the most heat sensitive areas in the nozzle design. Amirav et al.[66] have reported a pulsed valve capable of operating in the temperature range 20^0 C - 520^0 C; to date this is highest temperature that any pulsed valve can maintain.

The pulsed valve used in our experiments (shown in Fig. 2-6(b)) is a series 9 high speed solenoid valve purchased from General Valve Co. The design of this valve is similar to the fuel injector valve, except it is made for molecular beam laser spectroscopy experiments; there have been wide applications of this valve and its modified versions. Based on this valve, we have built two pulsed nozzle assemblies for high temperature experiments. The schematic diagram of the first high temperature nozzle assembly is shown in Figure 2-7; we followed a similar nozzle design from D. H. Levy's laboratory. The main feature of this high temperature nozzle

Figure 2-7 Levy-type pulsed nozzle assembly. The assembly made for high temperature experiments, consist of the solenoid valve made by General Valve Co. The sample tube is heated by five cartridge heaters, and temperatures higher than 400^0 C can be obtained. The pulsed nozzle, separated from the oven, is cooled by an internally drilled mounting block through which cooling water is run.

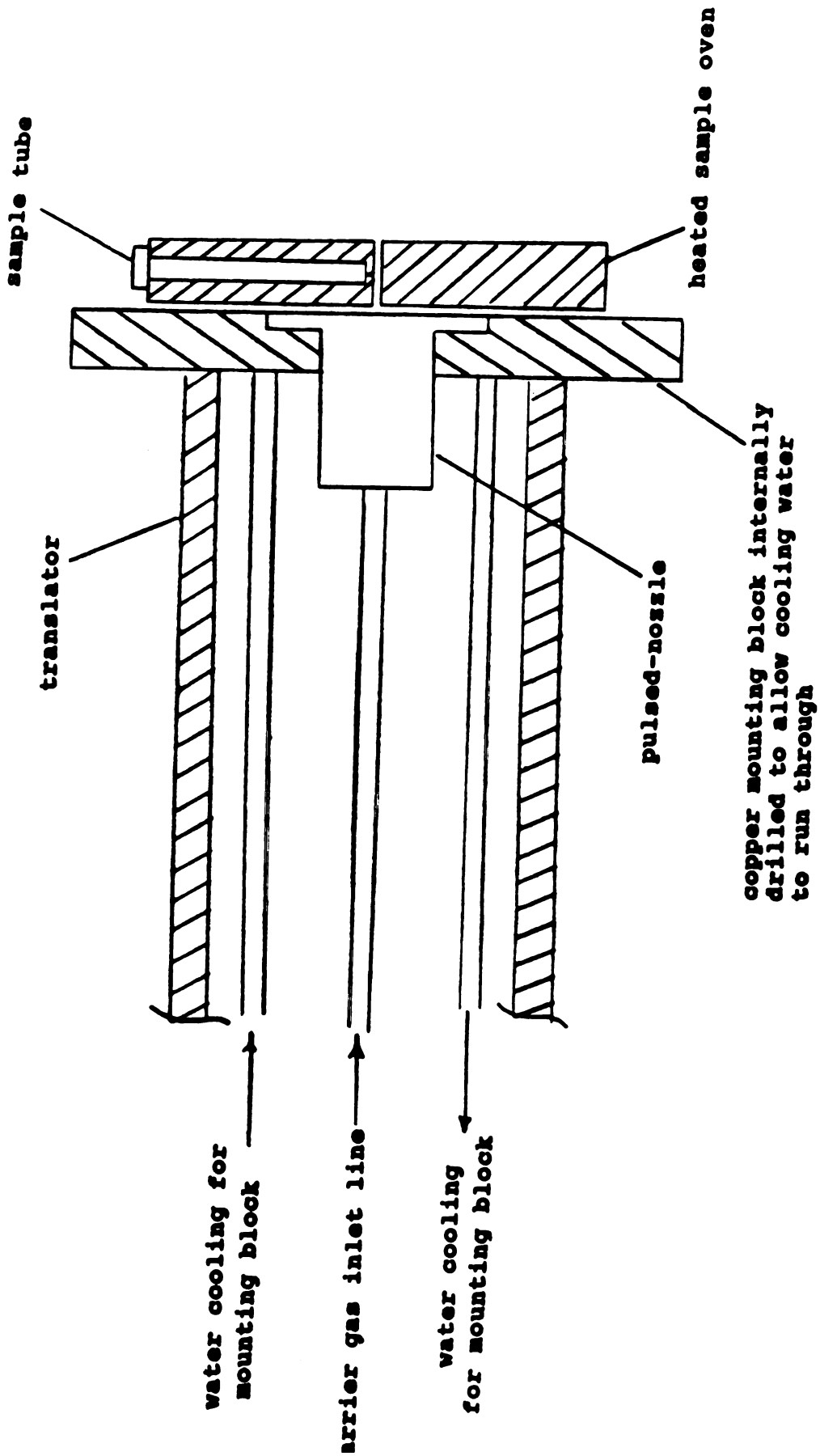
sample tube
heated sample oven
translator
pulsed-nozzle
copper mounting block internally
drilled to allow cooling water
to run through
water cooling for
mounting block
arrier gas inlet line
water cooling
for mounting block

assembly is that the sample oven is a separate piece from the pulsed-nozzle, so that the nozzle itself is not heated. As shown in Figure 2-7, the series 9 pulsed valve and the sample oven are attached to the xyz-translator. (This translator is built to be mounted onto the chamber shown in Figure 2-9(a).) The oven is made of copper and heated by five cartridge heaters (Watlow, G1A38). The sample tube is screwed into the heated sample oven, also made of copper. Around the series 9 pulsed valve is an internally drilled cooling block which allows cooling water to run through and isolate the pulsed valve from the heat generated by the heated oven. This nozzle assembly has been used in experiments operated at temperature as high as 400^0 C.

The second pulsed nozzle assembly (shown in the insert in Figure 2-3) was also constructed from a General valve series 9 molecular beam valve, but one with a high temperature solenoid (9-279-050) with 760 μm diameter orifice. (We have been told by the General Valve Co. that this coil can be heated up to 250^0 C.) The sample and the pulsed valve are heated separately by two band heaters (Watlow, MB1A), thus enabling the valve to be kept at a higher temperature than the sample. The temperatures were monitored by two chromel-alumel thermolcouples.

The circuit diagram for the pulsed valve controller is given in Figure 2-8 (this circuit was designed by D. Smith of the University of Chicago). The controller can be triggered

Figure 2-8 Circuit diagram for pulsed valve controller

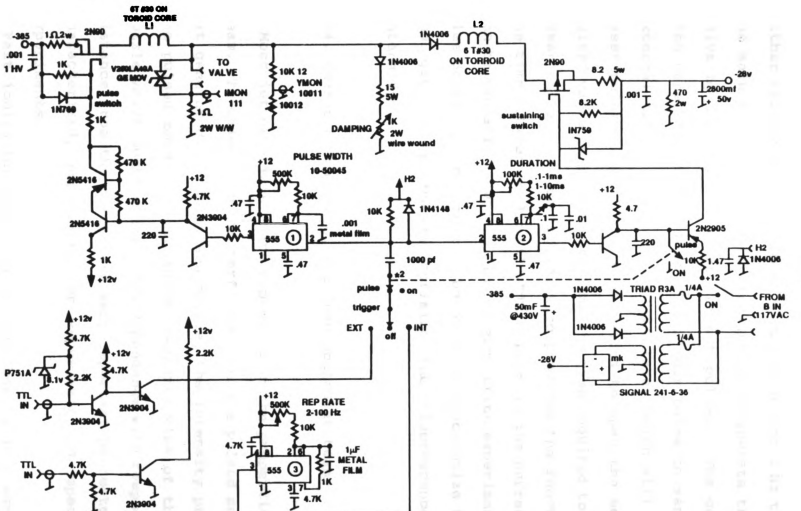
2N3904
67 #30 ON TOROID CORE
L1
-385
1Ω 2w
2N90
.001
1 HV
1K
V385LA40A
GE MOV
TO VALVE
IMON 111
1Ω 2W W/W
10K 12 YMON 10011 10012
1N4006
15 5W
DAMPING
1K 2W wire wound
1N4006
L2
5 T #30 ON TORROID CORE
2N90
8.2 5w
-28v
.001
470 2w
2800mf 50v
8.2K
sustaining switch
IN759
1N760
pulse switch
1K
470 K
2N5416
470 K
2N5416
1K
+12v
PULSE WIDTH 10-50045
+12
500K
10K
.47
+12
4.7K
2N3904
10K
220
555
.001 metal film
.47
H2
10K
1N4148
1000 pf
+12
DURATION
100K
1-1ms
1-10ms
10K
.47
555
.01
+12
4.7
10K
220
2N2905
pulse
10K
1.47
H2
1N4006
ON
+12
pulse
trigger
EXT
on
off
INT
-385
1N4006
TRIAD R3A
1/4A
ON
FROM B IN 117VAC
50mF @430V
1N4006
1/4A
-28V
mk
SIGNAL 241-6-36
+12v
4.7K
+12v
4.7K
P751A
.1v
2.2K
TTL IN
2N3904
2N3904
+12v
2.2K
+12
500K
REP RATE 2-100 Hz
10K
4.7K
555
1μF METAL FILM
1K
4.7K
TTL IN
4.7K
4.7K
2N3904

either externally or internally at a rate from 1 Hz to 100 Hz. The main function of the controller is to operate the pulsed valve by sending out short current pulses. The controller also generates a 15 V 10μs TTL trigger pulse to send to the external trigger input of the YAG laser which will fire the laser pulses. Since the time needed to open the mechanical pulsed valve is much longer than the time required to fire the laser pulses, the controller also provides the function that the time between sending the TTL pulses and the current pulses can be manually adjusted. In the excitation experiments, this time delay control actually helps us to synchronize the laser and gas pulses and to optimize the fluorescence signal intensity.

2-4. Characterization of a pulsed molecular beam

Most jet experiments are dependent on the properties of the beam. To understand the performance of the pulsed supersonic jet generated by the pulsed nozzle, the intensity profile of the pulsed beam, the mechanical response time of the pulsed nozzle valve, and the intensity dependence with respect to the distance from the nozzle are very important parameters to be characterized, especially for supersonic jet spectroscopy experiments.

Fast ionization gauges (FIG) have been widely employed to monitor and to characterize pulsed beams [74]. A FIG which

is employed to monitor pulsed molecular beams should have the following characteristics:

(1) linear pressure response up to high pressure (~ 10^{-2} torr), so the intensity can be monitored near the pulsed nozzle.

(2) the gauge itself must have an open structure.

(3) fast rise time.

The geometry of a common FIG is similar to a standard Bayard-Alpert gauge tube; it consists of a central ion collection wire surrounded by a helical grid and a filament on the outside. The first requirement can be satisfied by making the distances filament-to-grid and grid-to-collector small. To achieve fast rise time, an operational amplifier with high gain-bandwidth should be located as close to the collector as possible.

We have performed a series of experiments with a FIG manufactured by R. M. Jordan Co. These experiments were carried out: (1) to understand the local environment in the laser and free jet interaction region, and (2) to characterize the time profile of the gas pulses and the mechanical response time of the pulsed valve. We have built two vacuum chambers (see Figure 2-9) for supersonic jet experiments. The first is a large stainless steel chamber originally designed to be used as the source chamber in a molecular beam photoionization spectroscopy experiment which had no relation to the supersonic jet spectroscopy project. Some modification was

Figure 2-9 Experimental arrangement for FIG tests in the two experimental chambers

(a) modified photoionization spectroscopy chamber;

(b) chamber in which emanating spectroscopy jet is directly pumped.

(a)

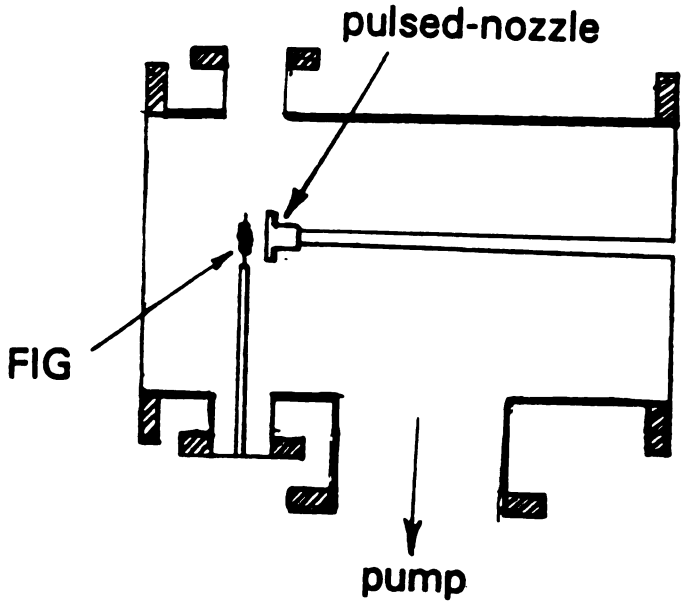

(b)

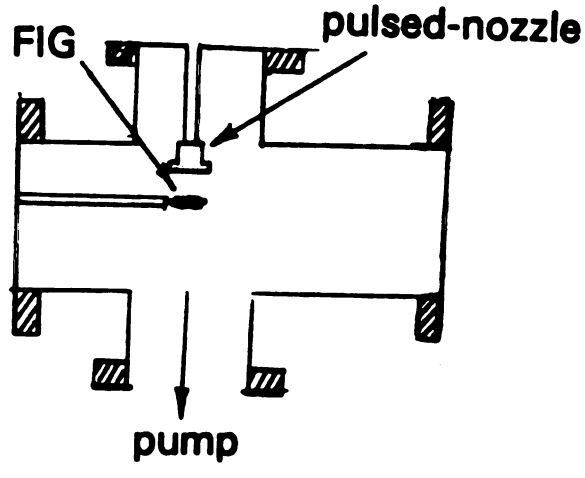

done on this chamber so it could be used for the fluorescence excitation experiments. One severe drawback of this chamber is that the position of the nozzle is unavoidably too close to one chamber wall; the geometry and the welding of the original chamber precluded any possiblity of opening a port in the central area of the chamber. The closeness of the nozzle to the wall posed the question: Will the local environment of the expanded jet be affected by this arrangement? The FIG tests can provide direct information in this regard.

The Jordan FIG is a Bayard-Alpert type high vacuum gauge (see Figure 2-10) on which the grid dimensions have been reduced to increase the speed of response; this FIG is capable of monitoring the time profile of a 50 μs FWHM pulsed beam. The emission current, which is generated by the electrons being emitted from the filament to the grid, is limited to 10 milliamps. The circuit for the collector amplifier designed by M. Rabb is shown in Figure 2-11. The FIG is controlled by an old ionization gauge controllor (Veeco RG-830), which is used to provide the grid voltage and the protection circuit. The protection circuit will turn the filament off when the average pressure at the FIG is higher than a preset value. To observe a pulsed beam profile, the output of the FIG is first amplified, then connected to an oscilloscope (Tektronix 7940) input, and the scope is triggered by the valve driver. The FIG signal on the scope screen is recorded by an

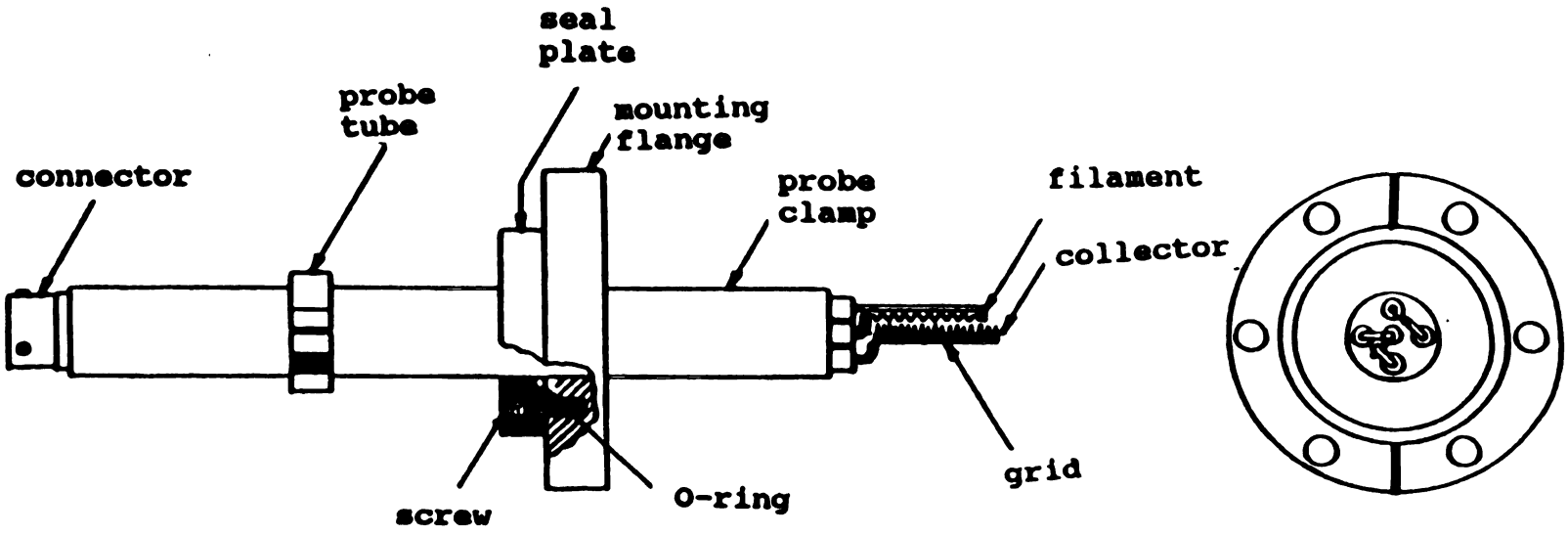

FIGURE 2-10 FIG probe assembly

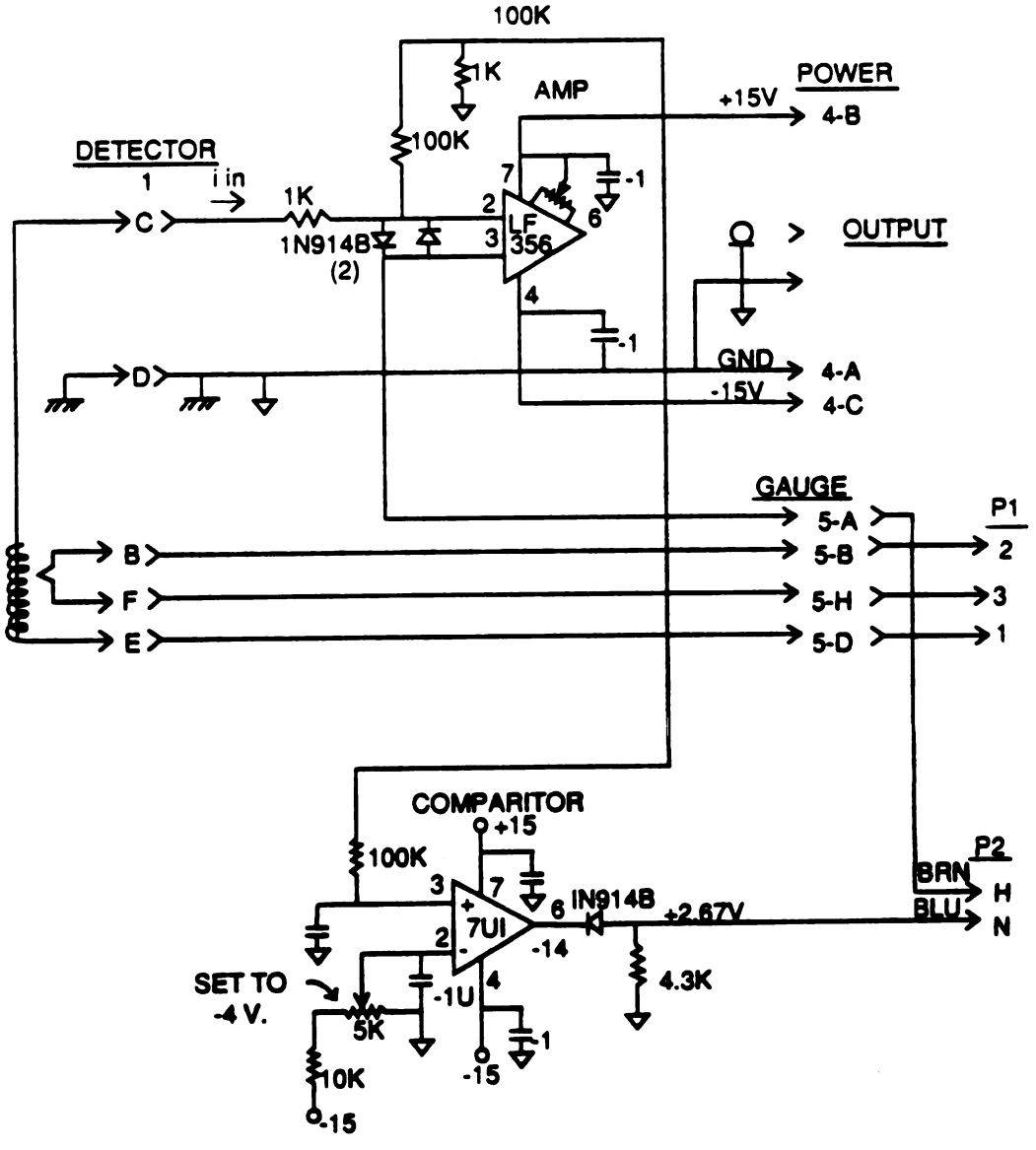

FIGURE 2-11 FIG amplifier circuit

oscilloscope camera (Tektronix C-12).

The performance of the General pulsed valve is illustrated in Figure 2-12. The traces in Figure 2-12 were obtained with a triggering rate of 10 Hz and backing pressure of 1 atm. Each trace represents the average of several successive pulses. The FIG is positioned downstream from the valve exit at (a) 3 cm, (b) 3.8 cm, (c) 3.3 cm, (d) 2.3 cm, (e) 1.8 cm. The test results for the first vacuum chamber are shown in Figure 2-12(a); the upper trace is the output from the FIG, and the lower trace is the current pulse from the pulsed valve driver, which is used to open the valve. Figures 2-12 (b)-(e) show the results from the FIG tests for second vacuum system under the same backing pressure. (Note that the FIG signal is the lower trace in these figures, and the displaying scale is 10 mV/cm) If the FIG output in Figure 2-12(a) is compared with Figures 2-12 (b)-(e), a significant difference in the amplitude and the shape of the FIG output signal is observed. In Figure 2-12(a), the output from the FIG has saturated the amplifier (note the signal is recorded on a 5 Volt/div scale), and the shape of the signal is unsymmetric; both observations strongly indicate that reflection from the chamber wall indeed occurred. The results of removing the wall are that the FIG signal has much lower amplitude, and the shapes are more symmetrical. The gas pulse duration has been adjusted to 0.3 ms FWHM in these tests. The time required to open the valve is very useful to know, since the optimization

Figure 2-12 Pulsed beam intensities monitored by the FIG. (a) The original vacuum chamber, FIG positioned 3.0 cm downstream from the nozzle; (b) - (e) The new vacuum chamber, with downstream FIG locations of 3.8, 3.3, 2.3, 1.8 cm, respectively. Upper traces: current pulse from valve driver; lower traces: amplified FIG output (These are reversed from Figure 2-12 (a).) The FIG signal intensity decreases as the distance from the FIG to the pulsed nozzle increases.

(c)

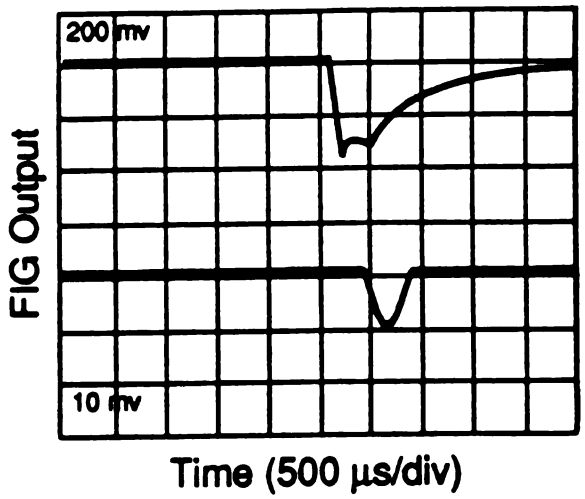
200 mv
FIG Output
10 mv
Time (500 µs/div)

(d)

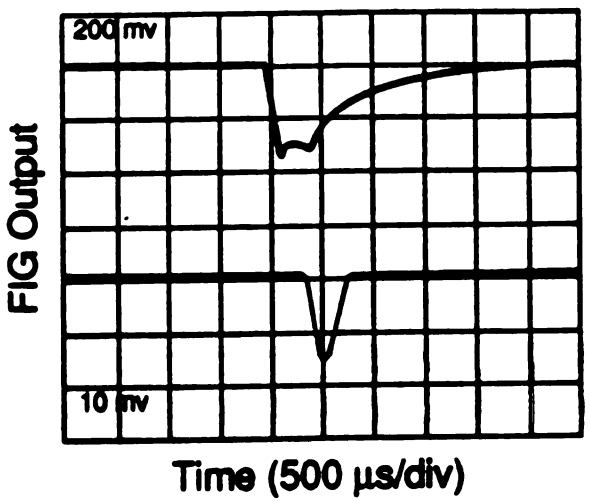
200 mv
FIG Output
10 mv
Time (500 µs/div)

(e)

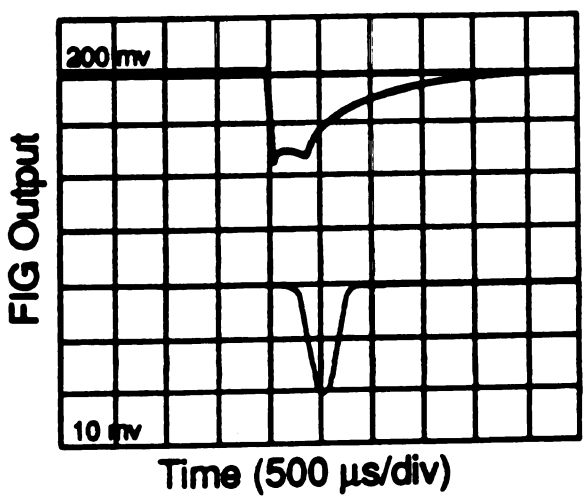
200 mv
FIG Output
10 mv
Time (500 µs/div)

(a)

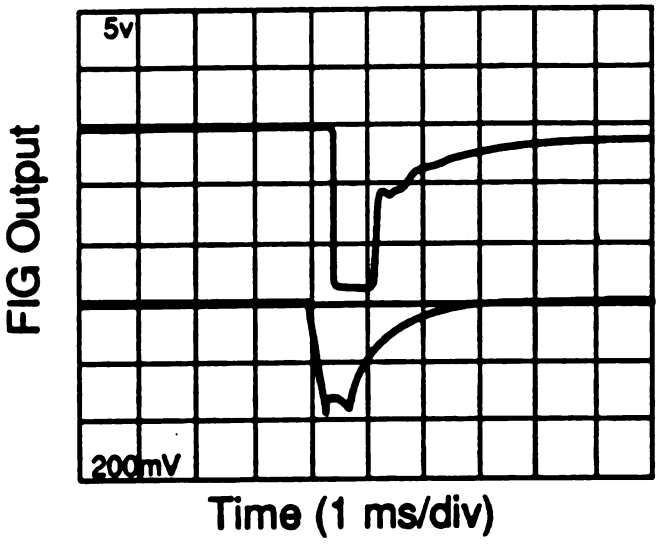
5v
FIG Output
200mV
Time (1 ms/div)

(b)

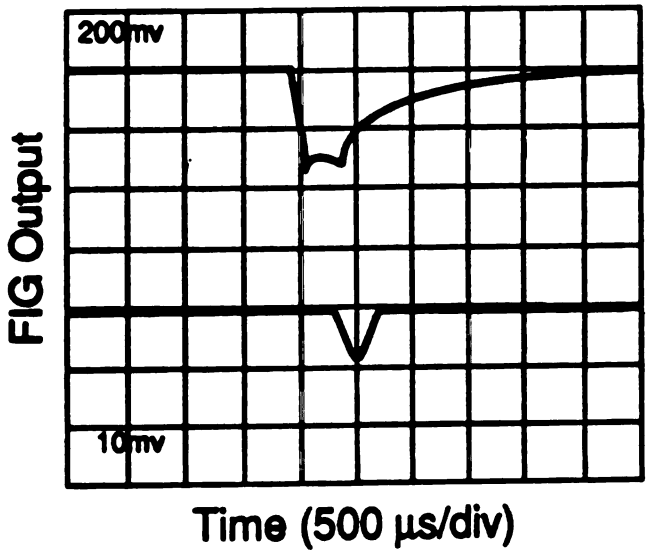
200mv
FIG Output
10mv
Time (500 µs/div)

of the fluorescence signal depends on the timing of the pulsed laser and the pulsed valve; it can be estimated to be 0.4 ms from the oscillogram.

2-5. Perylene experiments

The performance of our supersonic jet apparatus and the advantages of supersonic jet spectroscopy are best understood through actual experimentation with several molecular systems. In the following sections, I will discuss some of the experiments we have carried out. The perylene experiments, for which the objective was to understand the vibrational cooling (vibrational relaxation) in the jet, serve as a probe to explore the experimental conditions which can be achieved by our intruments. (The sectroscopy of perylene itself is surely an interesting subject; in fact, one of the goals we initially set for the supersonic jet project was to detect the electronic symmetry-forbidden states of perylene by two photon spectroscopy.) The aniline experiment was initiated based on another long-term interest of this project: to study chemistry within clusters generated in supersonic jets. However, the preliminary results indicate that although we obtained sufficient cooling to eliminate most hot vibronic bands, we were not able to generate Ar-aniline clusters with the current apparatus.

Perylene can be viewed as a molecule comprised of two weakly bonded naphthalene molecules. In contrast to naphthalene, which absorbs in the ultraviolet region, and also in constrast to five-and six-ring condensed hydrocarbons which absorb on the long wavelength side, perylene shows intense absorption in the visible region, with the first maximum at about 435 nm (in solution). There have been extensive early studies on absorption and fluorescence spectra of perylene in Shpolskii matrices [79,80]. Because of perylene's size, the spectral linewidths were 10-20 cm^{-1} at 77 K, and narrower in lower temperature matrices.

Recent interest in perylene originated from the study of IVR of large aromatic molecules in jets [81-83]. By using dispersed fluorescence spectroscopy from the first excited state in jet-cooled perylene, it was found that vibrational states low in the S_1 manifold ($E_{vib} < 700$ cm^{-1}) showed no IVR in the time scale of emission, while those high in the manifold ($E_{vib} \rangle$ 1600 cm^{-1}) showed strong IVR. For the intermediate region, the fluorescence consists of resonance emission and non-resonant ("relaxed") bands; this can be explained by "restricted IVR".

The relevant portion of the vibronic analysis of perylene is summarized in Table 2-1. In the low frequency region, we can expect the out-of-plane (non-totally symmetric) modes rather than the in-plane modes. These low-frequency modes are of special interest. One is the so-called "butterfly" out-

TABLE 2-1 Ground- and first electronic excited-state frequencies of optically active modes in perylene*.

mode	ground state	excited state
A	353	352
B	427	426
C	547	548
D	1300	1292
E	1372	1398
F	1580	1603
G	24.5	48

* reference [83]

of-plane mode - the G mode; information about the rigidity of the molecule with respect to the planar structure can be inferred from this vibrational mode. The butterfly mode cannot be observed directly in infrared and Raman spectra of perylene in crystalline matrices, where the low-frequency vibrations are strongly mixed with lattice-modes.

The fluorescence excitation spectra of the S_1 <--- S_0 transition of perylene shown in Figures 2-12 to 2-16 was recorded by laser excitation of molecules cooled in the supersonic jet. The positions of the peaks near the origin at 24056 cm^{-1} are listed in Table 2-2. The most interesting spectral features in this region are a band located at 95 cm^{-1} and a hot band sequence shifted to the blue by 24.5 cm^{-1}, 44.5 cm^{-1} and 65 cm^{-1}. The assignment of the hot bands is based on the decrease of their intensity with an increase in the backing pressure. The sequence bands in the 0-81 cm^{-1} (0 cm^{-1}, 22 cm^{-1}, 42 cm^{-1}, 63 cm^{-1}, 81 cm^{-1}) above the origin can be assigned to the G^0_0, G^1_1, G^2_2, G^3_3, G^4_4 transitions. The 95 cm^{-1} band is assigned to a transition of the G mode with two quanta excited in the excited electronic state. This low frequency non-totally symmetric vibration follows the selection rule $\Delta v = 0, 2, 4, \ldots$; thus the excited state vibrational level separations are $\approx$ 48 cm^{-1}. Four more transitions have been observed in the excitation spectrum above 95 cm^{-1}. From the energies of these bands, plausible assignments would be G^3_1, G^4_2, G^5_3, G^6_4; however, the relative intensities do not support

TABLE 2-2 Observed transition energies (cm^{-1}) near S_1 <---S_0 in the fluorescence excitation spectrum of perylene

Wavenumber	Relative to origin	assignment
24056	0.0	origin
24078	22	G^1_1
24098	42	G^2_2
24119	63	G^3_3
24137	81	G^4_4
24151	95	G^2_0
24175	119	
24197	141	
24220	164	
24249	193	

Figure 2-13 Fluorescence excitation spectrum of perylene from 416 nm to 412 nm, taken with 760 μm pulsed nozzle at a carrier gas pressure P_{Ar}= 15 psig.

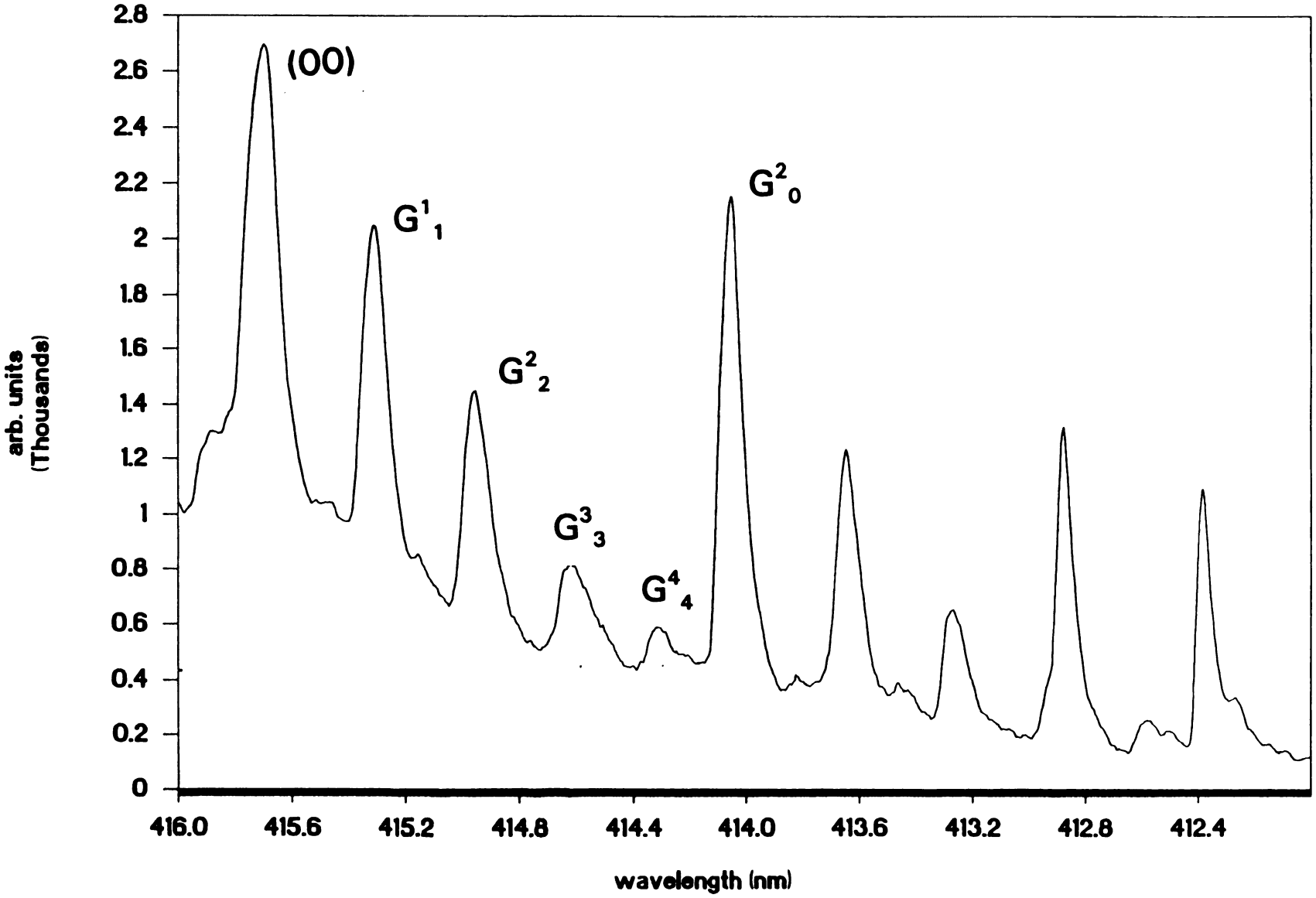
(00)
G^1_1
G^2_2
G^3_3
G^4_4
G^2_0
arb. units
(Thousands)
2.8
2.6
2.4
2.2
2
1.8
1.6
1.4
1.2
1
0.8
0.6
0.4
0.2
0
416.0
415.6
415.2
414.8
414.4
414.0
413.6
413.2
412.8
412.4
wavelength (nm)

Fig. 2-14 Fluorescence excitation spectrum of perylene from 416 nm to 412 nm, taken with pulsed nozzle at P_{Ar}= 30 psig.

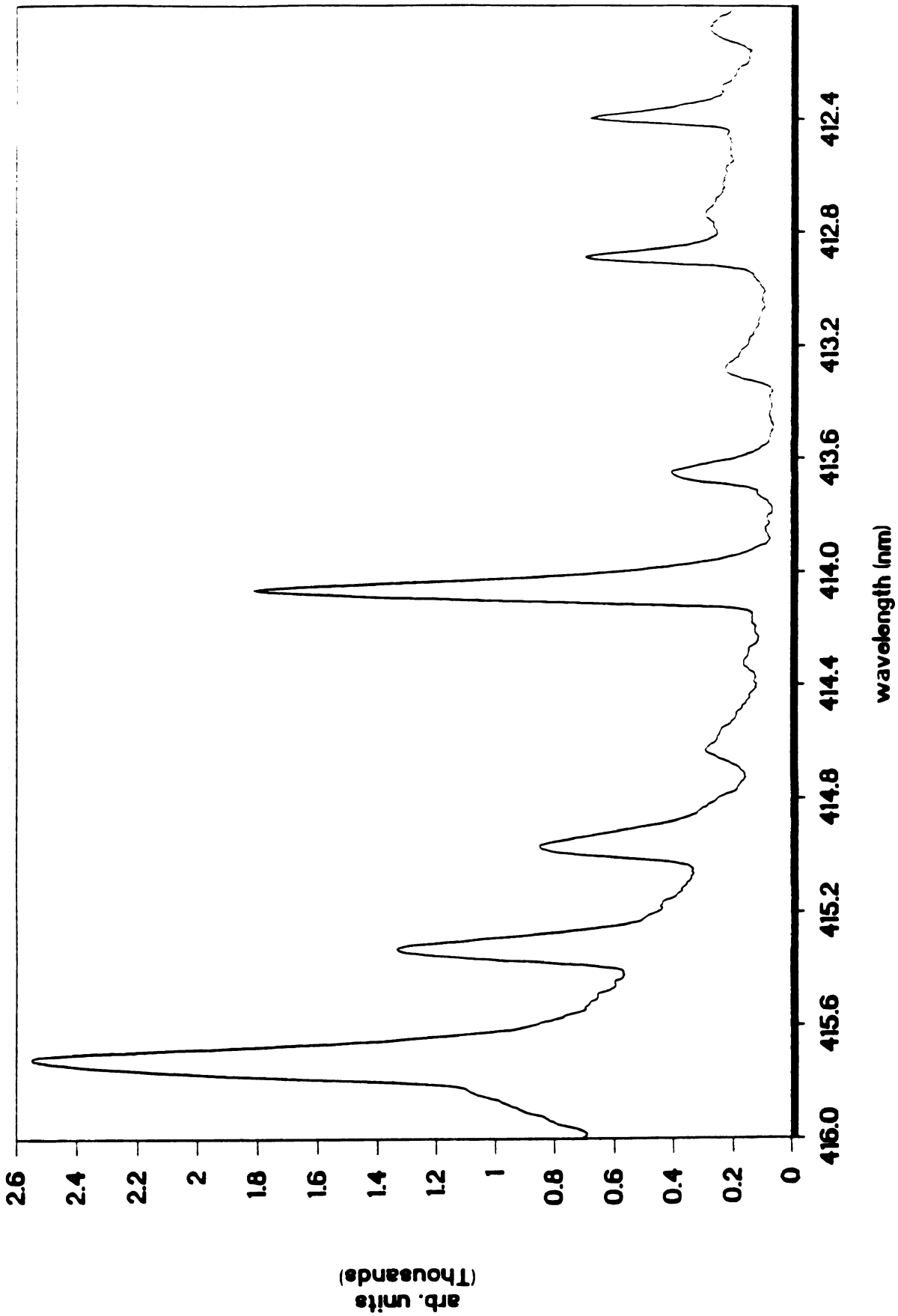
arb. units
(Thousands)
2.6
2.4
2.2
2
1.8
1.6
1.4
1.2
1
0.8
0.6
0.4
0.2
0
416.0
415.6
415.2
414.8
414.4
414.0
413.6
413.2
412.8
412.4
wavelength (nm)

Fig.2-15 Fluorescence excitation spectrum from 416 nm to 412 nm, taken with pulsed nozzle at carrier gas pressure P_{Ar}= 45 psig.

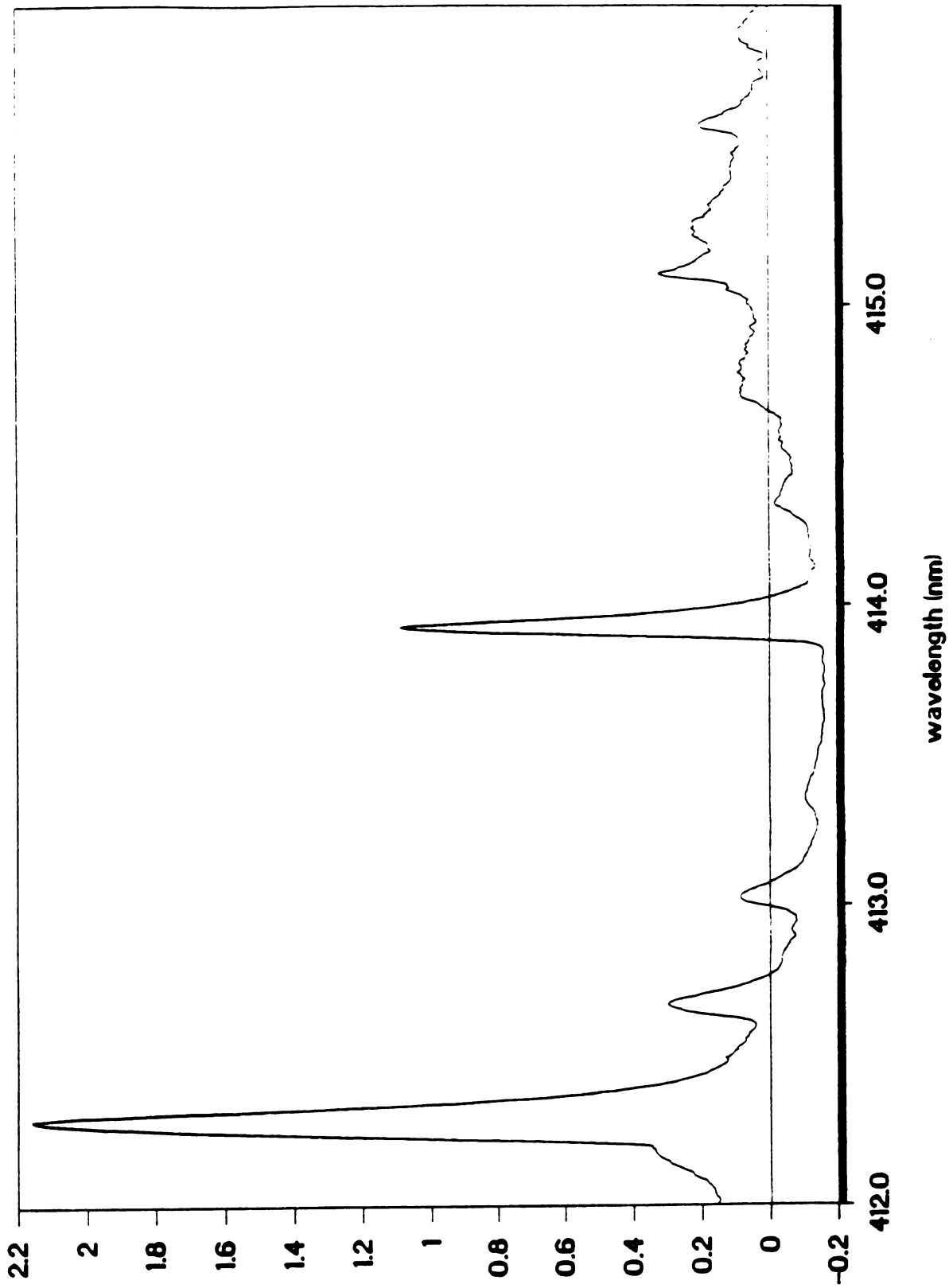
arb. units
(Thousands)
2.2
2
1.8
1.6
1.4
1.2
1
0.8
0.6
0.4
0.2
0
-0.2
412.0
413.0
414.0
415.0
wavelength (nm)

Fig. 2-16 Fluorescence excitation spectrum of perylene from 416 nm to 412 nm, taken with pulsed nozzle at carrier gas pressure P_{Ar}=60 psig.

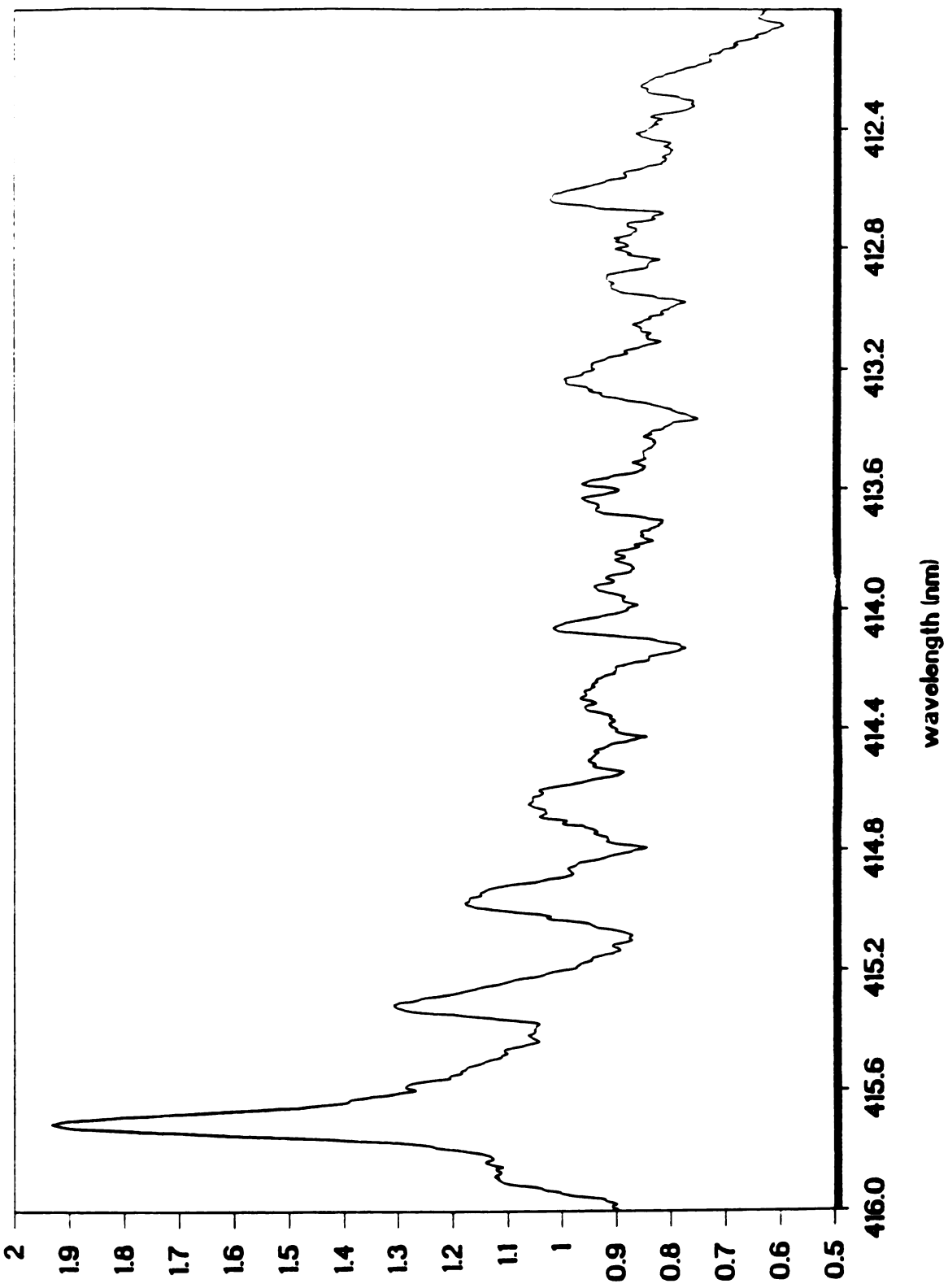
arb. units
(Thousands)
2
1.9
1.8
1.7
1.6
1.5
1.4
1.3
1.2
1.1
1
0.9
0.8
0.7
0.6
0.5
416.0
415.6
415.2
414.8
414.4
414.0
413.6
413.2
412.8
412.4
wavelength (nm)

Fig. 2-17 Fluorescence excitation spectrum of perylene from 416.6 nm to 412.6 nm, taken with a 200μm orifice continuous nozzle at a carrier gas pressure P_{Ar}= 15 inHg.

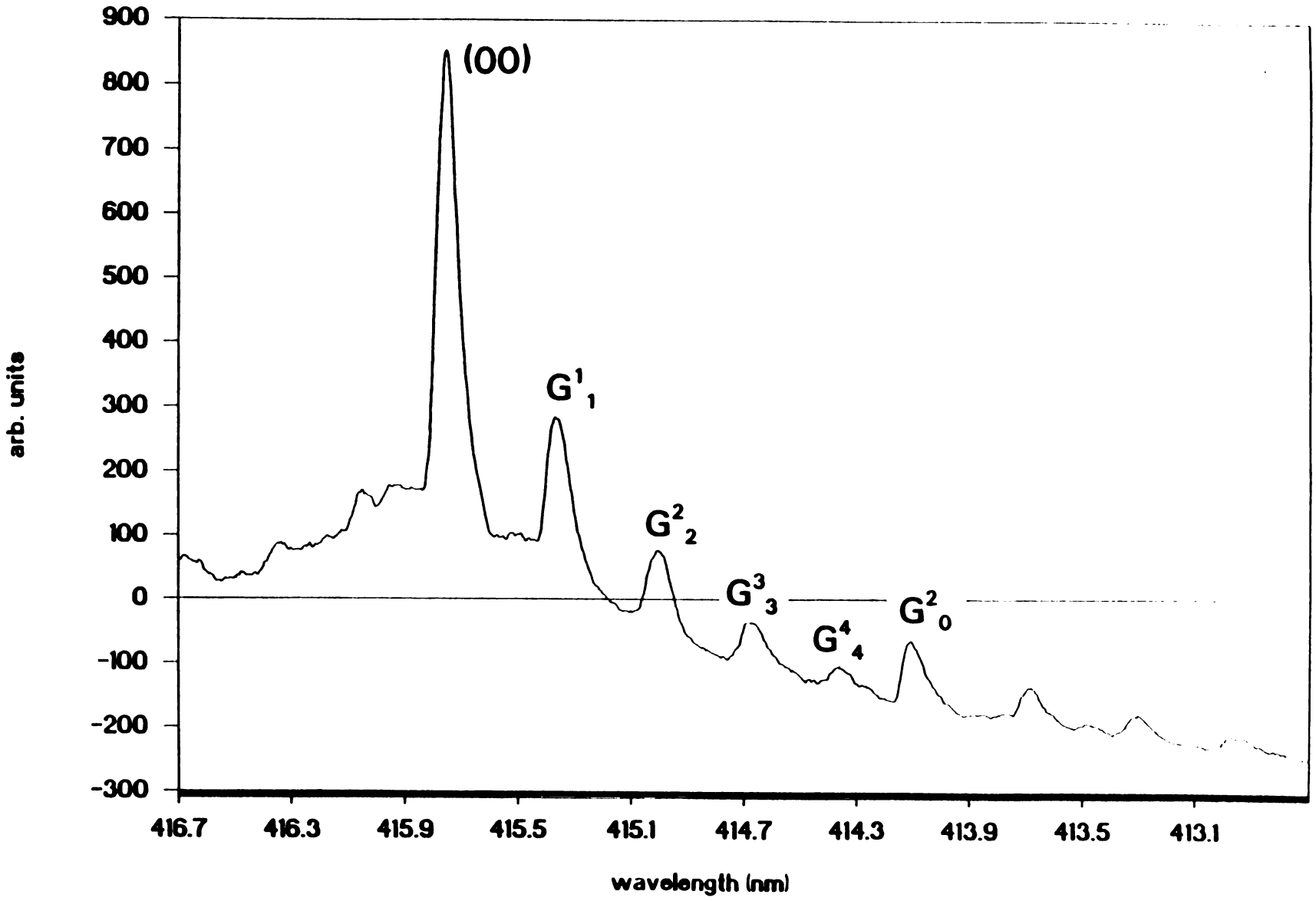
900
800
700
600
500
400
300
200
100
0
-100
-200
-300
arb. units
(00)
G 1 1
G 2 2
G 3 3
G 4 4
G 2 0
416.7
416.3
415.9
415.5
415.1
414.7
414.3
413.9
413.5
413.1
wavelength (nm)

this conclusion. Based on information obtained for this vibrational mode, I shall discuss how the internal temperature of the molecule depends on the jet expansion conditions.

The total number of binary collisions experienced by a molecule in a free jet expansion is on the order of 10^2 to 10^3. The energy relaxation processes in the jet are kinetic processes; therefore, any process that requires a higher number of collisions to reach equilibrium will not go to completion. The vibrational relaxation of a simple diatomic molecule requires more than 10^4 collisions, hence the full vibrational relaxation of diatomic molecules is difficult to achieve. On the other hand, the vibrational relaxation of a large molecule or the rotational relaxation of most diatomics may require on the order of only 10 to 100 collisions. Since the collision rate is proportional to p_0d, it is very easy to control the jet expansion conditions, such as the backing pressure p_0 or nozzle diameter d to understand the relaxation prcesses. Rotational relaxation processes in free jets have been studied extensively in the past [84]. Vibrational relaxation in the supersonic expansion was predicted by Kantrowitz and Gray [54] when the idea of supersonic beams was first conceived; recently there have been many studies of vibrational relaxation in supersonic jets, including I_2 [85,86], Br_2 [87], aniline [88], touluene [89], glyoxal [90], and naphthalene [91]. Much theoretical work has been developed for the collisional relaxation of a simple harmonic

oscillator interacting with a thermal bath [92]. The theoretical results illustrate that an initial Boltzmann distribution can relax to a cooler Boltzmann distribution due to collisions. The general expression for the rate of the relaxation of the vibrational energy is given by [93]

$$dE(T_v)/dt = [E(T) - E(T_v)]/ \tau$$

where $E(T_v)$ is the vibrational energy of a harmonic oscillator with vibrational temperature T_v, and $E(T)$ is the vibrational energy of the oscillator at the local translational temperature T, and τ is the vibrational relaxation time. This relation is referred to as the Landau-Teller relaxation equation. Although the Landau-Teller model is a useful starting point to understand vibrational relaxation, a recent study [85] has shown that the vibrational relaxation in supersonic jet is much more complicated.

The fluorescence excitation spectrum of perylene provides the advantage that the internal temperature of the molecule can be monitored by following the population of the G-mode; the intensity of the prominent sequence bands (G^1_1, G^2_2, G^3_3) can be assumed proportional to the vibrational distribution for the vibrational states $v_G'' = 1, 2, 3$. According to the Boltzmann distribution formula [94,95]

$$R_v = \exp(- \Delta E_v/RT_v)$$

where R_v = the ratio of the peak height of the state v to that for the ground state as a measure of the vibrational population of the state v

ΔE_v = vibrational energy above the ground vibrational state ($\Delta E_v = v\omega_G$, $\omega_G = 24.5\ cm^{-1}$ for the ground electronic state)

T_v = the vibrational temperature that characterizes the population of mode G.

$T_v(^0K)$ can then be derived from the observed intensity ratio R_v,

$$T_v = (hc/k)\ \Delta E_v / \ |\ln R_v|$$

where $hc/k = 1.4839\ ^0K\ cm$; ΔE_v is in cm^{-1}, and R_v is now the ratio of the intensity of the ground vibrational state to that of state v.

From this relationship, the assumption that the G mode is harmonic in the electronic ground state and the assignments in Table 2-2, the vibrational temperature of the G mode under different expansion conditions can be evaluated. Figures 2-12 to 2-16 showed the fluorescence excitation spectra of perylene taken at different carrier gas pressures. The intensities of the sequence bands G^1_1, G^2_2, G^3_3 in these spectra change dramatically according to the varied nozzle operating conditions; this is clearly due to the change in the internal

temperature of the molecule. If we assume the vibrational population follows the Boltzmann law, the vibrational temperature of the G mode can be estimated from the relative sequence band intensities. Figure 2-18 is a least squares plot of $\ln R_v$ versus ΔE_v (v = 0, 1, 2, 3) for Figure 2-14, which indicates the vibrational population corresponds to a Boltzmann distribution with a temperature $T_v \approx 37^0$ K. The accuracy of such plots is affected by the estimation of the peak heights of the sequence bands; since the exact position of the baseline near the electronic origin is uncertain, these measurements provide only a rough estimation. From similar plots performed for the spectra taken at 15 psig and 45 psig, one obtains:

pressure(psig)	$T_v(^0K)$	p_0d (d = 760 μm)torr cm
15	51	58
30	37	118
45	29	177

The best cooling condition we were able to achieve was when p_0 = 45 psig (see Figure 2-15). At this pressure, the first member, G^1_1, of the sequence bands has the lowest peak height relative to the electronic origin and G^3_3 and G^4_4 have been essentially eliminated. On the other hand, the relative intensity of the G^2_0 band, the first member of the v_G'-

Figure 2-18 Plot of $\ln R_v$ vs. ΔE_v. The experimental points (from Figure 2-14) are shown by open squares and the least-squares fit to the four points by a solid line. R_v is the peak height ratio of the ground vibrational state to that of the peak heights of the sequence bands. R_v = 1, 2.29, 3.34, 13.7 for v = 0, 1, 2, 3.

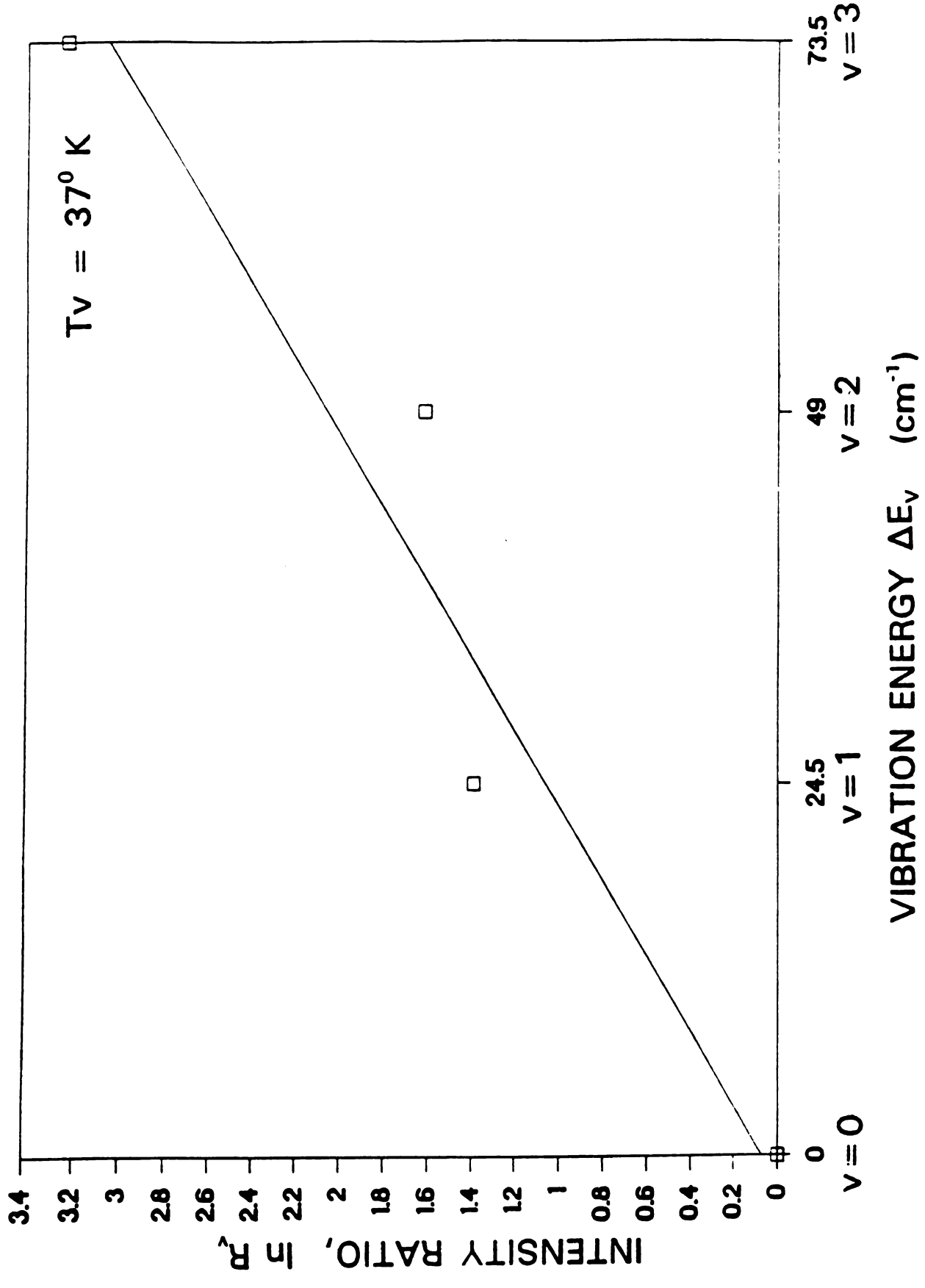
Tv = 37° K
INTENSITY RATIO, ln R_v
3.4
3.2
3
2.8
2.6
2.4
2.2
2
1.8
1.6
1.4
1.2
1
0.8
0.6
0.4
0.2
0
0
v = 0
24.5
v = 1
49
v = 2
73.5
v = 3
VIBRATION ENERGY ΔE_v (cm^-1)

progression, remained constant. It seems that the vibrational temperature will decrease with increasing p_0. Unfortunately, we were not able to eliminate all the hot bands at higher carrier gas pressure p_0. For example, consider the excitation spectrum of perylene at p_0 = 60 psig, shown in Figure 2-16. The signal-to-noise ratio in this spectrum is unacceptable for any meaningful assignments. Two plausible explanations might contribute to the worsened experimental conditions. First, the concentration of perylene will decrease as the carrier gas pressure increases, which can reduce the signal intensity. Second, higher values of p_0 will increase the gas load for the pumping system, and the jet expansion may be strongly perturbed due to backstreaming from the diffusion pump oil once the gas load exceeds the capacity of the pumping system.

Finally, for a comparsion between the performance of pulsed and continuous nozzles, Figure 2-17 shows the perylene excitation spectrum from 416.7 nm to 412 nm, recorded by using a 200 μm continuous nozzle. The sequence bands of the G mode are clearly visible. Moreover, the relative intensity of the G^2_0 band is much lower than in the pulsed-nozzle experiments; this is probably due to the lower S/N ratio. Therefore, we concluded that the pulsed nozzle is superior to the cw nozzle for laser-induced fluorescence experiments with the supersonic instrumentation.

2-6. Aniline experiment

The remainder of this chapter describes a series of experiments on aniline, carried out to investigate the possibility of synthesizing van der Waals complexes with the existing supersonic jet apparatus.

Aniline vapor has an absorption band system near 294 nm which is ascribed to the electronic transition $^1B_2$ <--- $^1A_1$. This system was first observed by Ginsburg and Matsen [96]. Later, Brand et al.[97] and Quack and Stockburger [98] carried out a detailed vibrational analysis. The excitation spectrum of room temperature aniline vapor from 295.1 nm to 290.3 nm is shown in Figure 2-19. The assignment of this spectrum is based on comparsion to the spectra published by Chernoff and Rice [99], and the jet spectra by Mikami et al. [100]; the agreement is good in terms of the band positions and the relative intensities. Some selected frequencies of the vibrational modes pertinent to the assignments are listed in Table 2-3. In the room temperature gas cell spectra, the most prominent features are the electronic origin (00) and several hot bands assigned to sequence bands associated with the inversion mode I and mode T. The symbol T represents both mode 10b and mode 15, and the transition T^1_1 means $10b^1_1$ or 15^1_1. S represents a possible unknown vibrational mode.

Jet-cooled spectra of aniline are shown in Figures 2-20 to 2-23. Figure 2-20 illustrates the spectrum taken at a backing

Figure 2-19 **Fluorescence excitation spectrum of aniline vapor at room temperature from 295.09 nm to 290.30 nm.**

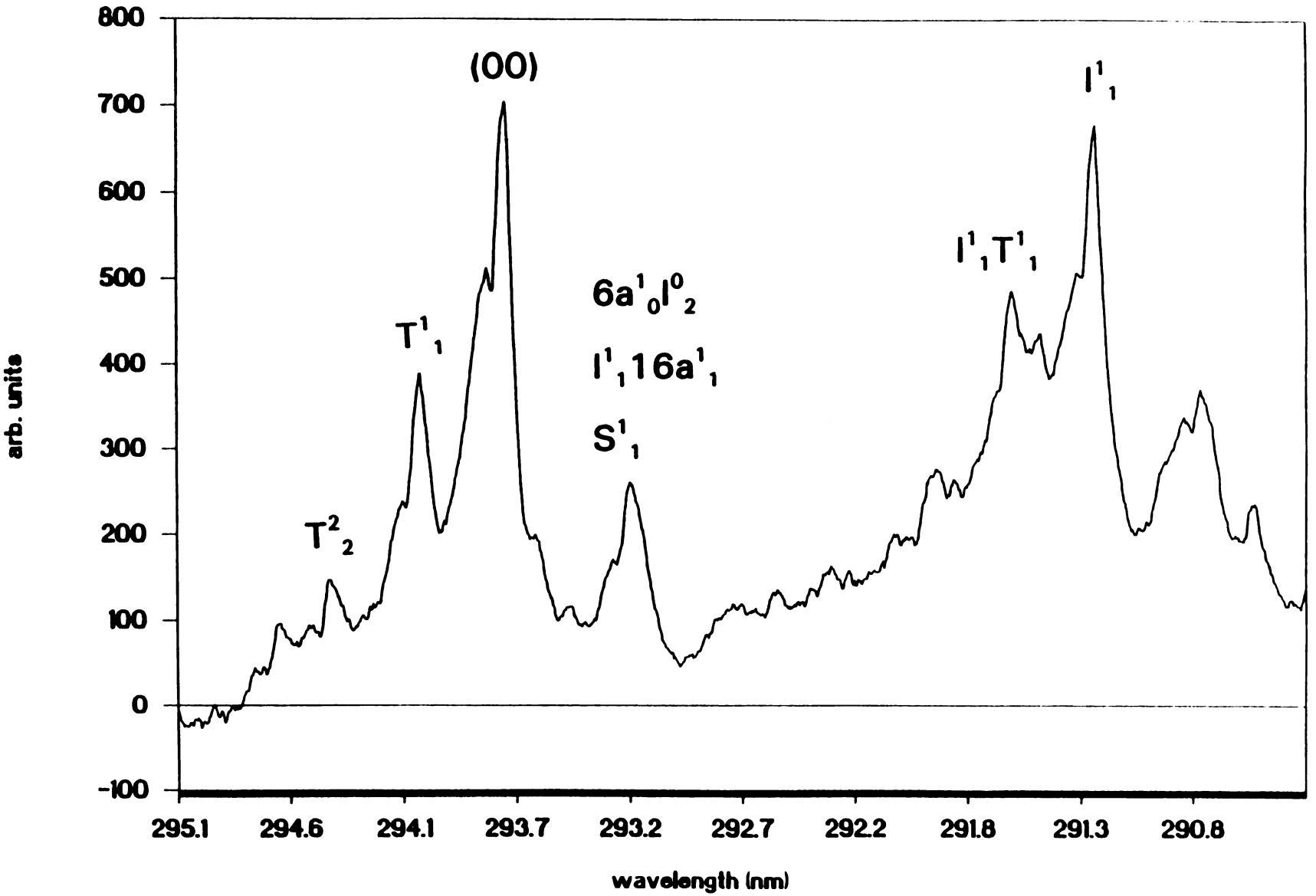
800
700
600
500
400
300
200
100
0
-100
arb. units
(00)
T^1_1
T^2_2
$6a^1_0l^0_2$
$l^1_1 16a^1_1$
S^1_1
$l^1_1T^1_1$
l^1_1
295.1
294.6
294.1
293.7
293.2
292.7
292.2
291.8
291.3
290.8
wavelength (nm)

TABLE 2-3 Frequencies (cm^{-1}) of selected vibrational modes of aniline[a]

mode[b]	$^1A_1$	$^1B_2$
6a	529	492
10b	217	177
15	390	350
16a	419	187
I(v = 1)	40.8	337
I(v = 2)	423	760
I(v = 3)	699	1137

a. D. A. Chernoff and S. A. Rice, J. Chem. Phys. 70, 2511 (1979).

b. The numbering of modes follows G. Varsanyi, ASSIGNMENTS FOR VIBRATIONAL SPECTRA OF SEVEN HUNDRED BENZENE DERIVATIVES (Wiley, New York, 1974)

Figure 2-20 Fluorescence excitation spectrum of aniline from 294.09 nm to 290.50 nm, taken with a 760 μm pulsed nozzle at a carrier gas pressure P_{Ar} = 14 inHg.

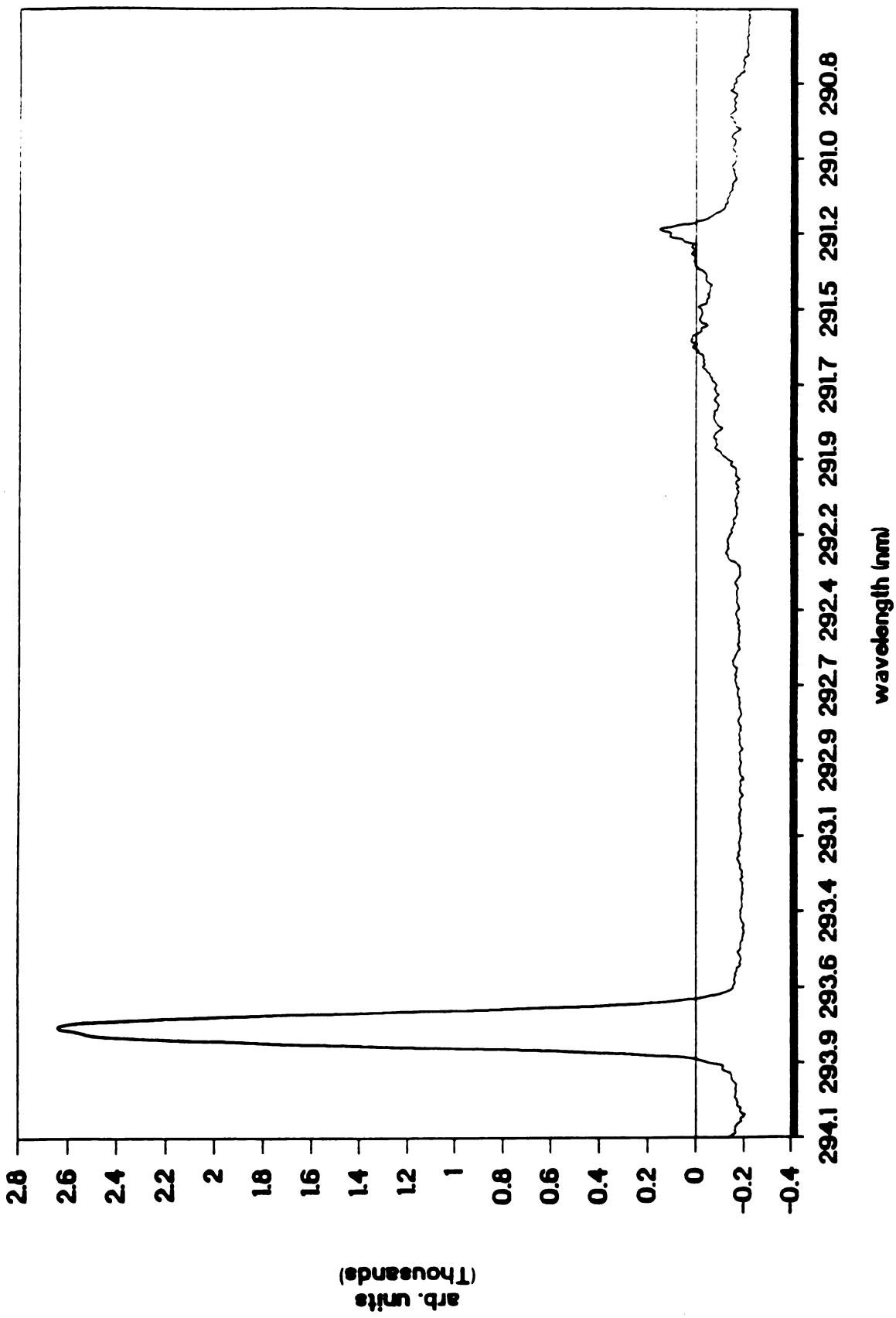
arb. units
(Thousands)
2.8
2.6
2.4
2.2
2
1.8
1.6
1.4
1.2
1
0.8
0.6
0.4
0.2
0
-0.2
-0.4
294.1 293.9 293.6 293.4 293.1 292.9 292.7 292.4 292.2 291.9 291.7 291.5 291.2 291.0 290.8
wavelength (nm)

Figure 2-21 Fluorescence excitation spectrum of aniline from 295.09 nm to 293.3 nm, taken at carrier pressure gas P_{Ar}= 40 psig.

arb. units
(Thousands)
1.1
1
0.9
0.8
0.7
0.6
0.5
0.4
0.3
0.2
0.1
0
-0.1
-0.2
-0.3
295.1
294.6
294.1
293.7
wavelength (nm)

Fig 2-22 Fluorescence excitation spectrum of aniline from 295.09 nm to 293.3 nm, taken with pulsed nozzle at carrier gas presure P_{Ar}=60 psig.

600
500
400
300
200
100
0
-100
-200
-300
arb. units
295.1
294.9
294.6
294.4
294.1
293.9
293.7
293.4
wavelength (nm)

Fig. 2-23 Fluorescence excitation spectrum of aniline from 295.09 nm to 290.3 nm, taken with pulsed nozzle at carrier gas pressure P_{Ar}= 75 psig.

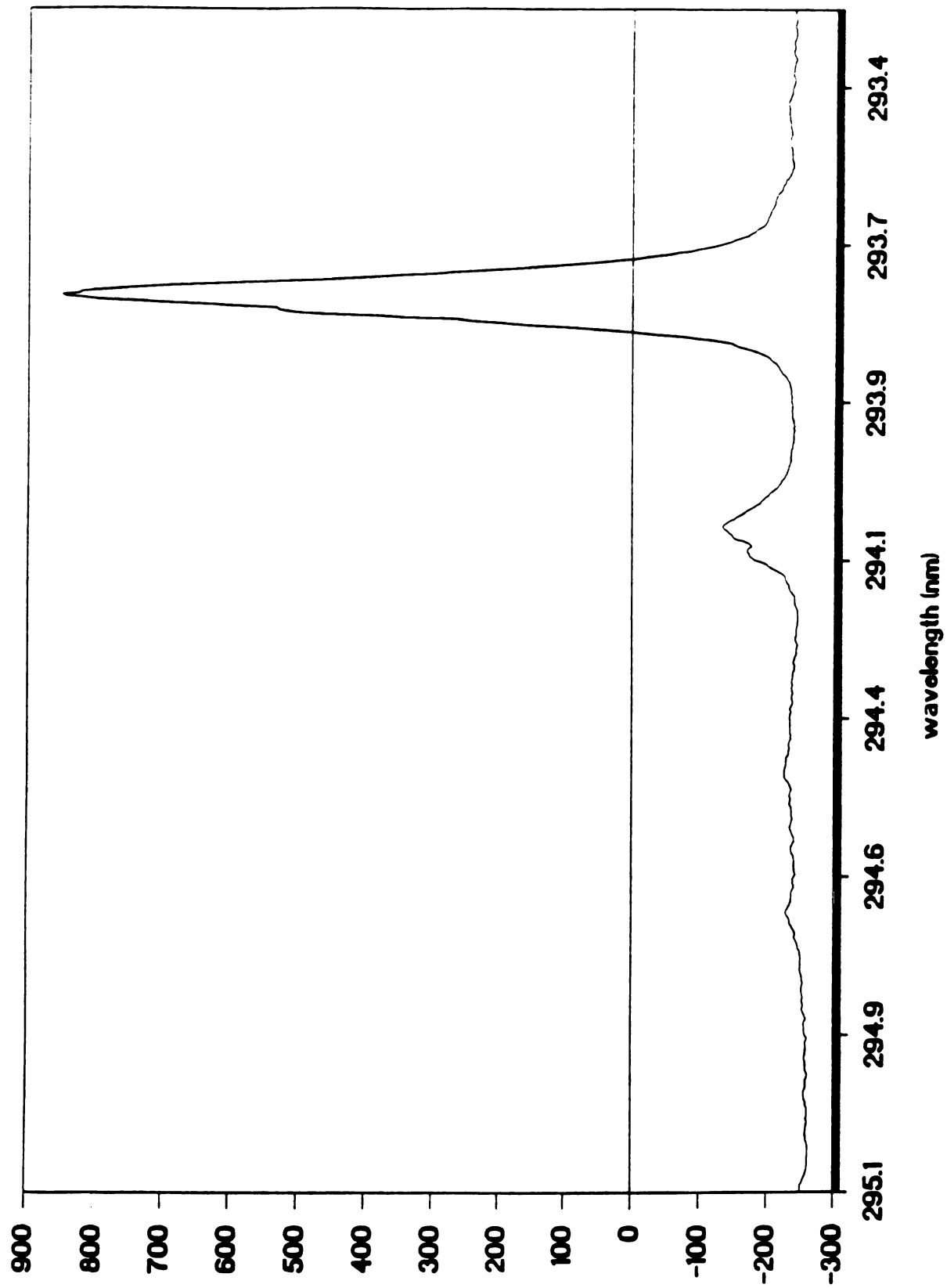
900
800
700
600
500
400
300
200
100
0
-100
-200
-300
arb. units
295.1
294.9
294.6
294.4
294.1
293.9
293.7
293.4
wavelength (nm)

pressure of 360 torr; it is clear that even at this low backing pressure the spectrum is free of hot bands.

The S_1 <--- S_0 transitions of the van der Waals complexes of aniline with rare gases have been reported in the literature [101]. The electronic origins of aniline-Ar_n complexes are red shifted to the low energy side of the electronic origin of bare aniline, as follows:

electronic origin	spectral shift(cm^{-1})	wavelength (nm)
aniline	0	293.8
aniline-Ar	-58	294.3
aniline-Ar_2	-102	294.7

The van der Waals features should appear with increasing backing pressure, or Ar carrier gas pressure. On the other hand, the intensity of fluorescence from the bare molecule should decrease with increasing backing pressure. However, when we increase the argon backing pressure from 30 psig to 75 psig no van der Waals transitions were observed. On the contrary, the only feature that shows increasing intensity is the hot band T^1_1. The results are somewhat suprising since an earlier report [101] indicates that the aniline-Ar complex can be generated under the condition of 7.5 torr cm, and our

expansion conditions are far higher than this value. One possible explanation (similar to the one given for the hot bands in perylene experiments) could be that because our diffusion pump is untrapped, the jet expansion is perturbed by the backstreaming of the diffusion pump oil.

Chapter 3

The fluorescene excitation spectroscopy of [2.2]paracyclophane

3-1 Background

[2.2]paracyclophane was first synsthesized in 1949 by Brown and Farthing [102,103]. This was the first example of a class of molecules in which two benzene rings are fixed in a face-to-face configuration. Cram and coworkers [103,104] later synthesized a series of [m.n]paracyclophanes. These molecules offer the opportunity to study the effect of electronic interaction due to the π-electrons of the rings; furthermore, they exhibit unusual chemical reactivity that reflects the strain of the molecules.

X-ray studies [105,106] indicate that [2.2]paracyclophane has a structure with face-to-face benzene rings, with the planes of the four unsubstituted carbon atoms of each ring being is 3.09 Å apart. This distance is shorter than the normal carbon-carbon van der Waals distance, 3.4 Å. Another interesting aspect of the structure involves the para-carbon

atoms of the molecule. These four carbons are bent about 12^0 out of the plane toward the other benzene ring. This could due to the strong π-π repulsion interaction between the two benzene rings and results in an increase of π-electron density on the outside faces of the benzene rings. Perhaps the most intriguing finding from the x-ray analysis at room and low temperatures is that there is a concerted movement of the two benzene rings toward and away from each other; this is accompanied by a twisting movement of each benzene ring about the long molecular axis.

The ultraviolet spectrum of [2.2]paracyclophane in solution at room temperature, first reported by Cram et al. [103] shows peaks at 310 nm, 290 nm, 260 nm, and 225 nm. The spectrum has been compared to the spectrum of benzene excimers, from the symmetry standpoint [107]. The spectrum of crystalline [2.2]paracyclophane has been studied very thoroughly by Ron and Schnepp [108a,b]. In their investigation, the polarized absorption and fluorescence spectra of a single crystal of [2.2]paracyclophane at 20^0 K were recorded in the region 330-310 nm. The 0-0 transition was observed in absorption at 30361 cm^{-1}, followed by a long progression with 236 cm^{-1} separation. The emission of this transition is extremely weak, but a progression of with separation of 240 cm^{-1} was identified. The assignment of the 0-0 line is unambiguous since the fluorescence spectrum is the mirror image of the absorption spectrum. Thus, this lowest-energy electronic

transition is a pure electronic transition and not vibronically induced.

The molecule [2.2]paracyclophane can be considered as a dimer molecule of para-xylene. As first explained by McClure [109], the electronic spectrum of [2.2]paracyclophane represents a strong coupling case of the transfer of electronic energy between two parts of a double molecule. The simple analysis of the spectrum of a double molecule is as follows: if ψ^0 represents the ground state of the moiety and ψ' the excited state, the electronic wavefunctions of the double molecule can be written as products of the wave functions of the separate parts. The ground state wavefunction of the molecule is $\psi_a^0\psi_b^0$ and the excited states of the double molecule are given by $\psi_a'\psi_b^0 \pm \psi_a^0\psi_b'$. The energy difference between the two excited state components can be estimated as $-(2M^2/R^3)$ under the simple dipole-dipole interaction model, where R is the distance between the centers of the two moieties and M is the transition in one moiety. In fact, the result is a splitting of the vibrationless transition of the double molecule. If M_a is the transition moment of moiety a for the transition ψ_a' <-- ψ_a^0, the transitions for the double molecule are given by $M_a \pm M_b$. In the case of [2.2]paracyclophane, if the two rings are eclipsed, the transition moment of one of the components will be twice M_a and the other component vanishes. McClure [109] calculated a splitting of 632 cm^{-1} for [2.2]paracyclophane by

using this model; however, the observed energy difference for the first two excited states is 2400 cm^{-1}.

Although the anomalous electronic spectum of [2.2]paracyclophane has been interpreted in terms of exciton (the double-molecule model) interaction, many other theoretical procedures [110-114] also have been employed to describe the electronic structure of this molecule. Gleiter [115] was the first to suggest the importance of the mixing between the α-bridges and the π-molecular orbitals. These theoretical analyses centered on the contributions of the splitting of cyclophane π-levels from the overlapping of π-orbitals ("through space" interaction) and the contribution from the mixing with the bridge orbitals of appropriate symmetry ("through-bond" interaction). The through-space and through-bond effects have been carefully examined by Doris et al.[112] In this study, a benzene "sandwich" structure was used as the model to understand the through-space interaction. The result from these calculations showed that the four (e_g) π-orbitals are split into two degenerate sets by the filled orbital closed-shell interation. In the 2.6-3.4 Å range of inter-ring separation of [2.2]paracyclophane, the splitting caused by the π-orbital interactions increases roughly as a linear function of this distance. The effects of through-bond interactions can be understood from the effect of alkyl substutition on the electronic structure of benzene, the distortion of the benzene rings from planarity, and the

involvement of the bridge σ-orbitals. The results indicate that the π-orbitals remain essentially unaffected by changes in σ-character upon alkyl substitution, ring deformation, and bridge-bonding. Therefore, the ordering of the highest occupied π-orbitals is determined mainly by the through-space interaction. The uv absorption spectra of charge-transfer complexes between tetracyanoethylene (TCNE) and paracyclophane have been studied by Cram and Bauer [116]. The peak absorption of the complex is shifted to longer wavelengths compared to the paracyclophane spectrum. The spectral shift was explained in terms of the strength of the paracyclophane acting as a π-base with TCNE being the π-acid. The authors suggested that structure could play a key role in these complexes. The question of whether the carbon-carbon double bond of TCNE lies on the six-fold axis of symmetry of the benzene ring or directly over one of the carbon-carbon bonds of the benzene ring still remained to be answered. Furthermore, the solvent can also influence the charge-transfer complexes by interacting with the TCNE:

$$\text{solvent....[paracyclophane...TCNE]...solvent} \xrightarrow{h\nu} \underset{\text{ground state}}{\text{solvent...[paracyclophane..TCNE]}^{*}\text{...solvent}}$$
excited state

The supersonic jet technique is very well suited to the study

of these systems and can provide information on the molecular level.

Several intramolecular charge-transfer systems involving the [2.2]paracyclophane series have been reported. Some early examples are "quinhydrones" of [2.2]paracyclophane [117,118]. These intramolecular donor/acceptor pairs are fixed in different orientations; although the electron affinity of the acceptor and the ionization energy of the donor are the same, their charge-transfer spectra are very different due to different π-electron overlap and differences in the charge densities on the opposite carbon atoms.

3-2. Experimental section

The pulsed molecular beam apparatus (see discussion in Chapter II) utilized to obtain laser-induced fluorescence spectra of [2.2]paracyclophane is shown in Figure 2-3. Chamber pressures were typically maintained on the order of 10^{-4} torr during an experiment with the pulsed valve in operation. The nozzle, the collection optics, and the laser beam are in a mutually orthogonal geometry. The spectra were excited with doubled radiation from a Spectra-Physics PDL-2 dye laser (1-2 cm^{-1} bandwidth) pumped by a DCR-2A Nd:YAG laser. The output of the dye laser was frequency doubled with an angle-tuned KDP crystal, and the optimum phase matching angle

was maintained by an autotracking system (Spectra-Physics, WEX-1). The laser dye DCM (Exciton) dissolved in methanol was used to scan the spectral region of interest, with energies of 1-2 mJ/pulse. A fast photodiode was used to monitor the laser power. The laser beam was focused with a 100 cm focal length quartz lens before it entered the vacuum chamber, which provided a beam width of 3 mm at the interaction point with the molecular beam. The heated pulsed nozzle is shown in expanded view in Figure 2-3. [2,2]paracyclophane (purchased from Aldrich, and used without further purification) was heated to 170-200^{0}C. Total fluorescence from the jet was collected by an f/1, 5 cm quartz lens, which imaged the fluorescence onto an end-on PMT tube (RCA-8850). A long-pass cutoff filter (Schott GG-335) was used to help reject scattered laser light. The signal from the PMT was sent to one channel (A) of a gated-integrator (Stanford Research Systems SR-250); the output from the photodiode used to monitor the laser power was connected to the second channel (B) of the integrator. The fluorescence intensity from each pulse was normalized to the laser power by the A/B function of the integrator. The spectrum was digitized and stored in a microcomputer for later analysis.

3-3. Fluorescence excitation spectrum of [2.2]paracyclophane

The excitation spectrum of [2,2]paracyclophane from 30675

cm^{-1} to 32570 cm^{-1} is presented in Figure 3-1. Figures 3-2 to 3-4 show the individual scans that constitute Figure 3-1. Figure 3-5 and Figure 3-6 are portions of the spectrum taken at different backing pressures. A complete list of the transition frequencies is given in Table 3-1. Two salient features are observed: first, the intensity becomes very weak towards the low frequency side of the spectrum; also, there are several prominent progressions with similar relative intensities. We account for these distinct features in the following sections.

Our vibronic analysis is guided by two principal criteria: the band separations of the progressions and the Franck-Condon intensities of the individual progression members. On this basis, six progressions can be identified; one of the groups of bands which contains members of each progression is labelled in Figure 3-1. The separations between sucessive members of the five strongest progressions are listed in Table 3-2; the near-identical separation values (~235cm^{-1}) suggest that they are all associated with the same progression-forming mode.

3-4. Fundamentals of electronic transitions [119,120]

Let ψ_e'' and ψ_e' be the electronic eigenfunctions of the lower and upper states involved in an electronic transition, and let

Figure 3-1 Fluorescence excitation spectrum of [2.2]paracyclophane from 30675 cm^{-1} to 32570 cm^{-1}, with Ar carrier gas at a pressure of 230 torr.

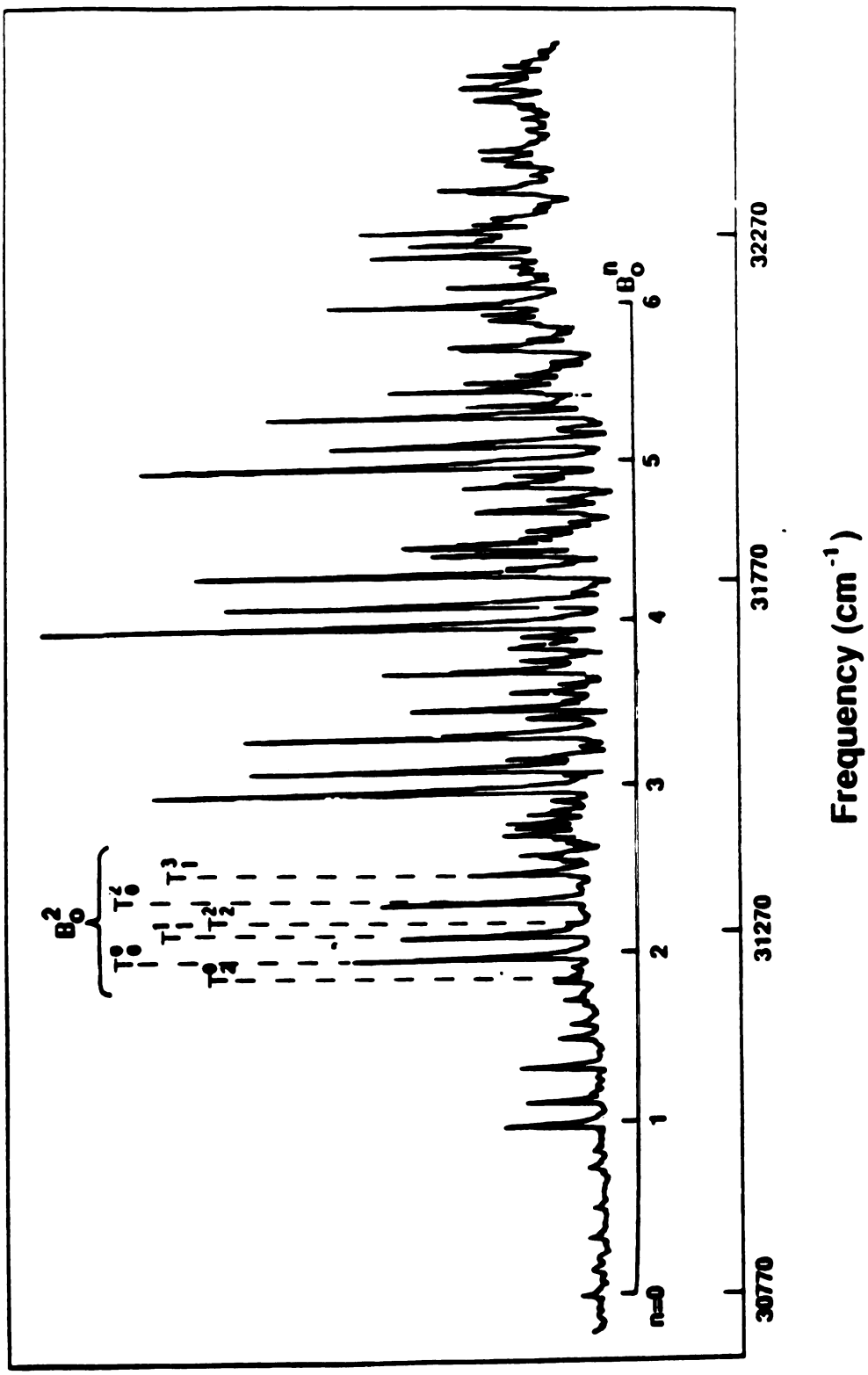
Arbitrary Units
Frequency (cm^{-1})
30770
31270
31770
32270
n=0
1
2
3
4
5
6
B_0^n
B_0^2
T_0^0
T_0^4
T_1^1
T_1^3
T_2^2
T_2^4

Figure 3-2 Fluorescence excitation spectrum of [2.2]paracyclophane from 325.5 nm to 319 nm, taken at Ar carrier gas pressure of 230 torr.

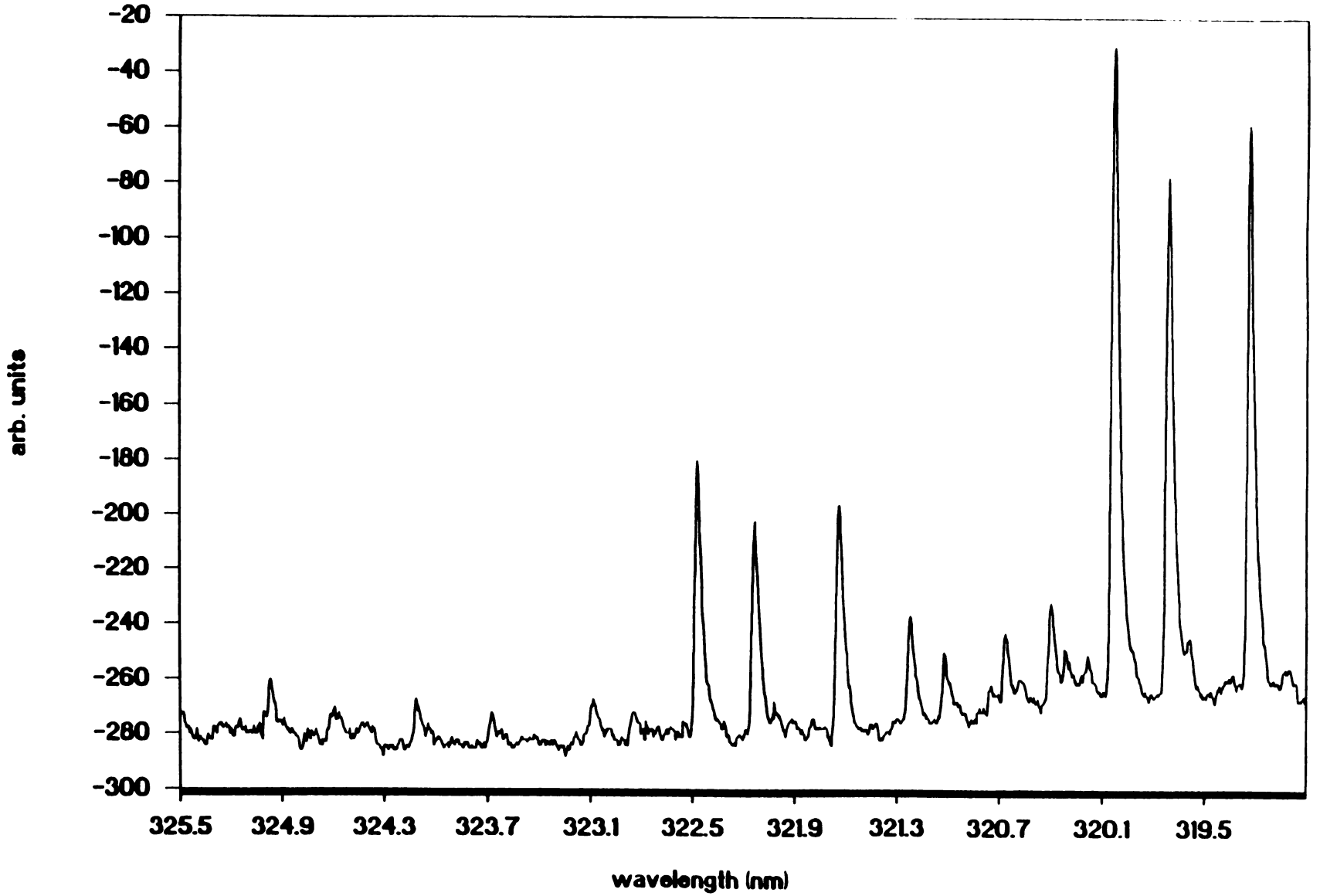
-20
-40
-60
-80
-100
-120
-140
-160
-180
-200
-220
-240
-260
-280
-300
arb. units
325.5
324.9
324.3
323.7
323.1
322.5
321.9
321.3
320.7
320.1
319.5
wavelength (nm)

Figure 3-3 Fluorescence excitation of [2.2]paracyclophane from 319 nm to 313 nm, taken under the same conditions as the previous figures.

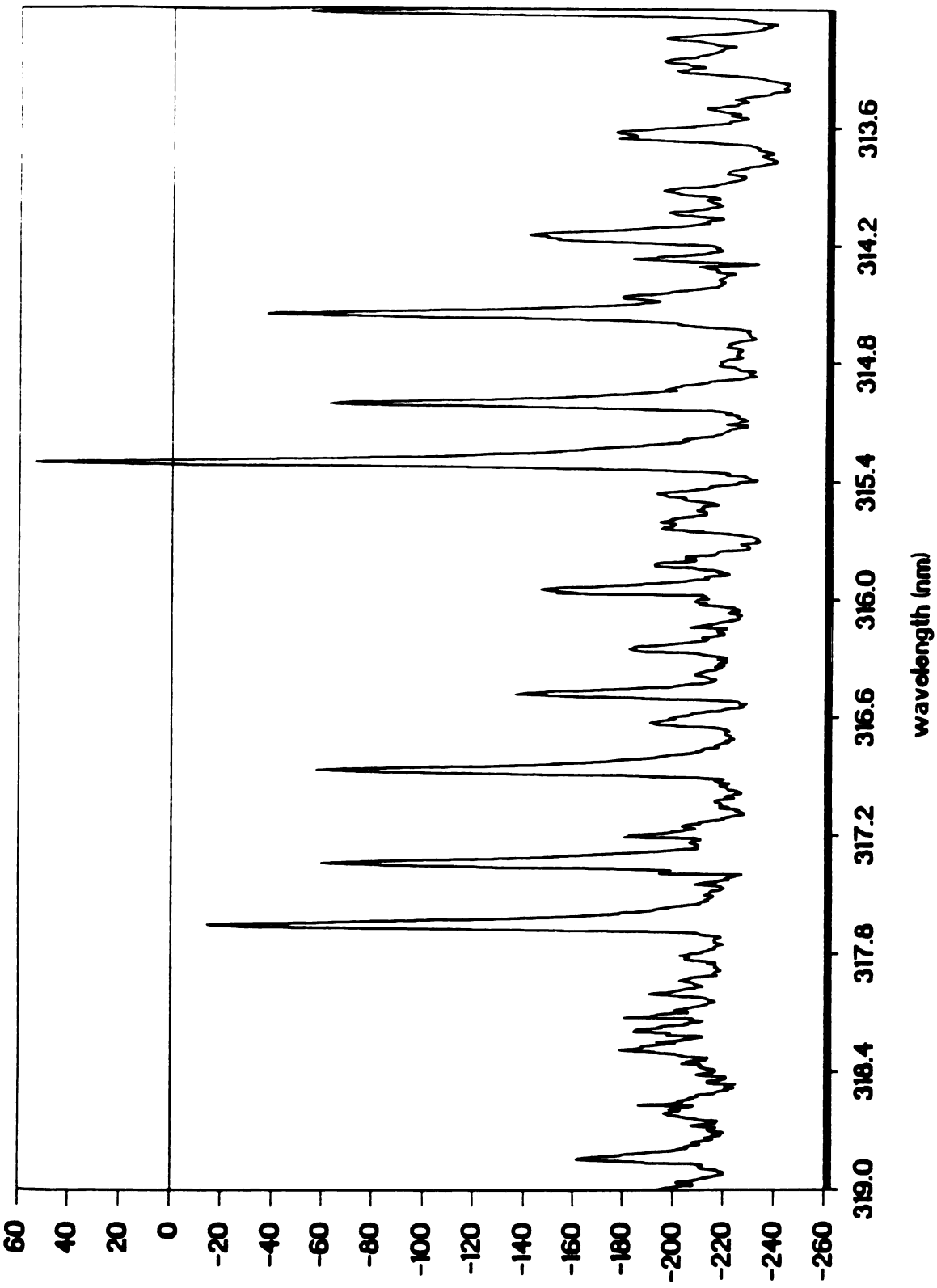
arb. units
60
40
20
0
-20
-40
-60
-80
-100
-120
-140
-160
-180
-200
-220
-240
-260
319.0
318.4
317.8
317.2
316.6
316.0
315.4
314.8
314.2
313.6
wavelength (nm)

Figure 3-4 Fluorescence excitation spectrum of [2.2]paracyclophane from 316 nm to 310 nm; unchanged experimental conditions.

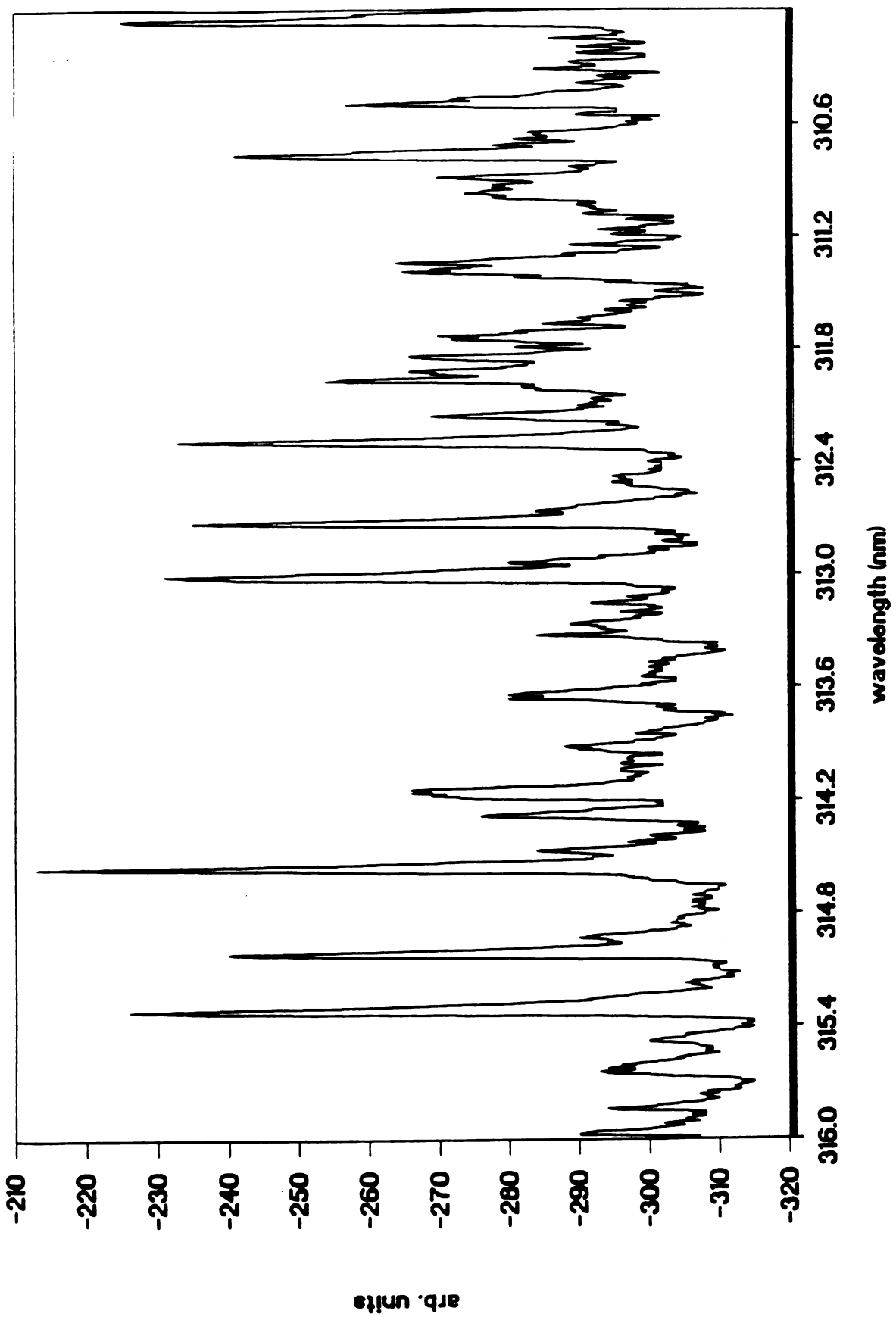
arb. units
-210
-220
-230
-240
-250
-260
-270
-280
-290
-300
-310
-320
316.0
315.4
314.8
314.2
313.6
313.0
312.4
311.8
311.2
310.6
wavelength (nm)

Figure 3-5 Fluorescence excitation spectrum of [2.2]paracyclophane from 325.5 nm to 319 nm at P_{Ar} = 200 torr. It can be seen that the relative intensity of B^n_0 and $B^n_0T^1_1$ progressions has changed from the spectrum taken at P_{Ar}= 230 torr (Figure 3-1).

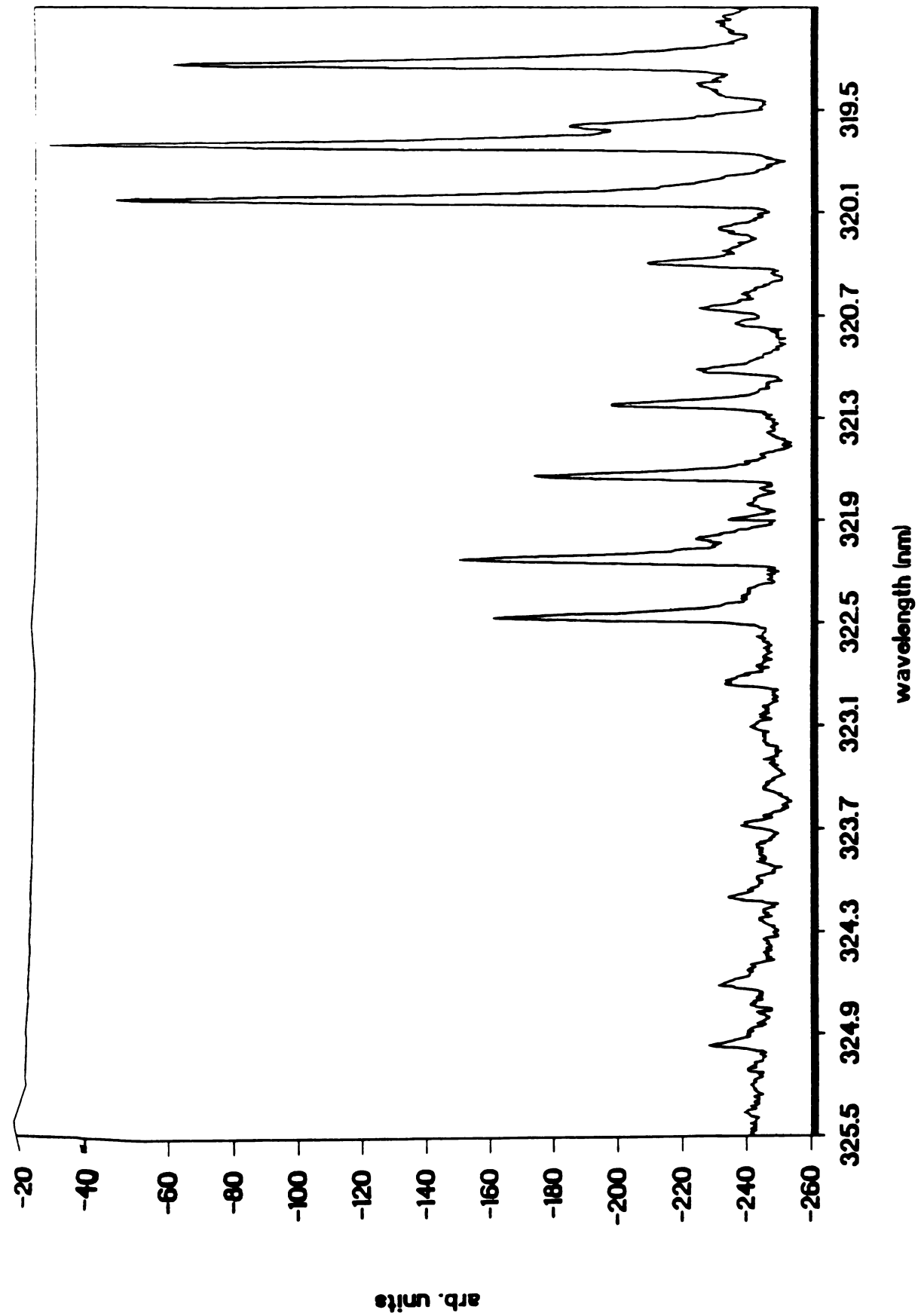
arb. units
-20
-40
-60
-80
-100
-120
-140
-160
-180
-200
-220
-240
-260
325.5
324.9
324.3
323.7
323.1
322.5
321.9
321.3
320.7
320.1
319.5
wavelength (nm)

Figure 3-6 Fluorescence excitation spectrum of [2.2]paracyclophane from 320 nm to 314 nm at P_{Ar} = 680 torr. At this pressure condition the signal-to-noise ratio is poor; however, the intense hot band progressions were eliminated.

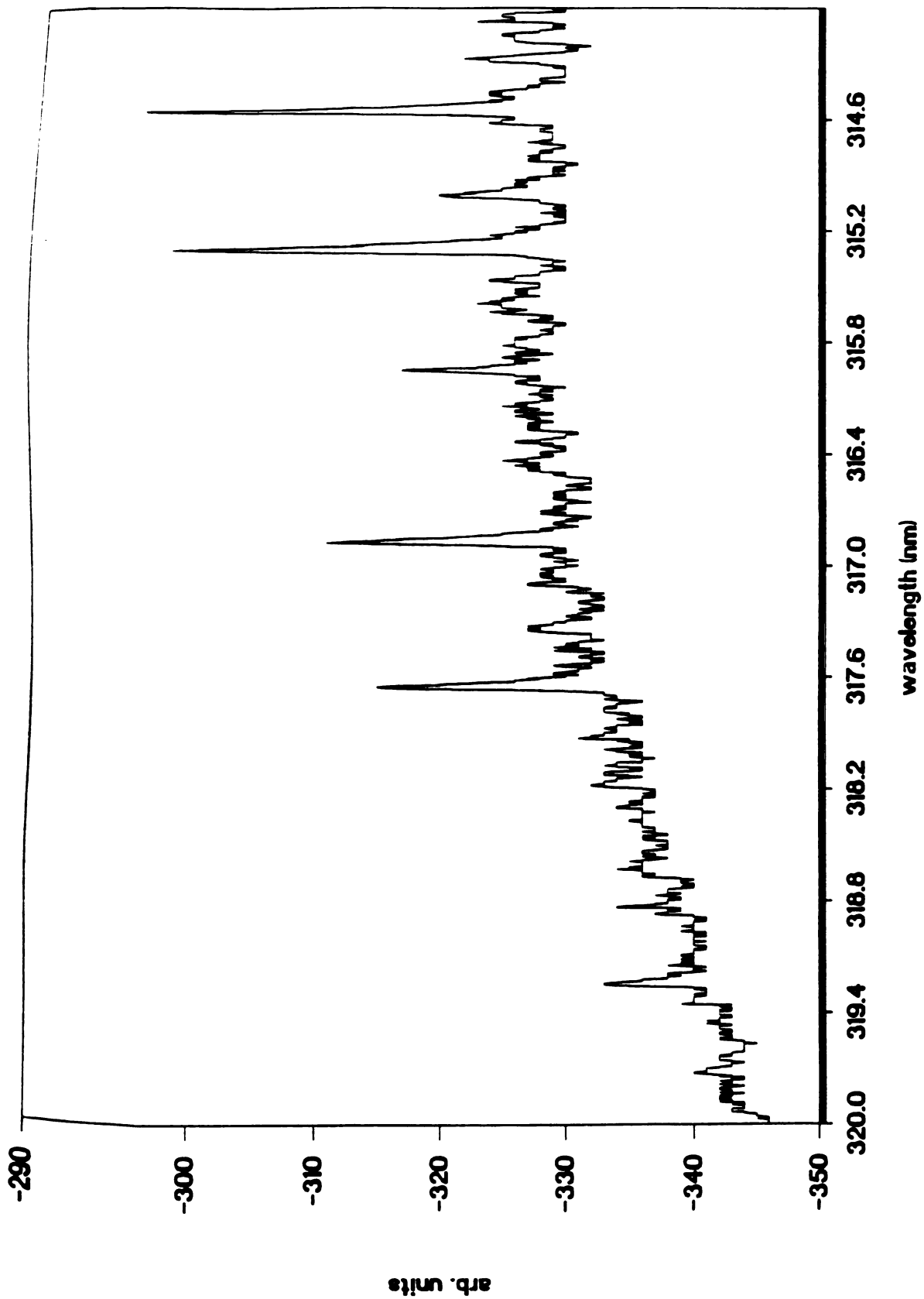
-290
-300
-310
-320
-330
-340
-350
arb. units
320.0
319.4
318.8
318.2
317.6
317.0
316.4
315.8
315.2
314.6
wavelength (nm)

TABLE 3-1 Observed transition energies(cm^{-1}) in the fluorescence excitation spectrum of [2.2]paracyclophane

Wavenumber	Relative to origin	Assignment
30772	0.0	origin
30809	37	$B^0_0T^1_1$
30825	53	
30853	81	$B^0_0T^2_0$
30894	122	$B^0_0T^3_1$
30951	179	
30974	202	$B^1_0T^0_2$
31009	237	B^1_0
31041	269	$B^1_0T^1_1$
31055	283	$B^1_0T^2_2$
31089	317	$B^1_0T^2_0$
31129	357	$B^1_0T^3_1$
31148	376	
31184	412	
31210	438	$B^2_0T^0_2$
31217	445	
31230	458	
31244	472	B^2_0
31276	504	$B^2_0T^1_1$
31289	517	$B^2_0T^2_2$
31323	551	$B^2_0T^2_0$
31363	591	$B^2_0T^3_1$

31384	612	
31416	644	
31428	656	
31430	658	
31445	673	$B^3_0T^0_2$
31450	678	
31463	691	
31479	707	B^3_0
31510	738	$B^3_0T^1_1$
31521	749	$B^3_0T^2_2$
31556	784	$B^3_0T^2_0$
31581	809	
31583	811	
31595	823	$B^3_0T^3_1$
31619	847	
31622	850	
31649	877	
31662	890	
31680	908	$B^4_0T^0_2$
31698	926	
31713	941	B^4_0
31743	971	$B^4_0T^1_1$
31753	981	$B^4_0T^2_2$
31789	1017	$B^4_0T^2_0$
31818	1046	
31831	1059	$B^4_0T^3_1$

31842	1070	
31854	1082	
31880	1108	
31883	1111	
31915	1143	$B^5_0T^0_2$
31920	1148	
31932	1160	
31945	1173	
31946	1174	B^5_0
31977	1205	$B^5_0T^1_1$
31985	1213	$B^5_0T^2_2$
32021	1249	$B^5_0T^2_0$
32035	1263	
32055	1283	
32067	1295	$B^5_0T^3_1$
32078	1306	
32115	1343	
32119	1347	
32150	1378	$B^6_0T^0_2$
32158	1386	
32167	1395	
32179	1407	B^6_0
32208	1436	$B^6_0T^1_1$
32252	1480	$B^6_0T^2_0$
32270	1498	
32289	1517	

32300	1528	$B^6_0T^3_1$
32310	1538	
32350	1578	
32397	1625	
32408	1636	
32435	1663	
32454	1682	
32472	1700	
32484	1712	
32503	1731	
32521	1749	
32534	1762	
32541	1769	

TABLE 3-2 Separation of progression members

Progression origin	B^0-B^1	B^1-B^2	B^2-B^3	B^3-B^4	B^4-B^5	B^5-B^6
00	237	235	235	234	233	233
T^1_1	232	235	234	233	234	231
T^2_0	236	234	233	233	232	231
T^3_1	235	234	236	236	236	233
T^0_2	-	235	236	235	235	235

both states be non-degenerate. The transition can be predicted by the matrix element

$$R_{e'e''} = \int \psi_e'^{*} \, M \, \psi_e'' \, d\tau \qquad \text{(III-1)}$$

The transition is allowed if $R_{e'e''} \neq 0$, and forbidden if $R_{e'e''} = 0$. Here M is the dipole moment vector, with components $\Sigma e_i x_i$, $\Sigma e_i y_i$ and $\Sigma e_i z_i$. (If the electric dipole moment is replaced by the magnetic dipole moment or the electric quadrupole moment then the transition probability produced by magnetic dipole or electric quadrupole radiation can be obtained.) That is, the electronic transition is allowed if the product

$$\psi_e'^{*} \, M \, \psi_e'' \qquad \text{(III-2)}$$

is totally symmetric for at least one of the orientations of M, or in other words, if the product $\psi_e'\psi_e''$ belongs to the same species as one of the components of M. The totally symmetric product can be obtained if the direct product of the species Γ of ψ_e', ψ_e'' and M has a totally symmetric component

$$\Gamma(\psi_e') \times \Gamma(\psi_e'') \times \Gamma(M) = \text{totally symmetric.} \qquad \text{(III-3)}$$

Thus, if $\Gamma(\psi_e') \times \Gamma(\psi_e'')$ has the same species as one of the components of M, equation (III-3) will be satisfied.

So far we have considered the case that the nuclei are

fixed. However, in reality we must recognize that the nuclei are not fixed and the total eigenfunction should include nuclear coordinates (if we neglect the interaction of electronic and vibrational motions)

$$\psi_{ev} = \psi_e(q,Q)\ \psi_v(Q)$$

q: electronic coordinates

Q: nuclear coordinates

The electric dipole moment can be separated into two parts

$$M = M_e + M_n$$

Equation (III-1) now became

$$R_{e'v'e''v''} = \int \psi_{ev}'^{*}\ M\ \psi_{ev}''\ d\tau_{ev}$$
$$= \int \psi_v'^{*}\psi_v''d\tau_v \int \psi_e'^{*}M_e\psi_e''d\tau_e + \int \psi_v'^{*}M_n\psi_v''d\tau_v \int \psi_e'^{*}\psi_e''d\tau_e \qquad \text{(III-4)}$$

Since electronic eigenfunctions are orthogonal, we have

$$\int \psi_e'^{*}\ \psi_e''\ d\tau_e = 0.$$

Therefore

$$R_{e'v'e''v''} = R_{v'v''}R_{e'e''}$$
$$= \int \psi_v'^{*}\psi_v''d\tau_v \int \psi_e'^{*}\ M_e\ \psi_e''d\tau_e \qquad \text{(III-5)}$$

The second integral in (III-5) is the matrix element of the

electric dipole moment for a given nuclear configuration (Q); it can be written as

$$R_{e'e''}(Q) = \int \psi_e'^{*}(q,Q)\ M_e\ \psi_e''(q,Q)\ d\tau_e \qquad \text{(III-6)}$$

If we neglect the dependence of electronic eigenfunctions on nuclear coordinates, Q corresponds approximately to the configuration of the nuclei near the equilibrium position. Accordingly, (III-5) becomes

$$R_{e'v'e''v''} = R_{e'e''}(Q) \int \psi_v'^{*}\psi_v'' d\tau_v$$
$$= R_{e'e''}\ R_{v'v''} \qquad \text{(III-7)}$$

The above discussion is based on symmetry considerations. If a molecule has no symmetry, then all electronic states can combine with one another. On the other hand, if the molecule belongs to a particular point group, then the allowed electronic transitions can be predicted with the help of symmetry properties. Table 3-3 contains the direct products and the transition moments related to electronic transitions for the D_2, (D_{2h}) point group(s) [119] which are pertinent to the discussion of the symmetry of [2.2]paracyclophane.

Up to now we have assumed that the molecule has the same symmetry in both the lower and upper electronic states associated with an electronic transition. The transition will be allowed as long as the product $\psi_e'^{*}M\psi_e''$ is totally symmetric. However, in many cases the equilibrium

TABLE 3-3 (a) Direct products for D_2, $(D_{2h})^*$

	A	B_1	B_2	B_3
A	A	B_1	B_2	B_3
B_1		A	B_3	B_2
B_2			A	B_1
B_3				A

(b) Transition moments of electronic transitions belonging to D_2, (D_{2h}).

D_2, D_{2h}^*	A	B_1	B_2	B_3
A	-	M_z	M_y	M_x
B_1		-	M_x	M_y
B_2			-	M_z
B_3				-

* For D_{2h}, the (g,u) rule must be added; that is: $g \times g = g$, $g \times u = u$, $u \times u = g$.

configuration of the molecule has different symmetry in the two states involved in a transition. (In other words, the two states belong to different symmetry point groups.) The symmetry elements to be considered in these cases are the ones that are common to both states. For example, a molecule XY_3 can be planar and symmetrical (D_{3h}) in one state, and non-planar (C_{3v}) in another state. The transition dipole moment matrix element $\psi_e'^* M \psi_e''$ will be determined with respect to point group C_{3v}, but not D_{3h}.

It is clear that in deriving (III-7), we have assumed the independence of electronic and vibrational motions. However, the general selection rule requires only that

$$\int \psi_{ev}'^* \, M \, \psi_{ev}'' \, d\tau_{ev} \neq 0. \qquad \text{(III-8)}$$

Thus electronic transitions that are forbidden by the symmetry of the electronic eigenfunction might be allowed from consideration of the vibronic species, $\psi_e\psi_v$, if the product of the vibronic species of the two states involved ($\psi_{e'v'}\psi_{e''v''}$) contains the species of one of the components of the electric dipole moment.

There are many examples which demonstrate that a transition can be electronically forbidden (equation III-7 does not hold) but made allowed by the vibronic interactions. Therefore, for $R_{e'v'e''v''}$ to be different from zero, the vibronic species must be different from the electronic species, and the vibronic

transition in such a forbidden electronic transition is different from those in allowed electronic transitions. This phenomenon is called Herzberg-Teller intensity borrowing [121]. It was first explained by noting that when the vibrational integral of equation (III-7) is non-totally symmetric, the electronic transition moment $R_{e'e''}$ is no longer independent of vibrational motion. The effect of vibrational motion is taken into account of by expanding M as a Taylor series in normal coordinates Q_k, Q_l, ... of the vibrations involved in the borrowing:

$$\begin{aligned} M = {} & (M)_{eq} && \text{zero order} \\ & + \Sigma \, (\partial M/\partial Q_k)_{eq} \; Q_k && \text{first order} \\ & + 1/2! \; \Sigma \, \Sigma \, (\partial^2 M/\partial Q_k \partial Q_l)_{eq} \; Q_k Q_l && \text{second order} \end{aligned}$$

If we consider only the first two terms, then

$$R_{e'v'e''v''} = \int \psi_{e'v'} \, [(M)_{eq} + \Sigma \, (\partial M/\partial Q_k)_{eq} \; Q_k] \, \psi_{e''v''} \, d\tau_v$$

It is convenient to separate the vibrations into totally symmetric (s) and non-totally symmetric (a); then we have

$$\begin{aligned} R_{e'v'e''v''} = \int \psi_{e'v'} \, [& (M)_{eq} + \Sigma \, (\partial M/\partial Q_s) Q_s \\ & + \Sigma \, (\partial M/\partial Q_a) Q_a] \psi_{e''v''} \, d\tau \end{aligned} \qquad \text{(III-9)}$$

For an electronically forbidden transition, the first two terms on the right hand side would be zero, and only the third term is non-zero. In this case, the transition is said to be electronically forbidden but vibronically allowed. The classical example of Herzberg-Teller intensity borrowing is the $B_{2u}(A)$ <--- A_{1g} 266 nm band system of benzene. This electronic transition is forbidden by symmetry; however, the transition is made allowed by the vibronic coupling of the B_{2u} state to a higher E_{1u} state through the ν_6 (e_{2g}) mode ($B_{2u} \times e_{2g} = E_{1u}$, $E_{1u} = \Gamma(T_x, T_y)$.)

- Vibrational structure of electronic transitions

In an allowed electronic transition, $R_{e'e''}$ must be different from zero. Futhermore, $R_{v'v''}$ also must not equal zero. For a symmetrical molecule, the latter integral will be different from zero only if the integrand ($\psi_v'^* \psi_v''$) is symmetric with respect to all symmetry operations permitted by the point group to which the molecule belongs. That is: $\psi_v'^* \psi_v''$ must be totally symmetrical, which is equivalent to condition that only vibrational levels of the same vibrational species in the upper and lower states can combine with one another. This is the general selection rule for allowed electronic transitions.

For allowed transitions between two non-degenerate electronic states, all vibrational levels of a totally

symmetric vibration are totally symmetric (i.e. symmetric with respect to all symmetry operations that apply to the equilibrium positions of both electronic states). Therefore, in allowed electronic transitions all totally symmetric vibrations may change by any number of quanta: $\Delta v = 0, \pm 1, \pm 2, \ldots$. For the higher states of an antisymmetric vibration v_k (a vibration that is antisymmetric with respect to at least one of the symmetry elements), the even levels of v_k are symmetric and the odd levels of v_k are antisymmetric. Thus, according to the selection rule, v_k can only change by an even number of quanta: $\Delta v = 0, \pm 2, \pm 4, \ldots$. The $\Delta v = 0$ sequence bands are always the most intense transitions unless they are weakened by the Boltzmann factor.

As mentioned earlier, the selection rule for transitions between electronic states with different symmetry is the one that applies to the common elements of symmetry. We can now consider the effect of the difference in symmetry on the vibronic structure. If we consider the earlier example of an non-planar XY_3 molecule, e.g. NH_3, the molecule might change its geometry from C_{3v} (non-planar) to D_{3h} (planar) in an excited electronic state; the C_{3v} selection rule should apply to this transition since the lower point group is C_{3v}. However, the vibrational levels of NH_3 are split into two sublevels: symmetric (+), and antisymmetric (-), due to inversion ("inversion doubling"). Symmetric and antisymmetric are defined with respect to the symmetry plane; in other

words, the effective point group for a non-planar molecule with inversion doubling is D_{3h}, since this is the symmetry of the potential field. The D_{3h} vibronic selection rules should be followed, which means that only transitions between vibrational wavefunctions which have the same symmetry (+ <--> +, - <---> -) are allowed, so that the $\psi_{v'}^{*}\psi_{v''}$ totally symmetric requirement is satisfied.

- Intensity distributions in electronic transitions- The Franck-Condon principle [122,123]

The Franck-Condon principle is a simple qualitative concept that states that because an electronic transition in a molecule takes place on a time scale much shorter than vibrational motion, the nuclei maintain the same position and velocity after the transition. This principle is very helpful in interpreting the vibronic structure.

The intensity of a vibronic transition is proportional to the square of the transition moment $R_{e'v'e''v''}$, which is given by equation III-7; $R_{e'e''}$ is given by III-6, and $R_{v'v''}$ is the vibrational overlap integral. $R_{v'v''}$ is a measure of the overlap of the two vibrational wavefunctions involved in the vibronic transition. The square of this integral is called the Franck-Condon factor, and it can be used to predict the intensity distribution in vibronic transition. Figure 3-7 illustrates three typical cases of vibronic intensity distribution. In case (a) $r_e'' \approx r_e'$, where r_e'' and r_e' are the

Figure 3-7 Typical vibrational progression intensity distributions. Case (a) $r_e' \approx r_e''$, case (b) $r_e' > r_e''$, and case (c) $r_e' >> r_e''$


v'
0
1
2
ν̃
(a)
v'
0
1
2
3
4
5
6
7
8
9
10
ν̃
(b)
ν̃
(c)

Figure 3-8 Quantum mechanical representation for the intensity distribution of case (b) $r_e' > r_e''$

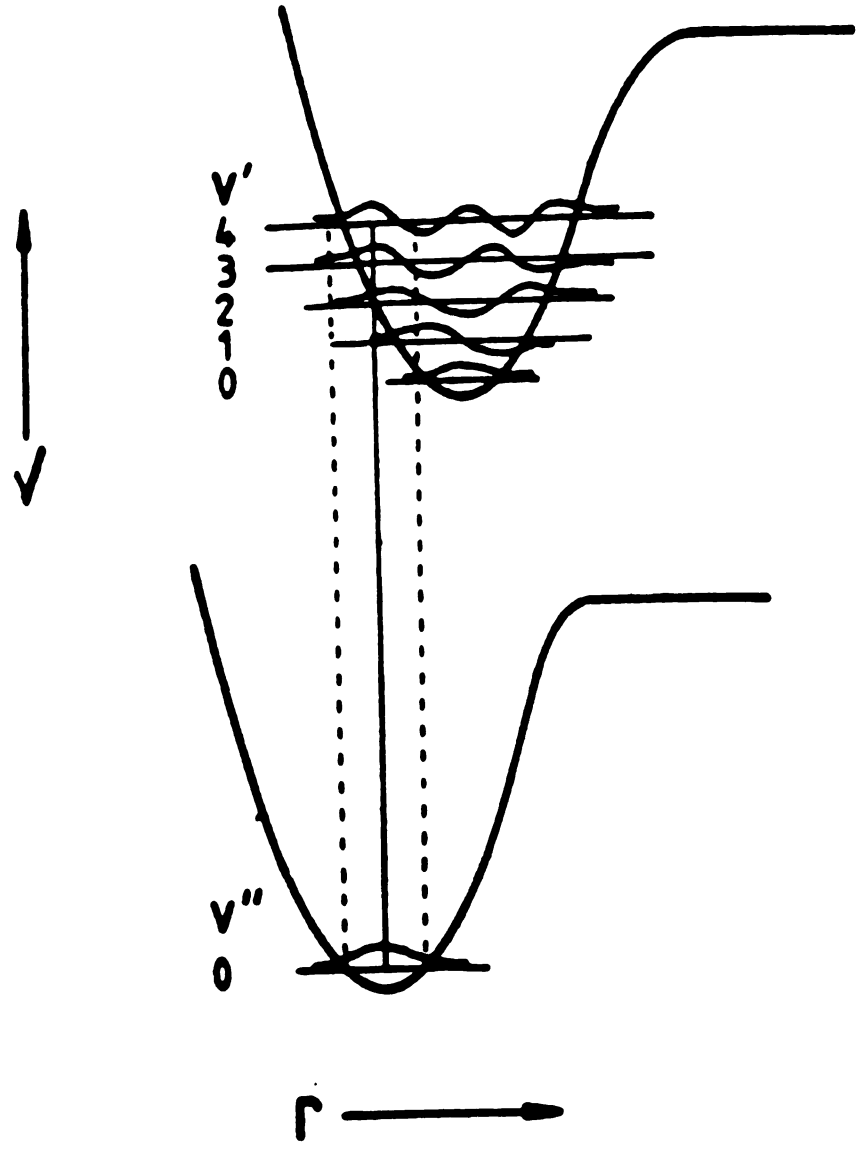

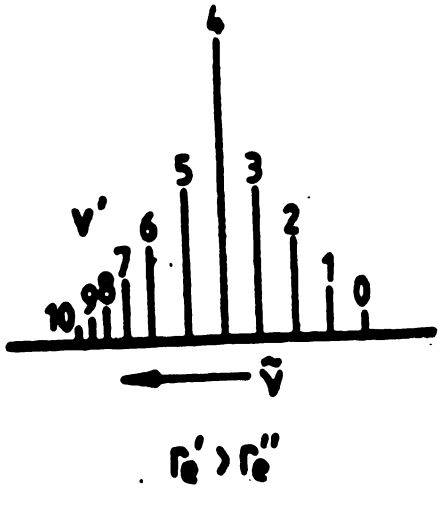

(b)

internuclear distances in the lower and upper electronic states; v′ = 0 (the electronic origin) has the maxmum intensity, and the intensity falls off fairly rapidly. An example is the electronic transition to the first excited state of perylene. In case (b), where $r_e' > r_e''$, the excited state potential curve above v″ = 0 is steep; this gives a broad maximum in the progression intensity. Note that $r_e' < r_e''$ might have the same Franck-Condon factor, and thus a similar intensity pattern. However, in the $r_e' < r_e''$ case, the shallow part of the excited state potential is above v″ = 0, which would give a sharper intensity maximum. Figure 3-8 is an illustration of the Franck-Condon principle with schematic wavefunctions associated with the vibrational levels. In case (c), Figure 3-7, $r_e' >> r_e''$, the intensity distribution may involve a broad intensity maximum close to the continuum onset.

For diatomic molecules, the Franck-Condon principle predicts that the greater the change in the internuclear distance, the longer will be the vibronic band system progression. Tables are available which relate progression intensity to the vibrational frequencies and the change of normal coordinates, which allow the determination of the change in geometry of a molecule upon electronic excitation.

The application of the Franck-Condon principle to polyatomic molecules is straightforward. If one measures the intensities along 3N-6 progressions, one could determine the change of the

3N-6 normal coordinates. However, for the spectra of most large molecules, often only a few progressions can be observed and identified. If we assume the change along all normal coordinates except the one with the most prominent progression are negligible, we may obtain useful information about the geometry change accompanying electronic excitation in a large molecule. Many examples can be found in the spectroscopic literature [119].

3-5 Spectroscopic analysis of [2.2]paracyclophane

From the discussion in Section 3-4, we can summarize the general selection rules for allowed electronic transitions between two nondegenerate electronic states of the same symmetry as follows [119,120]: (1) $\Delta v=0, \pm1, \pm2, \ldots$ for totally symmetric vibrational modes, and (2) $\Delta v=0, \pm2, \pm4, \ldots$ for the nontotally symmetric modes. Furthermore, for the latter, the $\Delta v=0$ sequence bands should have prominent intensity unless they are weakened by the Boltzmann factors. For a double minimum vibrational potential, which might apply to the twisting mode in [2,2]paracyclophane, the vibrational eigenfunctions may labelled with "+" and "-", the even symmetry levels corresponding with + parity and the odd levels with - parity. The additional selection rules for allowed vibronic transitions are: +<-->+ and -<-->-.

The lowest energy transition is observed at 30772 cm^{-1}, with

very weak intensity (see Figure 3-1). We tentatively assign this band as the electronic origin. A long progression with the strongest intensity in each group of bands starts at 30772 cm^{-1}, with ~235 cm^{-1} separation between successive members. This progression is the most dominant feature both in the absorption and the emission spectra [108,124,125], and the observed gas-to-crystal shift for the band separations is small [108]. It is well established that a relatively large geometry change accompanying an electronic transition will produce long progressions [122,123]. Moreover, the change in geometry of a molecule in the excited state can be inferred by examining the Franck-Condon intensity envelope. Canuto and Zerner [113] have predicted theoretically that the inter-ring spacing of [2,2]paracyclophane will decrease by ~0.31Å in the first excited state; this result is supported by the calculations carried out in this investigation. The structural change is consistent with the long progression we observe in the excitation spectrum, which we assign as the breathing mode progression, B^n_0, in the upper state.

A second progression starts at (0,0)+ 81 cm^{-1} and also extends over the entire excitation spectrum. The separations between successive progression members and their Franck-Condon intensity distribution are essentially identical to the B^n_0 progression, which indicates that both are associated with the same progression-forming mode. We assign this progression, on average spaced 78 cm^{-1} from B^n_0, to $B^n_0T^2_0$, the breathing mode

combined with two quanta of the inter-ring twisting vibration in the excited state.

An important objective of supersonic jet spectroscopy is the internal cooling of the entrained molecule. However, hot bands in the electronic spectrum can serve as an aid in spectroscopic assignment [126]. This is particularly true for low frequency modes. The [2.2]paracyclophane fluorescence excitation spectrum shown in Figure 3-1 contains several long progressions from hot bands, for which the intensities are controlled by Boltzmann factors. The hot band origin can be easily verified by changing the carrier gas pressure (as shown in Figure 3-5), which alters the effective internal temperature of the analyte molecule. (We were unable to eliminate all hot bands by increasing the carrier gas pressure because of deterioration of the signal-to-noise ratio under our experimental conditions; see Figure 3-6.) The lowest energy band stemming from $v_T''=1$ lies at (0,0)+ ~37 cm^{-1}; it is the first member of a progression assigned to the breathing mode in combination with the $\Delta v=0$ transition of the twisting mode, $B^n_0T^1_1$. A second hot band progression from $v_T''=1$ starts at (0,0)+ 122 cm^{-1}; it is assigned to the progression-forming mode in combination with the $\Delta v=2$ transition of the twisting mode, $B^n_0T^3_1$. The Franck-Condon intensity envelopes of both $B^n_0T^1_1$ and $B^n_0T^3_1$ progressions are very similar to that of the B^n_0 progression. According to this assignment, and considering all the members of these progressions identified in Table 1,

the $v_T'=1$ and $v_T'=3$ levels are separated by 88 cm^{-1} in the excited electronic state.

The intensities of the remaining two progressions are significantly lower than the first four. We assign them to combinations involving hot bands originating from the second vibrational level of the twisting mode in the ground state, $v_T''=2$, their intensities being severely weakened by the Boltzmann factor. The first member of the progression, $B^n_0T^0_2$, should lie below the electronic origin; unfortunately, because of the low Franck-Condon intensity of B^0_0 this band cannot be discerned in our spectra. We assign the band at (0,0)+ 202 cm^{-1} (B^1_0 - 35 cm^{-1}) as the second member of this progression. The average separation, B^n_0-$B^n_0T^0_2$, is 34 cm^{-1}. The remaining progression in the excitation spectrum is clearly observable only at significantly decreased carrier gas pressure, where the paracyclophane internal temperature is higher. Figure 3-9 illustrates the appearance of these hot bands on the higher frequency side of the $B^n_0T^1_1$ progression members under lower pressure conditions than those used to obtain Figure 3-1. We assign this sixth progression as $B^n_0T^2_2$. Figure 3-10 shows the change in relative intensity of the $B^3_0T^1_1$ and $B^3_0T^2_2$ bands near 315 nm with changing backing pressure.

3-6 Discussion

The point symmetry of [2.2]paracyclophane can be considered

Figure 3-9 Five members of the $B^n_0T^1_1$ and $B^n_0T^2_2$ progressions. (These scans were taken at lower carrier gas pressure than Figure 3-1; the relative intensities are arbitrary.)

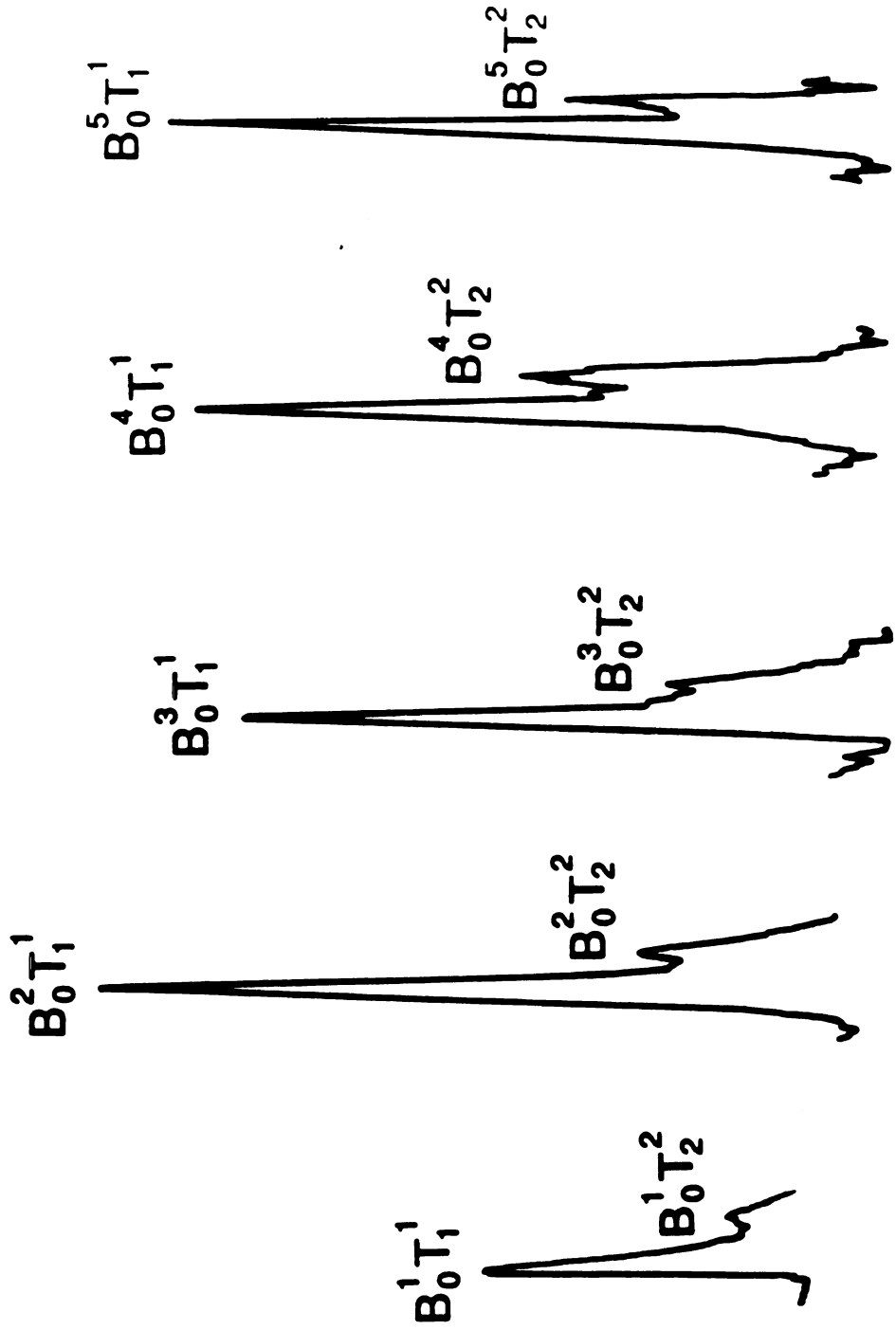
$B_0^5T_1^1$
$B_0^5T_2^2$
$B_0^4T_1^1$
$B_0^4T_2^2$
$B_0^3T_1^1$
$B_0^3T_2^2$
$B_0^2T_1^1$
$B_0^2T_2^2$
$B_0^1T_1^1$
$B_0^1T_2^2$

Figure 3-10 The $B^3_0T^1_1$ and $B^3_0T^2_2$ bands near 315 nm. The four scans in the figure were taken under different carrier gas pressure conditions; the $B^3_0T^2_2$ band (the band on the right) grew as the pressure was decreased.

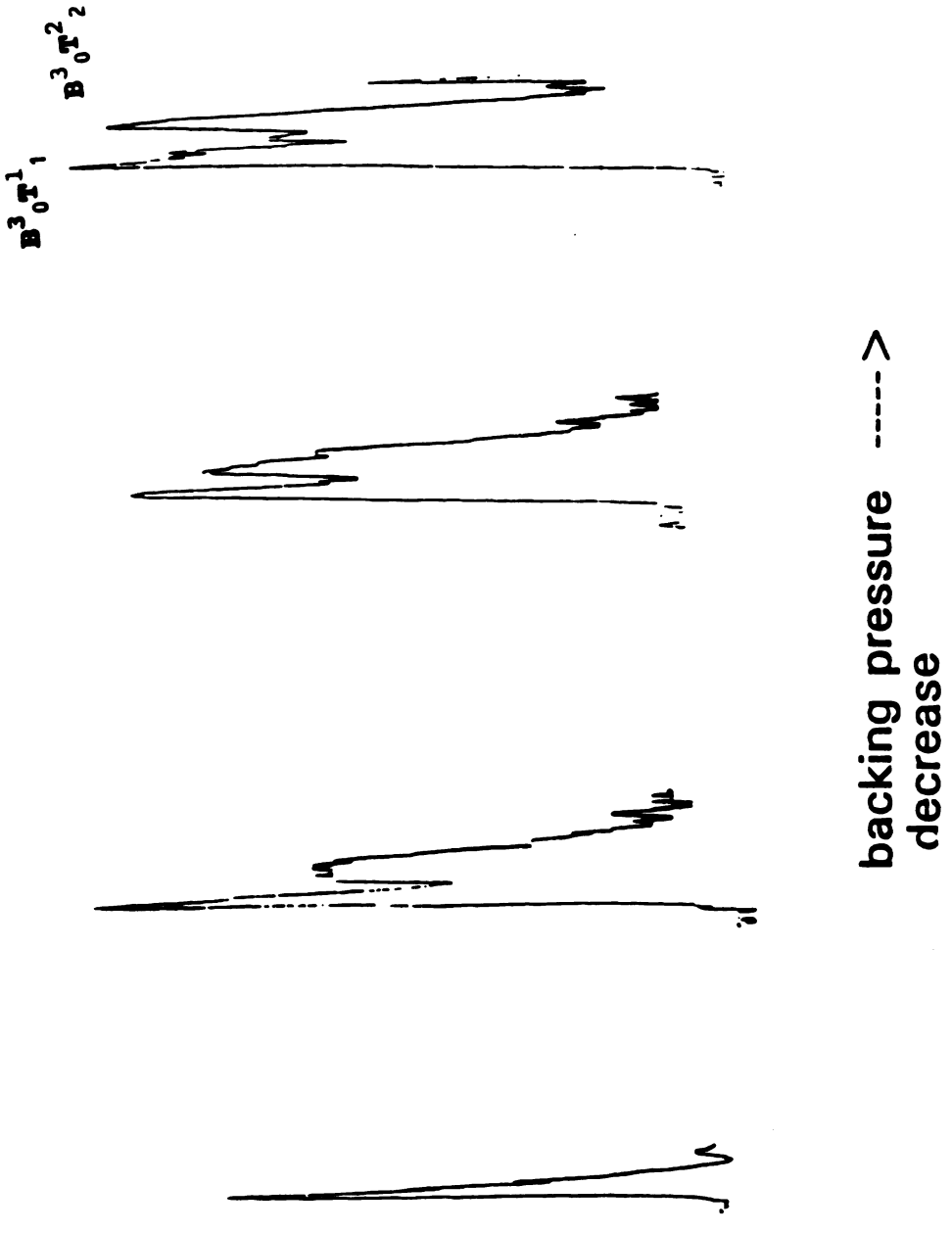
$B^3_0T^1_1$
$B^3_0T^2_2$
backing pressure ----->
decrease

as D_{2h} when the two benzene rings are eclipsed, and D_2 when the rings are twisted in relation to one another. In D_{2h}, assuming a totally symmetric (A_g) electronic ground state, the general electronic selection rules allow electronic transitions to upper states with B_{1u}, B_{2u}, and B_{3u} symmetry. Transitions to A_u and to all the g-states are forbidden. In the D_{2h} point group, the lowest excited electronic state has B_{2g} symmetry; $^1B_{2g} \leftarrow\!- {}^1A_g$ is forbidden according to the selection rules. However, if Herzberg-Teller type vibronic coupling is considered, the $^1B_{2g}$ state can interact with a higher electronic state having $^1B_{2u}$ symmetry through a nontotally symmetric vibration with a_u symmetry, such as the inter-ring twisting vibration, since the direct product $B_{2g} \times a_u = B_{2u}$. Such vibronic intensity borrowing could explain the observed intensity of the electronic transition.

Analysis of the X-ray data has shown that [2.2]paracyclophane has a twisted structure in the crystal, which reduces the symmetry of the molecule from D_{2h} to D_2. From the correlation table, under the reduced symmetry a B_{2g} state becomes B_2, and $B_2 \leftarrow\!-$ A is an allowed transition in the D_2 point group (see Table 3-3). The geometry of [2.2]paracyclophane in the gas phase has not been established; regardless of whether the symmetry is D_{2h} or D_2, optical excitation of the lowest energy excited state should be permitted.

The most important aspect of our interpretation of the

excitation spectrum is that the vibronic activity arises from only two low frequency inter-ring modes. Unfortunately, the vibrational analysis of [2.2]paracyclophane is incomplete [127,128]; in particular, the important low frequency modes have not been observed in the gas phase. In order to verify our assignments, we have undertaken theoretical structural optimization and normal mode analysis by using GAUSSIAN 86 and GAMESS at the STO-3G level [3-28]. These calculations were carried out by Prof. J. E. Jackson of our department. Essentially identical results were obtained with both programs; D_{2h} geometries are predicted for both the ground and first excited electronic states. The calculated normal coordinate relative displacements for the ground state inter-ring breathing and twisting vibrations are shown in Figure 3-11. It is clear from Figure 3-11(a) that in the twisting mode the two benzene rings are rotating counter to one another; the displacement vectors for all the hydrogen atoms on one ring (and the smaller displacements of the carbon atoms to which they are attached), together with the hydrogens and the carbon of the neighboring ethylene bridge, move in phase. The twist is calculated to be ~50 cm^{-1}, the lowest frequency of all ninety vibrational modes. In Figure 3-11(b), the relative displacement vectors illustrate that the breathing mode (with a calculated frequency of 276 cm^{-1}) can be characterized as primarily a change in the inter-ring separation. Goldacker et al. [125] have studied the effect of selective deuteration

Figure 3-11 Calculated normal coordinate relative displacements for (a) the inter-ring twisting vibration, and (b) the inter-ring breathing vibration of [2.2]paracyclophane. The predicted frequencies (cm^{-1}) of these modes in the ground electronic state are also listed.

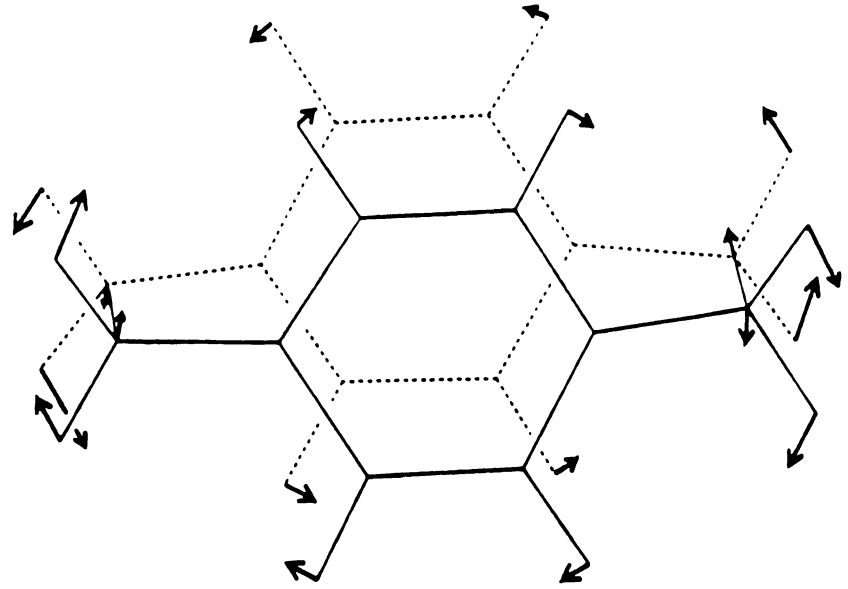

(a)

50 cm^{-1}

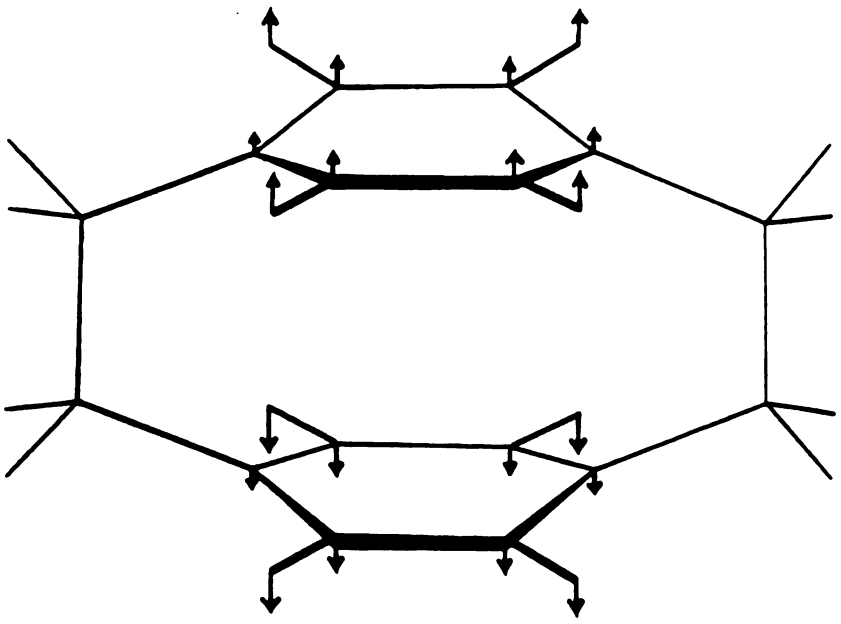

(b)

276 cm^{-1}

on the 241 cm^{-1} (ground state) mode in the crystal. When the ring hydrogens of [2.2]paracyclophane were replaced with deuterium atoms, the frequency decreased by 4.6%; when the methylene bridges were deuterated, the frequency was 0.8% below that of the normal isotopomer. We have also calculated the vibrational frequencies of these partially deuterated [2.2]paracyclophanes. For the 276 cm^{-1} mode the values decrease 4.3% and 0.1%, in agreement with the experimental results; this provides additional support for our assignment of the breathing mode.

From the band separations of the various progressions and supported by the normal mode calculation, we conclude that the breathing mode in the first excited state of [2.2]paracyclophane is vibronically active, and has a frequency of 235 cm^{-1}. However, the analysis of the twisting mode is not straightforward. Although this vibration is active in combination with the breathing mode, the obstacle is that the $\Delta v=0, \pm 2, \ldots$ selection rule precludes observation of the twisting fundamental and provides no connection between the odd and even quantum levels. According to our assignments, the following relationships hold:

$$B^n_0T^0_2 = B^n_0 - 2\nu_T'' = B^n_0 - 34 \text{ cm}^{-1},$$

$$B^n_0T^2_0 = B^n_0 + 2\nu_T' = B^n_0 + 78 \text{ cm}^{-1},$$

$$B^n_0T^1_1 = B^n_0 + \nu_T' - \nu_T'' = B^n_0 + 31 \text{ cm}^{-1},$$

$$B^n_0T^2_2 = B^n_0 + 2\nu_T' - 2\nu_T'' \approx B^n_0 + 44 \text{ cm}^{-1},$$

and $B^n{}_0T^3{}_1 = B^n{}_0 + 3\nu_T' - \nu_T'' = B^n{}_0 + 119\ cm^{-1}$.

From this analysis, sets of self-consistent energy levels can be estimated as follows: for $v_T''=0, 1, 2$ the values 0, 5, 34 cm^{-1} and for $v_T'=0, 1, 2, 3$ the values 0, 36, 78, 124 cm^{-1} (see Figure 3-12). To some degree of approximation, large amplitude vibrations may be separated from the other vibrations of a molecule and treated as a one-dimensional vibration problem [41]. The energy levels can be calaulated by solving one dimensional wave equations with appropriate potential functions. The potential functions used to describe large amplitude motions may be divided into the following two types:

- periodic functions

- non-periodic functions

Any continuous periodic function of a single variable can be expanded as a Fourier series:

$$F(\alpha) = b_0 + \sum_{n=1}^{\infty} b_n \cos n\alpha + \sum_{n=1}^{\infty} c_n \sin n\alpha \quad \text{(III-1)}$$

Most of the molecules with internal rotation have symmetrical potential functions; they must satisfy the boundary condition $V(\alpha) = v(\pi + \alpha)$. Since $\cos n\alpha = \cos n(\pi$

Figure 3-12 Vibrational energy level diagram for the twisting mode of [2.2]paracyclophane

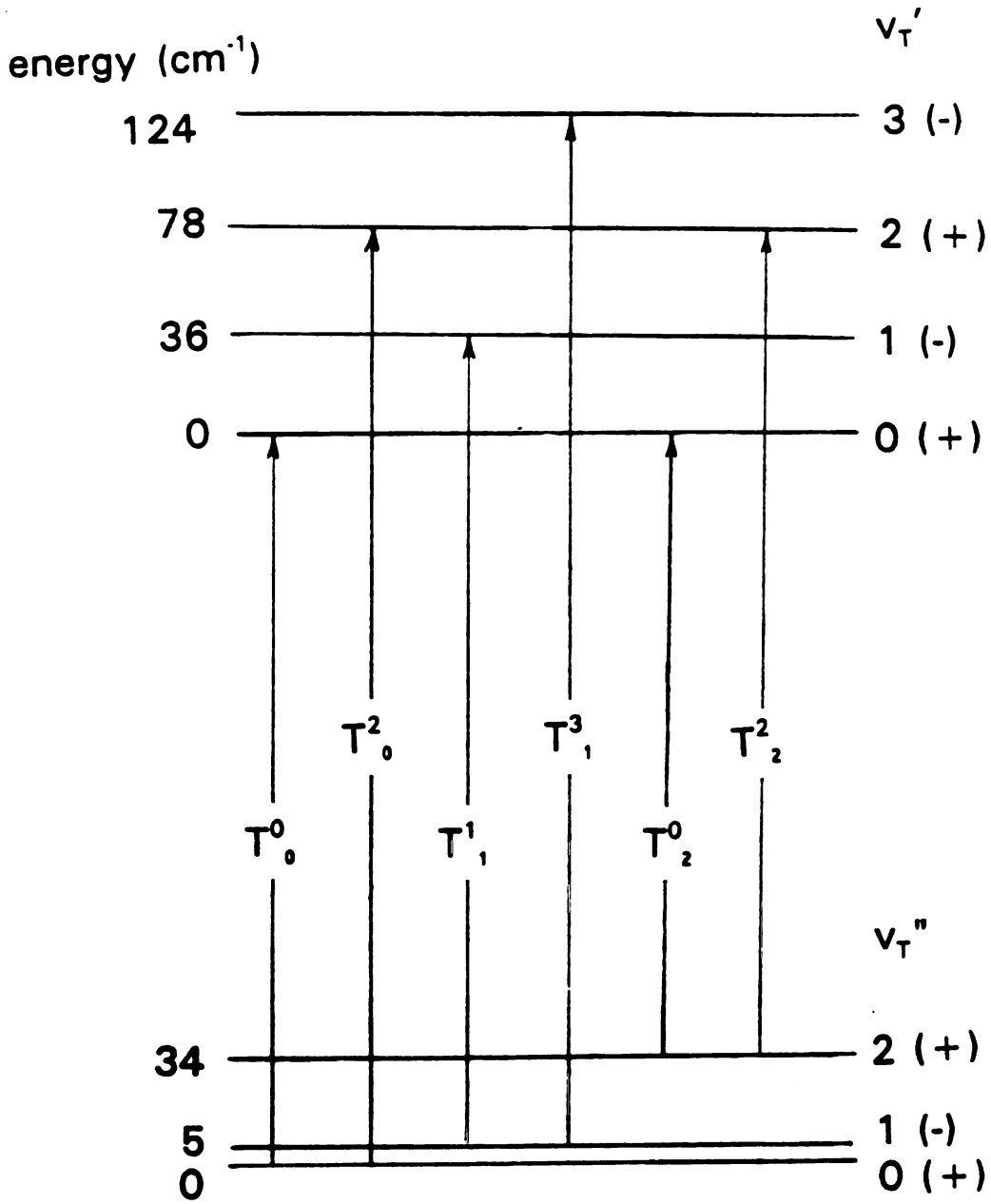
energy (cm-1)
v_T'
124
3 (-)
78
2 (+)
36
1 (-)
0
0 (+)
T^2_0
T^3_1
T^2_2
T^0_0
T^1_1
T^0_2
v_T''
34
2 (+)
5
1 (-)
0
0 (+)

$+ \alpha)$, while $\sin n\alpha = - \sin n(\pi + \alpha)$ the potential function for such molecules can be expressed as a cos Fourier series:

$$v(\alpha) = \sum_{n} v_n \cos n\alpha \qquad \text{(III-2)}$$

or this may be written in the form (for suitable choice of origin)

$$v(\alpha) = \sum_{n} v_n/2 \quad (1 - \cos n\alpha) \qquad \text{(III-3)}$$

This potential energy function has been used to describe the internal rotation vibration, where only the terms n = N, 2N, 3N, ... are used for an N-fold rotor. Thus, for a three-fold rotor such as ethane, the v_3 term is by far the most important, although the v_6 term may also contribute slightly. When the higher term is small, the v_3 term is effectively a measure of the barrier to the internal rotation.

The vibrational energy levels can be obtained by solving the wave equation

$$- B \, d^2\psi/d\alpha^2 + v(\alpha)\psi = E\psi \qquad \text{(III-4)}$$

where B is the internal rotation constant that can be calculated from the molecular structure. For a three-fold symmetry potential this equation is

$$- B\, d^2\psi/d\alpha^2 + v_3/2\,(1 - \cos 3\alpha) = E\psi \qquad \text{(III-5)}$$

standard tables and computer programs are available to provide the solutions for these equations [130,131].

The simplest form of the non-periodic potential functions is the power series expanded in a coordinate x. For a symmetrical potential function, the expansion contains only even powers of x, whereas both even and odd powers are included for the potential function with no symmetry.

symmetrical function $$v(x) = \sum_n a_{2n}\, x^{2n} \qquad \text{(III-6a)}$$

non-symmetrical function $$v(x) = \sum_n a_n\, x^n \qquad \text{(III-6b)}$$

The variable x is used to describe the specific dimension associated with the large amplitude vibration. A typical example is the ring-puckering vibration. If the potential function is governed by the quartic x^4 rather than the quadratic x^2 terms (the familiar harmonic potential), then the potential function can be written as:

$$v(x) = a\,(x^4 + b\,x^2)$$

where a and b are force constants. The one dimensional Schrodinger equation for this potential function has been solved numerically, and the eigenvalues can be found in a tabulated form [132]. From these tables, it is possible to determine the effect of different order terms in the potential on the eigenvalues. For example, for negative values of b the potential becomes one with a double-minimum, in which the barrier height is $b^2/4$.

There is another type of potential often used to describe the ring-puckering and inversion vibrations by intruducing a central barrier; the result of adding a Gaussian term [133] is:

$$v(x) = ax^4 + bx^2 + c\exp(-dx^2) \qquad \text{(III-7)}$$

In this potential function, we have taken the general potential function to be a simple harmonic oscillator function which is perturbed by a quartic term and a Gaussian term. Coon et al. [134] have adopted this potential function without the quartic term; then only three independent parameters will determine the shape of the potential function. The potential function is expressed in the form

$$V(Q) = 1/2\ \lambda Q^2 + A \exp(-a^2Q^2) \qquad \text{(III-8)}$$

and the Hamiltonian can be written as

$$H = - h^2/8\pi^2 \ (d^2/dQ^2) + \lambda Q^2/2 + A \exp(-a^2Q^2) \quad \text{(III-9)}$$

Q is defined by $2T = (Q')^2$, the parameter ρ is defined by the relationship $a^2 = e^{\rho}\lambda/2A$ and the parameter ν_0 is related to λ through the relation $\lambda=(2\pi c\nu_0)^2$. The dimensionless parameter B is defined so the barrier height is $Bhc\nu_0$, and

$$Bhc\nu_0 = A(e^{\rho} - \rho - 1)/e^{\rho} \quad \text{(III-10)}$$

the barrier height in cm^{-1} is $B\rho_0$.

The eigenvalue problem has been solved by Coon et al. [134] and the energy levels

$$G/\nu_0 = E/hc\nu_0 - B(\rho + 1)/(e^{\rho} - \rho - 1) \quad \text{(III-11)}$$

are complied in tables for seven different values of ρ.

This three-parameter potential has been used as the model for the twisting vibration of [2.2]paracyclophane. The fitting procedure will be described as follows. If we follow the notation used by Coon et al., where v_i is used to designate the vibrational quantum number 0^+, 0^-, 1^+, 1^-,.... , the vibrational energy in cm^{-1} is written as

$$G(v_i) = G(0^+) + G_0(v_i) \quad \text{(III-13)}$$

To find the parameters ν_0, B, ρ for the twisting mode of [2.2]paracyclophane, we first arbitrarily choose a value of ρ. For example ρ = 0.6. The other two parameters B and ν_0 can be determined from any two observed energy levels. To determine B, we must calculate the ratio of the two choosen energy levels. Let us calculate the ground state energy levels $G_0(v_i)$ = $0(0^+)$, $5(0^-)$, $34(1^+)$

$$[G(1^+) - G(0^+)]/[G(1^+) - G(0^-) = 1.1724 \qquad \text{(III-14)}$$

Using the table in Coon et al. [134], this ratio can be plotted against B, and it is found that the experimental value corresponds to B = 0.771. The value ρ_0 may be obtained from the relation

$$\rho_0 = [G(1^+) - G(0^+)] \; / \; [G(1^+)/\nu_0 - G(0^+)/\nu_0]$$
$$\approx 45 \text{ cm}^{-1} \qquad \text{(III-15)}$$

the numerator is calculated from the observed energy levels, and the denominator from the table in Coon et al. The results for the ground and excited state are summarized in Table 3-4. By following this procedure, we obtain barrier heights of ~35 cm^{-1} for the ground state, a value in accord with interpretations of the calorimetric data [108c, 135], and ~7

TABLE 3-4 Constants of the double-minimum potential functions of [2.2]paracyclophane

constant	ground state	excited state
ρ	0.6	0.6
ν_0	45 cm^{-1}	49 cm^{-1}
B	0.771	0.131
$G(0^+)$	19 cm^{-1}	15 cm^{-1}
barrier height	34 cm^{-1}	7 cm^{-1}

cm^{-1} for the excited state. In this model, the lowest vibrational level of [2.2]paracyclophane in the ground state lies below the barrier, resulting in a twisted equilibrium geometry, whereas in the upper state D_{2h} symmetry applies even to the zero-point level.

Chapter 4

Multiphoton ionization spectroscopy in supersonic jets

Optical methods of detecting electronic excited states of molecules depend on the absorption of photons from a radiation field under resonance conditions, and then upon examination of the changes: in the radiation field itself (absorption spectroscopy), the emission by the molecule, ionization of the molecule, or dissociation of the molecule. Any of these methods can be used jointly with the supersonic jet technique.

With the advances in high power, pulsed tunable dye lasers, the method of using multiphoton ionization (MPI) spectroscopy as a tool to detect excited states has been widely employed [136-143]. In the multiphoton ionization method, the spectrum of the resonance peaks in the ion current as a function of excitation laser wavelength can provide information about the n-photon excited state. This is similar to fluorescence excitation spectroscopy in which laser-induced fluorescence from an n-photon excited state is detected, and information about the upper electronic excited state is revealed. Although there can be many variations of the MPI technique, it should be recognized that the basic molecular

parameters that control the MPI processes, the cross sections, are typically 10^{-50} cm^4 sec $photon^{-1}$ for a two-photon absorption and 10^{-82} cm^6 sec^2 $photon^{-1}$ for a three-photon absorption. Therefore, the efficiency of these higher order processes are generally low.

The study of molecules in supersonic jets requires very sensitive methodology, and MPI is a very attractive option in this regard [144-147]. However, the MPI technique also offers other advantages. For example, the molecules of interest might have excited state lifetimes shorter than the laser pulse width, and thus have very low fluorescence quantum yields due to the fast non-radiative decay processes. These molecules can best be observed by methods such as MPI. However a few conditions must be fulfilled in order to use MPI on any molecular system. First, the excited states should not have a decay rate that is faster than the rate of ionization. Second, the cross section for the ionization from the excited state should be constant over the region of interest. Finally, saturation of the transition between the ground and excited states should be avoided.

In the simple case of MPI, an n-photon absorption process leads to ionization

$$n\ h\nu \geq IE$$

where $n\ h\nu$ is the sum of the energies of the n photons and IE

is the ionization energy of the molecule. In this case the number of ions being produced is proportional to I^n, where I is the laser intensity. Since most organic molecules (e.g. aromatic molecules) have ionization energies between 7 and 13 eV, MPI is easily achieved by using near-uv pulsed dye lasers.

When the MPI method is combined with supersonic jet expansion, the ionization process is even more powerful since the cooling provided by the expansion resolves most vibronic states, and a resonance condition can be achieved. In a favorable case,

$$2\ h\nu_1 \geq IE$$

and the photon $h\nu_1$ can reach the excited state S_1 (satisfy resonance condition) from which the second photon $h\nu_1$ will ionize the molecule. This type of process is generally called one-color resonance-enhanced two-photon ionization or R2PI, and the cross-section is much larger than 10^{-54} cm^4 sec $photon^{-1}$. The same result can be obtained with a two-color R2PI process provided that the energy sum of the two photons exceeds the IE. In two-color R2PI experiments, laser light at one wavelength ($h\nu_1$) excites the molecular system into a specific excited vibronic state, and then the second laser at another wavelength ($h\nu_2$) ionizes the molecules from the excited state. By tuning the wavelength of the first laser,

and keeping the wavelength of the second laser constant to ionize the excited molecules, ions are produced when $h\nu_1$ is in resonance with an excited vibronic level. Variation of the time delay between $h\nu_1$ and $h\nu_2$ can be used to determine the excited state lifetime, thus providing information on the dynamics of excited states. An important application of two-color MPI is to tune $h\nu_1$ to a vibronic level of a given excited electronic state and fix the wavelength, and then tune the second laser $h\nu_2$ through the ionization threshold to yield the photoionization efficiency curves of the excited states. This approach allows the IE to be measured with much higher precision ($\leq$ 5 cm^{-1}) than does conventional ionization spectroscopy.

MPI spectroscopy of aniline [144,145] is a good example to demonstrate the utility of this technique (see Figure 4-1). The $^1B_2$ <-- $^1A_1$ (S_1 <--- S_0) transition of aniline in the uv is very well characterized (see discussion in Section 2-6). Two types of MPI experiments can be performed with this molecule: (1) The electronic origin of the $^1B_2$ state is located at 34037 cm^{-1}; since this is more than half of the first ionization threshold (IE = 62265 cm^{-1}), it is possible to record the absorption spectrum of the first excited state via $h\nu_1$ + $h\nu_1$ one color resonant two-photon ionization. If the laser is tuned to the origin of the first excited state of aniline, the first step of the R2PI is the strong one-photon absorption to the origin, and the absorption of the second photon will

Figure 4-1 Schematic energy diagram for multiphoton ionization spectroscopy of aniline

aniline

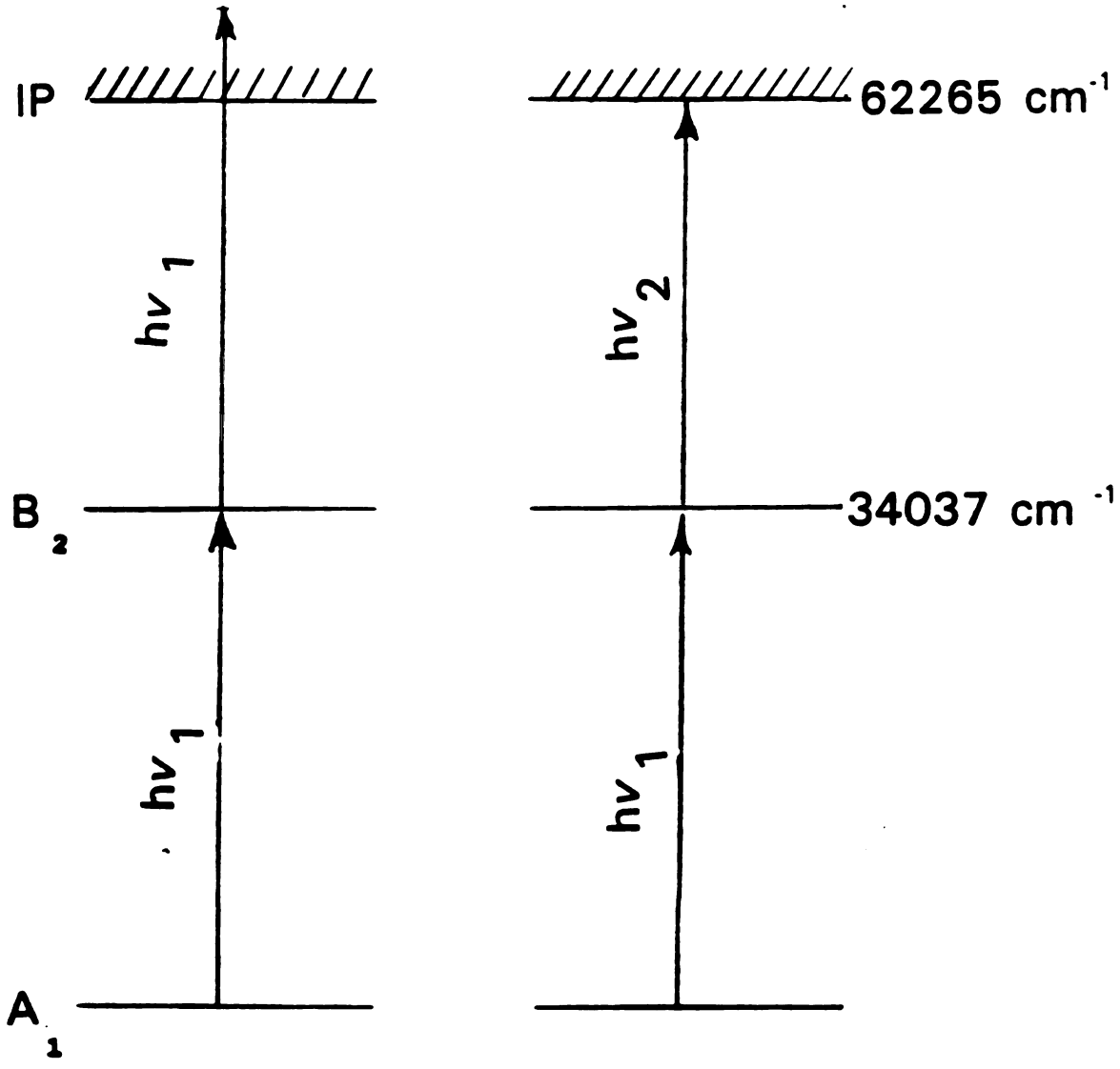

(1) one color two-photon photoionization

(2) Two color two-photon photoionization

ionize the molecule. By scaning the laser near the origin and monitoring the ion current as a function of $h\nu_1$, one obtains the excitation spectrum. (2) On the other hand, one can fix $h\nu_1$ at 34037 cm^{-1} and tuning $h\nu_2$ between 28180 cm^{-1} and 28850 cm^{-1}, the ionization threshold will be observed at a total energy $h\nu_1 + h\nu_2 = 62265\ cm^{-1}$. When performing this type of experiment, it is important that the power of the first laser (the excitation laser) should kept low to enhance the two-color signal, and that the diameter of the ionization beam should always kept larger than the excitation laser. The excitation laser power should reduced to a point that no signal can be observed without the ionization laser. It is well-known that jets can produce van der Waals clusters under suitable conditions, but the stoichiometry and the properties of these clusters is generally unknown. There are many techniques one can employ to investigate cluster chemistry in supersonic beams. The most popular laser spectrocopic methods are laser-induced fluorescence and resonant two-photon ionization. A benchmark study by Amirav et al. [148] on the tetracene·Ar_n clusters is a typical example of using the fluorescence method to study van der Waals molecules. The origin of the S_1 <--- S_0 electronic transition of tetracene·Ar_n clusters is increasingly red shifted from the bare tetracene origin with increasing n; each van der Waals spectral feature can be assigned to a different solvent cluster for n = 1 - 7. Also the pressure dependence of each of these van der Waals

transitions can be measured by means of the change in peak intensity; the intensity of the van der Waals peaks can be normalized to the intensity of the corresponding bare tetracene molecule transition, from which the authors obtained the relationship: $I(\text{tetracene}\cdot Ar_n)/I(\text{tetracene}) \sim (\text{pressure}^2)^n$.

The principle of using the resonant two-photon ionization method to study clusters is no different from the application to bare molecules. Clusters of a given size n can be excited to a stable excited state by absorbing a uv photon and a second uv photon will ionize the cluster. The cluster can be ionized only if the excitation frequency coincides with a specific absorption of that cluster. One should be cautious because if fragmentation occurs, the spectrum for the n-mer will superimposed on the spectra of other smaller clusters. The excited ionic states of clusters are always predissociative; the fragmentation thresholds of cluster ions are low, typically 0.3 eV to 3 eV. Therefore, it is crucial to restrict the ionization energy so that the excess energy above the threshold is kept lower than the ion state binding energy (0.02 eV - 0.04 eV) per solvent atom or molecule. This is the reason why R2PI is a better ionization method than the electron impact method.

The time-of-fight mass spectrometer (TOFMS) has been accepted as the primary tool in laser ionization experiments [149]. The primary advantage of TOFMS is that the full mass

spectrum can be aquired with a single ionization pulse; this is important since the ionization laser is operated at a very low repetition rate (10 Hz - 50 Hz for the nanosecond Nd:YAG-pumped dye laser.) Futhermore, TOFMS also has the advantages of being very simple to construct and relatively inexpensive. Our TOFMS, shown schematically in Figure 4-2, is a simple instrument based on the design of Wiley and Mclaren [150] (manufactured by R. M. Jordan Co.) The TOFMS is mounted on a 6" stainless steel chamber which is pumped by a 6" oil diffusion pump (Varian VHS-6). The diffusion pump has a liquid nitrogen cooled trap (Varian 362-6) above it to prevent the back streaming of diffusion pump oil, and the chamber can be closed from the pump by a 6" manual aluminum sliding gate valve. The supersonic jet is skimmed and differentially pumped by a 240 l/s turbomolecular pump (Balzers TSU-240 pumping station) after it enters the TOF tube. The skimmer helps collimate the beam so it passes through the ionization region without being perturbed. The 6" diffusion pump will handle most of the gas load in the ionization region. The pressure in the acceleration region and the flight tube should kept as low as possible to optimize the signal-to-noise ratio and to extend the lifetime of the electron multiplier detector (a Galileo dual microchannel plate with a gain of 10^7) The ionization region is enclosed by a liquid nitrogen cooled cryoshield in order to keep the ionization clean from contamination. The contamination can come from two sources:

Figure 4-2 Jordan TOF mass spectrometer

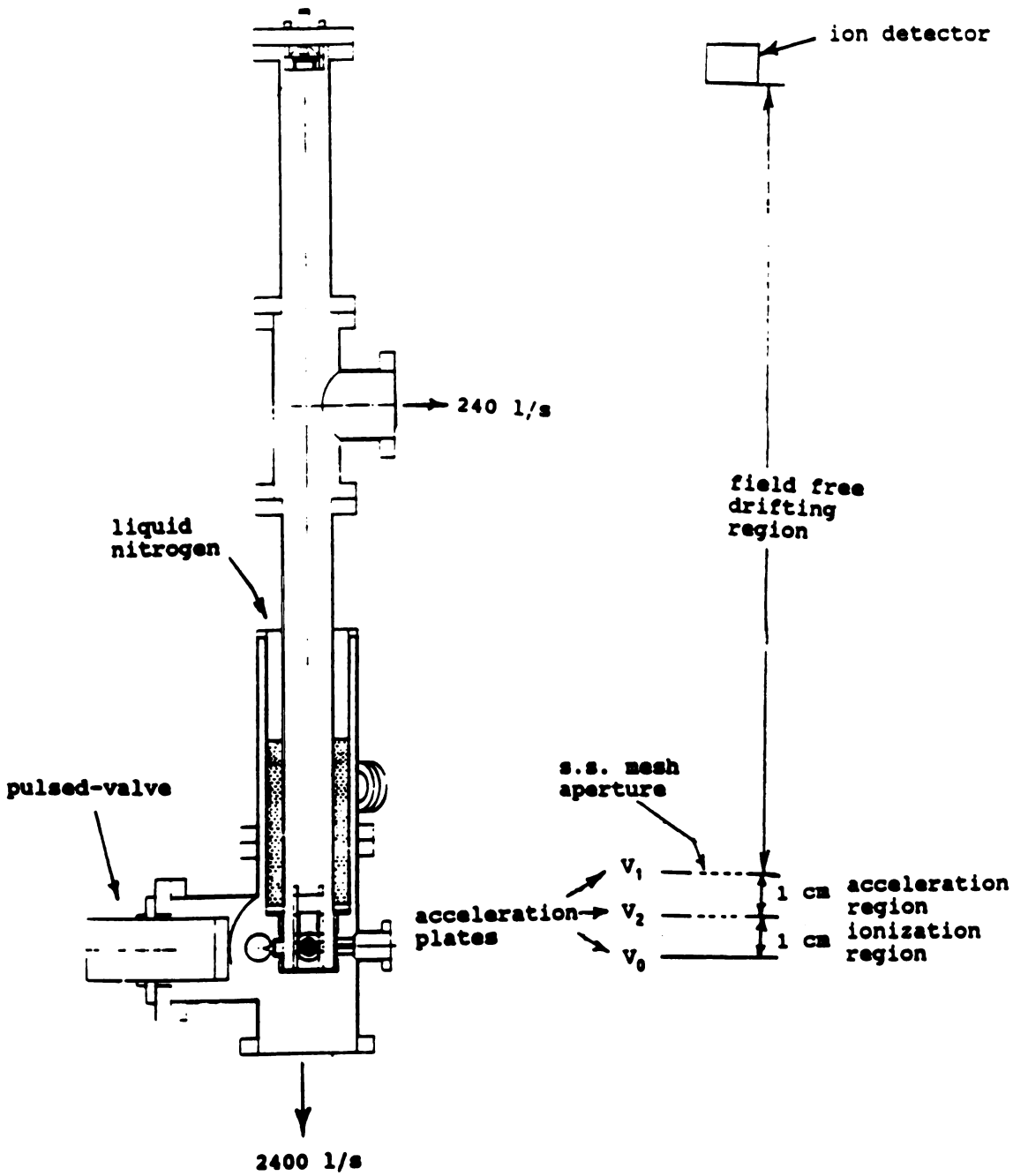
ion detector
240 l/s
field free
drifting
region
liquid
nitrogen
s.s. mesh
aperture
pulsed-valve
V_1
1 cm
acceleration
region
acceleration
plates
V_2
1 cm
ionization
region
V_0
2400 l/s

the back streaming of the pump oil and backscattered molecules from the jet colliding with the walls. The design of the acceleration region is quite simple (see Figure 4-2); it consists of three plates with 1 cm separations, held at different voltages. The supersonic source for the TOFMS is a stainless steel pulsed valve based on the current loop mechanism (see discussions in Chapter 2); this valve can produce 55 μsec wide gas pulses.

The key factor that determines the resolution in the TOF method is the velocity spread of the molecules. The resolution is defined as $R = T/(2\Delta T)$, where T is the total flght time of an ion, and ΔT is the FWHM of the peak. Thus, if the flight time of the ion is 2,000 ns and the FWHM of the peak is 20 ns, we have a resolution of 50. The supersonic beam offers a great advantage in that the velocity distribution of molecules is much narrower (smaller ΔT) as a result of the supersonic expansion. A resolution of 800 has been reported by users of the Jordan TOFMS.

REFERENCES

1 R. G. J. Fraser, MOLECULAR RAYS, Cambridge University Press London (1931).

2 R. G. J. Fraser, MOLECULAR BEAMS, Methuen & Co, London (1937).

3 N. F. Ramsey, MOLECULAR BEAMS, Oxford University Press (1954).

4 W. H. Bessey and O. C. Simpson, Chem. Rev. 30, 234 (1942).

5 I. Estermann, Rev. Mod. Phys. 18, 300 (1945).

6 W. L. Fite and S Datz, Ann. Rev. Phys. Chem. 14, 61 (1963).

7 Disscussions Faraday Soc. vol 33 (1962); vol 55 (1973); vol 62 (1977); vol 73 (1982); vol 75 (1983)

8 R. D. Levine and R. B. Rernstein, MOLECULAR REACTION DYNAMICS AND CHEMICAL REACTIVITY, Oxford University Press, London (1987).

9 T. R. Dyke and J. S. Muenter, MTP International Review of Science, Physical Chemistry Series Two, Vol 2, 27 (1975)

10 W. Klemperer, J. Mol. Struct. 59, 161 (1980).

11 R. E. Smalley, L. Wharton and D. H. Levy, Acc. Chem. Res. 10, 139 (1977).

12 D. H. Levy, Ann. Rev. Phys. Chem. 31, 197 (1980).

13 D. H. Levy, Science, 214, 263 (1981).

14 D. H. Levy, Adv. Chem. Phys. 47, 323 (1981).

15 B. J. Howard, MTP International Review of Science, Physical Chemistry Series Two, Vol 2, 93 (1975)

16 G. E. Ewing, Angew. Chem. Int. Ed. 11, 486 (1972).

17 G. E. Ewing, Acc. Chem. Res. 8, 185 (1975).

18 G. E. Ewing, Ann. Rev. Phys. Chem. 27, 533 (1976).

19 W. Klemperer, Ber. Bunsenges. Phys. Chem. 78, 128 (1974).

20 F. G. Celii and K. C. Janda, Chem. Rev. 86, 507 (1986).

21 D. J. Nesbitt, Chem. Rev. 88, 843 (1988).

22 J. M. Hutson, Ann. Rev. Phys. Chem. 41, 123 (1990).

23 L. A. Philips, and D. H. Levy, J. Chem. Phys. 89, 85 (1988).

24 J. C. Alfano, S. J. Martinez, and D. H. Levy, J. Chem. Phys. 94, 1673 (1991).

25 K. C. Janda, Adv. Chem. Phys. 60, 201 (1985).

26 M. P. Casassa, Chem. Rev. 88, 815 (1988).

27 R. E. Miller, Science, 240, 447 (1988).

28 R. E. Miller, Acc. Chem. Res. 23, 10 (1990).

29 J. Jortner, Ber. Bunsenges. Phys. Chem. 88, 188 (1984)

30 J. Jortner, R. D. Levine, and S. A. Rice, Adv. Chem. Phys. 70, 1 (1988).

31 H. Haberland, H. G. Schindler, and D. R. Worsnop, J. Phys. Chem. 88, 3903 (1984).

32 O. Cheshnovsky and S. Leutwyler, Chem. Phys. Lett. 121, 1 (1985).

33 L. W. Peng, M. Dantus, A. H. Zewail, K Kemnitz, J. M. Hicks, and K. B. Eisenthal, J. Phys. Chem. 91, 6162 (1987).

34 W. H. Flygare, Acc. Chem. Res. 1, 121 (1968).

35 V. E. Bondybey, Ann. Rev. Phys. Chem. 35, 591 (1984).

36 J. B. Hopkins, J. B. Powers, and R. E. Smalley, J. Chem. Phys. 73, 683 (1980).

37 J. B. Hopkins, D. E. Powers, and R. E. Smalley, J. Chem. Phys. 72, 5039 (1980).

38 J. B. Hopkins, D. E. Powers, and R. E. Smalley, J. Chem. Phys. 72, 5049 (1980).

39 W. R. Lambert, P. M. Felker, and A. H. Zewail, J. Chem. Phys. 79, 5958 (1981).

40 E. B. Wilson, Jr. Adv. Chem. Phys. 2, 367 (1959).

41 D. G. Lister, J. N. Macdonald, and N. L. Owen, INTERNAL ROTATION AND INVERSION, Academic Press (1978).

42 V. W. Laurie, Acc. Chem. Res. 3, 331 (1970).

43 J. Laane, Pure & Appl. Chem. 59, 1307 (1987).

44 M. Ito, J. Phys. Chem. 91, 517 (1987).

45 K. Okuyama, N. Nakami, and M. Ito, J. Phys. Chem. 89, 5617 (1985).

46 L. H. Spangler, R. v. Zee, and T. S. Zwier, J. Phys. Chem. 91, 2782 (1987).

47 D. W. Werst, W. R. Gentry, and P. F. Barbara, J. Phys. Chem. 89, 729 (1985).

48 H.-S. Im and E. R. Bernstein, J. Chem. Phys. 88, 7337 (1988).

49 L. R. Khundkar and A. H. Zewail, J. Chem. Phys. 84, 1302 (1986).

50 P. J. Breen, J. A. Warren, E. R. Bernstein, and J. I. Seeman, J. Chem. Phys. 87, 1917 (1987).

51 V. H. Grassian, J. A. Warren, E. R. Bernstein, and H. V. Secor, J. Chem. Phys. 90, 3994 (1989).

52 T. Y. D. Lin and T. A. Miller, J. Phys. Chem. 94, 3554 (1990).

53 X. Q. Tan, W. A. Majewski, D. F. Plusquellic, and D. W. Pratt, J. Chem. Phys. 94, 7721 (1991).

54 A. Kantrowitz and J. Grey, Rev. Sci. Instrum. 22, 328 (1951).

55 J. B. Anderson, J. B. Fenn, Phys. Fluids, 8,780 (1965).

56 J. B. Anderson, R. B. Andres, and J. B. Fenn, Methods Exp. Phys. 7A, 345 (1968).

57 J. B. Anderson, In MOLECULAR BEAMS AND LOW DENSITY GAS DYNAMICS, P. P. Wegener ed, Dekker (1974)

58 H. Ashkenas and F. S. Sherman, Rarefied Gas Dynamics. Proceedings of the 3rd International Symposium, 2, 84 (1965).

59 D. R. Miller, In ATOMIC AND MOLECULAR BEAM METHODS, G. Scoles ed, Oxford University Press (1988).

60 N. Abuaf, J. B. Anderson, R. P. Andres, J. B. Fenn, and D. G. H. Marsden, Science, 155, 997 (1967).

61 R. A. Larsen, and D. R. Herschbach, Rev. Sci. Instrum. 45, 1511 (1974).

62 A. Amirav, U. Even, and J. Jortner, Chem. Phys. 51, 31 (1980).

63 O. Hagena and W. Obert, J. Chem. Phys. 56, 1793 (1972).

64 D. M. Lubman and R. N. Zare, J. Chem. Phys. 71, 4192

(1979).

65 H. Pauly, In ATOMIC AND MOLECULAR BEAM METHODS, G. Scoles ed, Oxford University Press (1988).

66 A. Amirav, U. Even, and J. Jortner, Chem. Phys. Lett. 83, 1 (1981).

67 C. M. Lovejoy and D. J. Nesbitt, Rev. Sci. Instrum. 58, 807 (1987).

68 D. H. Levy, In CHEMICAL AND BIOCHEMICAL APPLICATIONS OF LASERS, C. B. Moore ed, Academic Press (1977).

69 To get an idea of the detection limit, total number of fluorescence photons generated can be estimated by [ref.2-12]: $N = V \times n \times E \times \sigma$, where V is the volume of excited molecules that will be produced in the jet, n is the number density, E is the number of laser photons per laser pulse, and σ is the absorption cross section.

70 J.-A. Yu, Ph. D. Thesis, Michigan State University (1990).

71 J. E. Butler, Appl. Opt. 21, 3617 (1982).

72 E. Mazur, Rev. Sci. Instrum. 57, 2507 (1986).

73 W. R. Gentry, In ATOMIC AND MOLECULAR BEAM METHODS, G. Scoles ed, Oxford University Press (1988).

74 W. R. Gentry and C. F. Giese, Rev. Sci. Instrum. 49, 595 (1978).

75 A. Auerbach and R. McDiarmid, Rev. Sci. Instrum. 51, 1273 (1980).

76 J. B. Cross and J. J. Valentini, Rev. Sci. Instrum. 53, 38 (1982)

77 C. E. Otis and P. M. Johnson, Rev. Sci. Instrum. 51, 1128 (1980).

78 T. E. Adams, B. H. Rockney, R. J. S. Morrison, and E. R. Grant, Rev. Sci. Instrum. 52, 1469 (1981).

79 E. V. Shpolskii and R. I. Personov, Opt. Spectry. 8, 172 (1960).

80 M. M. Valdman and R. I. Personov, Opt. spectry, 19, 296 (1965).

81 C. Bouzou, C. Jouvet, J. B. Leblond, Ph. Millie, A. Tramer, and M Sulkes, Chem. Phys. Lett. 97, 161 (1983).

82 S. A. Schwartz and M. R. Topp, Chem. Phys. 86, 245 (1984).

83 B. Fourmann, C. Jouvet, A. Tramer, J. M. Lebars, and Ph. Millie, Chem. Phys. 92, 25 (1985).

84 S. P. Venksteshan and J. B. Fenn, J. Chem. Phys. 77, 2599 (1982).

85 G. M. McClelland, K. L. Saenger, J. J. Valentini, and D. R. Herschbach, J. Phys. Chem. 83, 947 (1979).

86 M. Sulkes, J. Tusa, S. A. Rice, J. Chem. Phys. 72, 5733 (1980).

87 J. W. Farthing, I. W. Fletcher, J. C. Whitehead, Mol. Phys. 48, 1067 (1983).

88 J. Tusa, M. Sulkes, S. A. Rice, and C. Jouvet, J. Chem. Phys. 76, 3513 (1982).

89 C. Jouvet, M. Sulkes, and S. A. Rice, Chem. Phys. Lett. 84, 241 (1981).

90 C. Jouvet, M. Sulkes, and S. A. Rice, J. Chem. Phys. 78,

3935 (1983).

91 D. J. Muller, R. I. McKay, G. B. Edwards, W. D. Lawrance, J. P. Hardy, A. B. Rock, K. J. Seway, S. H. Kable, and A. E. W. Knight, J. Phys. Chem. 92, 3751 (1988).

92 (a) R. J. Rubin and K. E. Shuler, J. Chem. Phys. 25, 59; 68 (1956) (b) E. W. Montroll and K. E. Shuler, J. Chem. Phys. 26, 454 (1957). (c) N. W. Bazley, E. W. Montroll, R. J. Rubin, and K. E. Shuler, J. Chem. Phys. 28, 700; 1185 (1958). (d) K. E. Shuler, J. Chem. Phys. 32, 1692 (1960).

93 I. R. Hurle, A. L. Russo, and J. G. Hall, J. Chem. Phys. 40, 2076 (1964).

94 R. P. Mariella, D. R. Herschbach, and W. Klemperer, J. Chem. Phys. 58, 3785 (1973).

95 M. P. Sinha, A. Schultz, and R. N. Zare, J. Chem. Phys. 58, 549 (1973).

96 N. Ginsburg and F. A. Matsen, J. Chem. Phys. 13, 167 (1945).

97 J. C. Brand, D. R. Williams, and T. J. Cook, J. Mol. Spectrosc. 20, 359 (1966).

98 M. Quack and M. Stockburger, J. Mol. Spectrosc. 43, 87 (1972).

99 D. A. Chernoff and S. A. Rice, J. Chem. Phys. 70, 2511 (1979).

100 N. Mikami, A. Hiraya, I. Fujiwara, and M. Ito, Chem. Phys, Lett. 74, 531 (1980).

101 A. Amirav, U. Even, and J. Jortner, Mol. Phys. 49, 899 (1983).

102 C. J. Brown and A. C. Farthing, Nature, 164, 915 (1949).

103 D. J. Cram, N. L. Allinger, and H. Steinberg, J. Am. Chem. Soc. 76, 6132 (1954).

104 D. J. Cram and J. M. Cram, Acc. Chem. Res. 4, 204 (1971).

105 K. Lonsdale, H. J. Milledge and M. V. K. Rao, Proc. Roy. Soc., Ser.A, 555, 82 (1960).

106 H. Hope, J. Bernstein, and K. N. Trueblood, Acta Cryst. B28, 1733 (1972).

107 M. T. Vala, Jr, I. H. Hiller, S. A. Rice and J. J. Jortner, J. Chem. Phys. 44, 23 (1966).

108 (a) A. Ron and O. Schnepp, J. Chem. Phys. 37, 2540 (1962) (b) A. Ron and O. Schnepp, J. Chem.Phys. 44, 19 (1966) (c) A. Ron, M. Noble and E. K. C. Lee, Chem. Phys. 83, 215 (1984).

109 D. S. McClure, Can. J. Chem. 36, 48 (1958).

110 C. B. Duck, N. O. Lipari, W. R. Salaneck and L. B. Schein, J. Chem. Phys. 63, 1758 (1975).

111 J. Spanget-Larsen, Theoret. Chim. Acta. 64, 187 (1983).

112 K. A. Doris, D. E. Ellis, M. A. Ratner, and T. J. Marks, J. Am. Chem. Soc. 106, 2491 (1984).

113 (a) S. Canuto and M. C. Zerner, Chem. Phys. Lett. 157, 353 (1989) (b) J. Am. Chem. Soc. 112, 2114 (1990).

114 I. H. Hiller, L. Glass and S. R. Rice, J. Chem. Phys. 45,

3015 (1966).

115 R. Gleiter, Tetrahedron Lett. 51, 4453 (1969).

116 D. J. Cram and R. H. Bauer, J. Am. Chem. Soc. 81, 5971 (1959).

117 W. Rebafka and H. A. Staab, Angew. Chem. Int. Ed. 13, 203 (1974).

118 H. Vogler, G. Ege, and H. A. Staab, Tetrahedron, 31, 2441 (1975).

119 G. Herzberg, MOLECULAR SPECTRA AND MOLECULAR STRUCTURE, vol.III. ELECTRONIC SPECTRA AND ELECTRONIC STRUCTURE OF POLYATOMIC MOLECULES, Van Nostrand Reinhold co., New. York, 1966).

120 H. Sponer and E. Teller, Rev. Mod. Phys. 13 (1941) 75.

121 J. M. Hollas, HIGH RESOLUTION SPECTROSCOPY, Butterworths (1982).

122 L. Goodman and J. M. Hollas, in: PHYSICAL CHEMISTRY-An Advanced Treatise, vol. III, H. Eyring, D. Henderson and W. Jost, eds Academic Press (1969).

123 K. K. Innes, in: EXCITED STATES, Vol. II, E. C. Lim ed, Academic Press (1975).

124 K. Matsui, N. Nishi, M. Kinoshita and S. Nagakura, Chem. Phys. 35,11 (1978).

125 W. Goldacker, D. Schweitzer, K. P. Dinse and K. H. Hausser, Chem. Phys. 48, 105 (1980).

126 K. L. Saenger, J. D. Barnwell and D. R. Herschbach, J.Phys. Chem. 86, 216 (1982).

127 V. Schettino, M. P. Marzocchi and G. Sbrana, J. Mol. Struct. 2, 39 (1968).

128 P. H. Scudder, V. Boekelheide, D. Cornutt and H. Hopf, Spect. Acta. 37A (1981) 425 (1981).

129 M. J. Frisch, J. S. Binkley, H. B. Schlegel, K. Raghavahari, C. F. Melius, R. L. Martin, J. J. P. Stewart, F. W. Borowicz, C. M. Rohlfing, L. R. Kahn, D. J. Defrees, R. Seeger, R.A. Whiteside, D. J. Fox, E. M. Fleuder, and J. A. pople, GAUSSIAN 86 (Carnegie-Mellon Quantum Chemistry Publishing Unit, Pittsburgh, 1984;Revision C). M. Dupuis, D. Spangler, and J. Wendoloski, GAMESS, NRCC Software Catalogue, program QG01 (Lawrence Berkeley Laboratory, 1980)

130 D. R. Herschbach, TABLES FOR THE INTERNAL ROTATION PROBLEM, Dept of Chemistry, Harvard University (1957)

131 J. D. Lewis, T. B. Malloy, T. H. Chao, and J. Laane, J. Mol. Struct. 12, 427 (1972).

132 J. Laane, Appl. Spectr. 24, 73 (1970).

133 S. Chan, J. Zinn, J. Fernandez, and W. D. Gwinn, J. Chem. Phys. 33, 1643 (1960).

134 J. B. Coon, N. W. Naugle and R. D. Mckenzie, J. Mol. Spec. 20, 107 (1966).

135 J. T. S. Andrews and E. F. Westrum, Jr, J. Phys. Chem. 74, 2170 (1970).

136 P. M. Johnson, M. R. Berman, and D. Zakheim, J. Chem. Phys. 62, 2500 (1975).

137 D. H. Parker and M. A. Al-Sayed, Chem. Phys. 42,379 (1979).

138 L. Zandee and R. B. Bernstein, J. Chem. Phys. 71, 1359 (1979).

139 T. G. Dietz, M. A. Duncan, M. G. Liverman and R. E. Smalley, Chem. Phys. Lett. 70, 246 (1980).

140 U. Boesl, H. J. Neusser, and E. W. Schlag, J. Chem. Phys. 72, 4327 (1980).

141 P. M. Johnson, Acc. Chem. Res. 13, 20 (1980).

142 P. M. Johnson and C. E. Otis, Ann. Rev. Phys. Chem. 32, 139 (1981).

143 M. A. Smith, J. W. Hager, and S. C. Wallace, J. Phys. Chem. 88, 2250 (1984).

144 E. R. Bernstein, K. Law, and M. Schauer, J. Chem. Phys. 80, 634 (1984).

145 M. A. Smith, J. W. Hager, and S. C. Wallace, J. Chem. Phys. 80, 3097 (1984).

146 E. Carrasquillo, T. S. Zwier, and D. H. Levy, J. Chem. Phys. 83, 4990 (1985).

147 S. Leutwyler, U. Even, and J. Jortner, J. Chem. Phys. 79, 5769 (1983).

148 A. Amirav, U. Even, and J. Jortner, J. Chem. Phys. 75, 2489 (1981).

149 D. M. Lubman, Anal. Chem. 59, 31A (1987).

150 D. M. Lubman and R. M. Jordan, Rev. Sci. Instrum. 56, 373 (1985).